

AN INVESTIGATION INTO THERAPIES FOR ATRIAL ARRHYTHMIAS USING A BIOPHYSICAL MODEL OF THE HUMAN ATRIA

THÈSE N° 3391 (2005)

PRÉSENTÉE À LA FACULTÉ SCIENCES ET TECHNIQUES DE L'INGÉNIEUR

Institut de traitement des signaux

SECTION DE GÉNIE ÉLECTRIQUE ET ÉLECTRONIQUE

ÉCOLE POLYTECHNIQUE FÉDÉRALE DE LAUSANNE

POUR L'OBTENTION DU GRADE DE DOCTEUR ÈS SCIENCES

PAR

Lam DANG

ingénieur en microtechnique diplômé EPF
de nationalité suisse et originaire de Genève (GE)

acceptée sur proposition du jury:

Dr J.-M. Vesin, directeur de thèse
Prof. H. Bleuler, rapporteur
Prof. L. Kappenberger, rapporteur
Dr N. Virag, rapporteur

Lausanne, EPFL
2006

Wheresoever you go, go with all your heart.

Confucius, Chinese philosopher & reformer (551-479 B.C.)

Acknowledgments

This thesis is the result of four years work and it would never have been possible for me to accomplish this without the help, support and encouragement from many people.

Foremost, I wish to express my gratitude to my advisor, Dr. Jean-Marc Vesin, for giving me the opportunity to achieve the research of this thesis within his group. I greatly appreciate the guidance he has given me over the years. The numerous discussions that we have had have been a constant source of inspiration to me. Not only have I benefited from his encyclopedic knowledge but he has also taught me many valuable lessons in life.

I am especially grateful to Prof. Adriaan van Oosterom, Dr. Vincent Jacquemet, Mr. Zenichi Ihara and Dr. Olivier Blanc, with whom I have worked very closely on most of the topics presented in this thesis. Their never-ending stream of ideas and their passion for research has fired my own enthusiasm. I would like to thank them for their ideas and comments, all of which have contributed greatly to the improvement of this thesis. So too, I thank Dr. Judith van Oosterom-Pooley, for her corrections to the English in my text.

The Lausanne-Heart project is led by Prof. Lukas Kappenberger from the Service de Cardiologie at the CHUV hospital in Lausanne. I would like to pay tribute to his sustained enthusiasm and vision in the project. It is due to him, his encouragement and the opportunities he has provided me with, that I have been able to meet such highly interesting people all over the world while attending international congresses and workshops.

My gratitude goes out to Dr. Nathalie Virag (Medtronic Europe), Dr. Patrick Ruchat and Dr. Jürg Schläpfer (Service de Cardiologie, CHUV) for their valuable collaboration during these last few years. I would also like to take this opportunity to thank Dr. Martin Rotter and Prof. Michel Haissaguerre (Service de Rythmologie, Hôpital Cardiologique du Haut-Lévêque, France) for their recent cooperation.

During the initial phase of this research Prof. Craig Henriquez and Dr. Kevin J. Sampson of Duke University in the United States generously offered their advice and collaboration, which is gratefully acknowledged.

In the last few years of this project a number of students have worked with me under my supervision. I particularly want to thank Mrs. Christophe Tournery, Vincent Ducry, Mattia Peterhans and Younes Majduline for their support.

Furthermore, I would like to thank Mr. Ryan Lahm, Drs. Jose Morissette and Arthur Stillman, who kindly furnished me with the atrial geometry surface model used in this study.

During my stay at the Signal Processing Institute, I have met many interesting people who have made the experience a rich one, not only at work but also on a personal level. I would like to mention one person in particular, Prof. Murat Kunt, the head of the institute, who made it possible for me to carry out my research there.

In addition, I wish to mention and to express my thanks here to Dr. Mattia Bertschi, Mrs. Mattieu Lemay, Philippe Jost, Yann Prudat, Dan Jurca, Ulrich Hoffmann and Dr. Elisa Drelie Gelasca, with whom I have spent a great deal of time in the laboratory during the course of my research, and to Dr. Gary Garcia, who encouraged me to start out on my doctorate studies and also provided me with constructive feedback throughout.

For all the help and support I have received in technical and administrative matters, I am indebted to Mr. Gilles Auric, Ms. Marianne Marion, Ms. Fabienne Vionnet and Mr. Eric Gruaz.

Finally, last but not least, my sincere gratitude goes to my family for their continuous support and encouragement throughout my studies.

This study was made possible by grants from the Theo-Rossi-Di-Montelera Foundation, Medtronic Europe and the Swiss Governmental Commission of Innovative Technologies (CTI).

Table of Contents

Acknowledgments	v
Table of Contents	vii
Version abrégée	xiii
Abstract	xv
Symbols and Acronyms	xvii
List of Figures	xxi
List of Tables	xxv
1 Introduction	3
1.1 Motivations and problem statement	3
1.2 Organization of the dissertation	6
1.3 Original contributions	7
I A biophysical model of the human atria	9
2 From the cell to the biophysical model	11
2.1 Introduction	11
2.2 Modeling the cardiac cell membrane	12
2.2.1 Cardiac cell properties	12
2.2.2 Modeling the active membrane properties	15
2.3 Modeling myocardial tissue	17
2.3.1 The bidomain model	17

2.3.2	The monodomain model	19
2.3.3	Electrograms	20
2.4	Geometry of human atria	20
2.4.1	Monolayer 3D surface	20
2.4.2	Multilayer 3D structure	22
2.5	Implementation of a biophysical model	22
2.6	Summary	23
3	Simulations of atrial arrhythmias	25
3.1	Introduction	25
3.1.1	Sinoatrial rhythm	26
3.1.2	Atrial flutter	26
3.1.3	Atrial fibrillation	27
3.2	Atrial flutter in the biophysical model	28
3.2.1	Atrial flutter in the monolayer 3D model	28
3.2.2	Atrial flutter in the multilayer 3D model	33
3.3	Atrial fibrillation in the biophysical model	36
3.3.1	Initiation of atrial fibrillation	36
3.3.2	Perpetuation of atrial fibrillation	36
3.3.3	Chronic atrial fibrillation	37
3.3.4	Meandering atrial fibrillation	39
3.3.5	Cholinergic atrial fibrillation	39
3.4	Conclusions	42
II	Measures of organization	43
4	Spatio-temporal organization	45
4.1	Introduction	45
4.2	Measures of organization	46
4.2.1	State of the art	46
4.2.2	Local high density mapping	47
4.2.3	Global mapping	48
4.2.4	Multidimensional signal analysis	49
4.3	Spatial organization	52
4.3.1	Local high density mapping	52
4.3.2	Global density mapping	53

4.4	Temporal organization	54
4.5	Conclusions	55
5	Tracking of phase singularities	57
5.1	Introduction	57
5.2	Phase singularity detection	58
5.2.1	Cardiac phase	58
5.2.2	Phase singularity	61
5.3	Localizing of phase singularities	61
5.3.1	Phase singularities in the general case	61
5.3.2	Phase singularities anchored around a macroscopic anatomical obstacle	62
5.4	Tracking of phase singularities	64
5.4.1	Limited search area	65
5.4.2	Exclusion of PSs already assigned	66
5.4.3	Constraint on the creation of new trajectories starting at vein orifice or valve ring	66
5.5	Number of PSs during simulated AF	68
5.5.1	Parity of the number of detected PSs	69
5.5.2	Effect of the slow inward current G_{si}	70
5.6	PSs lifespan during simulated sustained AF	71
5.6.1	Effect of the slow inward current G_{si} on PSs lifespan	71
5.6.2	Origin of long-lasting PSs	72
5.7	Spatial distribution of PSs	73
5.7.1	PS localization on a homogenous surface	73
5.7.2	PSs localization on an inhomogeneous surface	74
5.8	Conclusions	76
III	Therapies	77
6	Surgical and catheter ablation	79
6.1	Introduction	79
6.2	Modelling ablation patterns	80
6.2.1	Ablation lines implementation	81
6.3	Simulated ablation patterns	81
6.3.1	Standard maze patterns	81
6.3.2	Simpler surgical/RF patterns	83

6.3.3	Isolation of the pulmonary veins	84
6.3.4	Proposition of an ideal ablation pattern	85
6.4	Imperfect ablation lines	85
6.4.1	Incomplete Maze-III procedure	86
6.4.2	Incomplete linear lesion in pulmonary veins isolation	86
6.4.3	Incomplete ablation line in clinical study	86
6.5	Simulation protocol	87
6.5.1	Initiation of AF and application of ablation patterns	87
6.5.2	Measure of organization	88
6.6	Impact of initial conditions	89
6.7	Comparison of the efficiency of ablation patterns	89
6.7.1	Standard maze patterns	90
6.7.2	Simpler surgical/RF patterns	91
6.7.3	Imperfect Maze-III procedure	95
6.7.4	Isolation of pulmonary veins	97
6.7.5	Comparison of simulations with clinical data	97
6.7.6	Proposition of an ideal ablation pattern	98
6.7.7	Limitations	99
6.8	Conclusions	100
7	Therapeutic pacing	101
7.1	Introduction	101
7.2	Pacing methods	103
7.2.1	Introduction	103
7.2.2	Pacing algorithms	103
7.2.3	Pacing rates and pacing sites	106
7.2.4	Evaluation of pacing efficiency	107
7.3	Pacing atrial flutter	109
7.3.1	Pacing AFL in the 3D homogeneous monolayer model	109
7.3.2	Pacing AFL in the 3D inhomogeneous multilayer model	109
7.4	Pacing atrial fibrillation	112
7.4.1	Pacing chronic AF	112
7.4.2	Pacing meandering AF	116
7.4.3	Pacing cholinergic AF	118
7.5	Conclusions	120

8 Conclusion	123
8.1 Summary of achievements	124
8.2 Perspectives	125
 Bibliography	 127
 Index	 141
 Curriculum vitae	 143

Version abrégée

LA fibrillation auriculaire (FA) est le type le plus répandu d'arythmie. Elle affecte environ 2% de la population totale et 8% à 11% des personnes âgées de plus de 65 ans.

Jusqu'à présent, le traitement de l'arythmie auriculaire a toujours été basé sur des considérations empiriques et habituellement réalisé lors d'études cliniques ou lors d'expériences animales. Les inconvénients majeurs de telles expériences résident dans la difficulté d'accéder à l'ensemble des oreillettes et à la différence entre l'anatomie animale et humaine.

Durant ces dernières années, la puissance toujours croissante des ordinateurs a permis le développement d'un modèle biophysique des oreillettes humaines. Récemment, il est devenu possible de simuler la propagation électrique résultant de l'activité cellulaire dans toutes les parties du cœur humain. Comparée aux études cliniques et animales, l'approche *in silico* a l'avantage d'être reproductible et de présenter des conditions contrôlées.

Dans cette thèse un modèle biophysique des oreillettes humaines est utilisé pour l'investigation des thérapies auriculaires suivantes: les ablations chirurgicales et les stimulations électriques.

Premièrement, les concepts utilisés pour la modélisation biophysique des oreillettes humaines sont passés rapidement en revue. Les différents types d'arythmie pouvant être générés avec un tel modèle sont présentés.

Deuxièmement, des mesures d'organisation ont été développées pour évaluer et classifier les différents types de FA. L'organisation de la FA est évaluée à partir des électrocardiogrammes aussi bien qu'à partir du potentiel transmembranaire des cellules. Quatre types d'arythmies ont été différenciés avec le modèle biophysique : le flutter, la FA chronique, la FA méandreuse et la FA cholinergique.

Finalement, les simulations de thérapies auriculaires ont été investiguées. Le modèle biophysique a été employé pour évaluer l'efficacité des lignes d'ablation, en particulier la procédure Maze-III a prouvé son efficacité dans le traitement de la FA chronique. Cependant, en raison des difficultés techniques et des risques d'une telle procédure, des lignes d'ablation moins invasives ont été proposées. Les résultats des simulations ont confirmé la supériorité des procédures agressives pour terminer la FA, tel que décrite dans les études cliniques. En outre, un modèle de lignes d'ablation idéal a été proposé à l'aide du modèle. Un modèle idéal doit être capable d'empêcher la FA avec un nombre limité

de lignes d'ablation et une longueur minimale, en tenant compte de la maintenance ou du rétablissement de l'activité mécanique des deux oreillettes pendant le rythme cardiaque normal.

La deuxième approche thérapeutique examinée est la stimulation électrique à basse énergie. Un algorithme de stimulation thérapeutique est proposé et testé pour différentes positions des électrodes. Les simulations montrent que les arythmies plus organisées comme le flutter peuvent être terminées par stimulation. Par contre, seulement un contrôle local est observé pour les FA plus complexes. Les résultats obtenus avec le modèle biophysique sont en accord avec les études cliniques.

Les résultats obtenus de cette recherche prouvent que les thérapies auriculaires peuvent être étudiées par un modèle biophysique des oreillettes humaines. Cet outil peut être employé à examiner plus en détail les techniques thérapeutiques afin d'améliorer la qualité de vie des patients.

Abstract

THE most common type of sustained arrhythmia is atrial fibrillation (AF), affecting about 2% of the general population and 8% to 11% of the elderly, more than 65 years of age.

The treatment of atrial arrhythmia is still based on empirical considerations and is usually evaluated in clinical studies or in animal experiments. The main drawbacks of animal experiments lie in the difficulty of technically accessing the whole atria and in the differences between animal and human anatomy.

In the last years, ever-increasing computer power has permitted the development of biophysical models of the human atria. It has become possible to simulate cellular electrical propagation in the whole human heart. Compared to clinical and animal studies, an *in silico* approach has the advantages of repeatability and reproducibility under controlled conditions.

In this thesis, a biophysical model of the human atria has been used to investigate therapies of atrial arrhythmias: surgical ablation and therapeutic pacing.

First, a brief review of the concepts of biophysical modeling of human atria developed until now is presented, as well as a brief description of several types of arrhythmia that can be simulated with the biophysical model.

Second, measures of organization are considered to quantify and classify the different types of AF. With these measures, AF organization is evaluated at the electrogram signals level as well as at the cellular level. Four types of atrial arrhythmia are differentiated with the use of the biophysical model: atrial flutter, chronic AF, meandering AF and cholinergic AF.

Finally, simulations of atrial therapies are investigated. The biophysical model has been used to test the efficacy of ablation lines. The surgical Maze-III procedure has proven to be highly effective in treating chronic AF. However, due to the technical difficulty and the risk of the procedure, less invasive ablation techniques have been investigated. The results confirm the superiority of aggressive surgical procedures in the termination of AF, as described in the clinical studies. Furthermore, an ideal ablation pattern has been proposed using the biophysical model. The ideal pattern should be able to prevent AF with a limited number of ablation lines of minimal length, while allowing for the maintenance or recovery

of mechanical activity of both atria during sinus rhythm.

The second therapeutic approach investigated is that of pacing. An algorithm of pacing and different pacing sites are investigated during this research. Antitachycardia pacing on different types of AF are carried out. The simulations showed that more organized arrhythmia such as atrial flutter can be pace-terminated. On the other hand, only local capture is possible on more complex AF. The results obtained with the biophysical model are in agreement with the clinical studies.

The results of the present research prove that atrial therapies can be approached by means of a biophysical model of the human atria. This tool can be used to investigate further therapeutic techniques and thus, improve the quality of life of patients.

Symbols and Acronyms

Principal symbols

α_y	Opening rate of generic gating variable
β_y	Closing rate of generic gating variable
σ_l	Conductance velocity longitudinal [cm s^{-1}]
σ_t	Conductance velocity transverse [cm s^{-1}]
$\theta(\vec{r}, t)$	Phase variable [rad]
ρ	Resistivity [$\Omega \text{ cm}$]
λ	Wavelength [cm]
μ	Eigenvalue
Φ_e	Extracellular potential [mV]
Φ_i	Intracellular potential [mV]
c	Conductance velocity [cm s^{-1}]
C_m	Membrane capacitance [$\mu\text{F mm}^{-2}$]
$CEig_{95\%}$	Number of principal components needed to obtain 95% of the energy (4.5)
$CEnt$	Quantifies the flatness of the eigenvalue distribution (4.6)
\mathbf{D}_e	Extracellular conductivity tensor [S cm^{-1}]
\mathbf{D}_i, \mathbf{D}	Intracellular conductivity tensor [S cm^{-1}]
F	Faraday's constant: 9.649104 [C mol^{-1}]
\bar{g}_k	Maximum conductance of the ion channel k [mS cm^{-2}]
G_k	Conductance of the ion channel k [mS cm^{-2}]
I_m	(Sum of) transmembrane currents [$\mu\text{A cm}^{-2}$]
I_{stim}	Transmembrane stimulus current [$\mu\text{A cm}^{-2}$]
R	Gas constant: 8.314 [$\text{J mol}^{-1}\text{K}^{-1}$]
S_v	Surface-to-volume ratio [μm^{-1}]
t	Time [ms], [s]
T	Absolute temperature [K]
V_m	Transmembrane potential [mV]

z Valence of the ions

Acronyms

1D/2D/3D	1 or 2 or 3 Dimension(al)
ABBI	Average beat-to-beat interval
AF	Atrial fibrillation
AFL	Atrial flutter
APD	Action potential duration
AVN	Atrio-ventricular node
BB	Bachmann's bundle
BBI	Beat-to-beat interval
CCW	Counterclockwise flutter
CL	Cycle length
CS	Coronary sinus
CT	Crista terminalis
CTI	Cavotricuspid isthmus dependent
CTI	Cavotricuspid isthmus
CRN	Courtemanche-Ramirez-Nattel
CW	Clockwise flutter
DI	Diastolic interval
DWT	Double wave reentry flutter
ECG	Electrocardiogram
ERP	Effective refractory period
FO	Fossa ovalis
IIR	Intraisthmus reentry flutter
IVC	Inferior vena cava
LA	Left atrium
LAA	Left atrium appendage
LLR	Lower-loop reentry flutter
LRI	Luo-Rudy I
LRII	Luo-Rudy II
MV	Mitral valve
PM	Pectinate muscles
PV	Pulmonary vein
RA	Right atrium
RAA	Right atrium appendage

RF	Radiofrequency
SAF	Sustained atrial fibrillation
SAN	Sinoatrial node
SVC	Superior vena cava
TAFT	Time to AF termination
TMPDM	Transmembrane potential distribution map
TV	Tricuspid valve
ULR	Upper loop reentry
UFP	Unstable fixed point

List of Figures

2.1	Transport pathways through the cell membrane and the basic mechanism of transport	13
2.2	Electrical response of cardiac cells	14
2.3	Definition of APD-DI for the Luo-Rudy membrane kinetics model	15
2.4	Geometry of human atria based on MR images	21
2.5	Geometry of the multilayer 3D atria showing the position of the atrial bundles	22
3.1	Activation time map and isochrones during normal sinoatrial propagation. .	26
3.2	Flutter in the monolayer model: action potential and restitution curve using the CRN membrane kinetics model	29
3.3	Initiation of atrial flutter using the CRN membrane kinetics model.	30
3.4	Atrial flutter using the CRN membrane kinetics model (at 4 s)	31
3.5	Atrial flutter using the Courtemanche model (at 5 s)	32
3.6	Atrial flutter pathway using the 3D model	34
3.7	Atrial flutter using the 3D model: TMPDM	35
3.8	Flutter on the multilayer 3D model: action potential and restitution curve using the CRN membrane kinetics model	35
3.9	Chronic atrial fibrillation: action potential and restitution curve	37
3.10	Chronic AF in isotropic tissue using the LRI membrane kinetics model . . .	38
3.11	Atrial fibrillation restitution curve using the CRN membrane kinetics model	39
3.12	Meandering AF in isotropic tissue using the Courtemanche model.	40
3.13	Cholinergic AF in isotropic tissue using the Courtemanche model.	41
4.1	Local high density mapping	48
4.2	Global high density mapping with respect to split level	49
4.3	Spatial correlation at the anterior right atrium.	52

4.4	Measure of complexity as a function of the split level using no filtered electrogram signals	53
4.5	Measure of complexity as a function of the split level using filtered electrogram signals	53
4.6	Measures of complexity over time using filtered electrogram signals	54
5.1	Illustration of the meaning of the phase variable	59
5.2	Phase space in function of different time delay τ	59
5.3	(A) Transmembrane potential distribution map. (B) Its corresponding phase map	60
5.4	Phase variable on a triangular mesh.	62
5.5	Determination of the rotation direction at veins/valves using the sign of a scalar product	63
5.6	Illustration of true and false phase singularities detected when several singularities are anchored around a macroscopic anatomical obstacle	64
5.7	Illustration of a jumping phase singularity	65
5.8	Illustration of an exclusion of a PS already assigned	66
5.9	Illustration of the constraint on the creation of new trajectories starting at an orifice	67
5.10	Illustration of the weaknesses on the constraint on the creation of new trajectories at vein orifice or valve ring	67
5.11	Time evolution of phase singularities.	68
5.12	Phase singularities in the septum	69
5.13	Distribution of PSs with respect to G_{si}	70
5.14	Lifespan histogram	71
5.15	Illustration of provenance of long-lasting PSs	72
5.16	Phase singularities localizations.	73
5.17	Phase singularities trajectories	75
6.1	Ablation line implementation.	81
6.2	Standard maze patterns	82
6.3	Simpler surgical/RF patterns.	83
6.4	Isolation of the pulmonary veins	84
6.5	Modified Maze III patterns	85
6.6	Ablation gap types.	86
6.7	Imperfect Maze-III procedure.	86
6.8	Initial conditions selected for the application of ablation patterns.	88

6.9	TAFT vs. percentage of excited tissue and TAFT vs. Number of initial wavelets	89
6.10	Percentage of success rate and distributions of the average beat-to-beat intervals (ABBI) for each of the standard maze procedures	91
6.11	RID-Maze uncommon flutter	92
6.12	Percentage of success rate and distributions of the average beat-to-beat intervals (ABBI) for each of the 11 simpler ablation patterns studied.	94
6.13	Uncommon flutter around mitral valve.	96
6.14	Percentage of cardioversions vs. TAFT for the modified Maze III patterns	99
7.1	Excitable gap	104
7.2	Flow chart of the closed-loop pacing algorithm	106
7.3	BBI histograms	107
7.4	Pacing sites	108
7.5	Unsuccessful termination of AFL pacing.	110
7.6	Pacing atrial flutter in the right atrium	111
7.7	Pacing atrial flutter: reentry in the isthmus	112
7.8	Spatial correlation during pacing of chronic AF	113
7.9	Measure of complexity during pacing of chronic AF.	113
7.10	Pacing in the right atrium free wall during chronic AF	114
7.11	Decrementing the pacing rate after control during chronic AF	115
7.12	Pacing in superior septum during chronic AF	116
7.13	Spatial correlation during pacing of meandering AF	117
7.14	Measure of complexity during pacing of meandering AF	117
7.15	Pacing in the septum (site S ₄) during meandering AF	119
7.16	Spatial correlation during pacing of chronic AF	119
7.17	Measure of complexity during pacing of cholinergic AF	120

List of Tables

2.1	Mathematical membrane kinetics models: continuous equation representations	12
2.2	Ionic currents in the LRI membrane kinetics model.	17
2.3	Ionic currents in the CRN membrane kinetics model.	18
2.4	Dimensions of the atrial geometry	21
4.1	Main methods to analyze atrial fibrillation.	47
5.1	PSs lifespan for different values of G_{si} for the LRI membrane kinetics model.	72
5.2	PSs lifespan for different types of Inhomogeneities.	75
6.1	Mean TAFT for the standard maze procedure patterns.	90
6.2	Mean TAFT for the simpler patterns.	93
6.3	Effect of discontinuities in the Maze-III: mean TAFT and percentage of successful termination.	95
6.4	Pulmonary veins isolations. Simulations performed with a gap are denoted with W.G.	97
6.5	Comparison between clinical data and biophysical simulations.	98
6.6	Statistic for the modified Maze III patterns.	99

Dissertation

Introduction

1

1.1 Motivations and problem statement

Atrial fibrillation

THE heart is the main organ of the cardiovascular system. Its role is to provide the body with the blood and oxygen it needs to function properly. It is divided into four chambers or cavities. The upper chambers, called *atria*, collect blood returning to the heart. The right atrium accumulates blood from the body that is poor in oxygen and the left atrium receives blood replenished with oxygen from the lungs. The atria empty blood into the lower chambers, respectively right and left ventricles. The blood in the right ventricle is passed into the lungs to be reoxygenate and the blood in the left ventricle is pumped out to the rest of the body.

During a normal heart beat, an electrical impulse originates in the right atrium in the sinoatrial node (SAN), the intrinsic pacemaker, and spreads throughout both the right and left atria and down the interatrial septum to the atrioventricular node (AVN). The impulse slows down briefly at the AVN and then travels down a common pathway, the His bundle, splitting off into the left and right bundle branches located in both ventricles. This electrical activation causes the muscular contraction, which allows the ejection of the blood through the cardiovascular system. The whole process is repeated at a rate of 60 to 100 beats per minute.

When the heart does not beat at a steady rate, the episodes are called *arrhythmias*. If the heartbeat is too slow, it is called a *bradyarrhythmia* or *bradycardia*. If it is too fast, it is called a *tachyarrhythmia* or *tachycardia*. However, depending on the part of the heart affected, the consequences for the person involved are quite different. The most serious

cardiac rhythm disturbance is called *ventricular fibrillation*. Here, the ventricles quiver, which is due to a chaotic, uncoordinated electrical activity and the heart is prevented from pumping, leading inevitably to cardiac arrest and sudden death.

The most common type of sustained arrhythmia is *atrial fibrillation* (AF), which affects about 2% of the general population and 8-11% of those older than 65 years of age and its incidence is increasing [1, 2]. Typically, AF is characterized by an unsynchronized electrical activity that travels in spinning wavelets across both atria, causing these upper chambers to quiver or to fibrillate at a rate of 300 to 600 times per minute. If abnormalities occur in the heart's electrical impulses, the heart is not able to pump the blood out sufficiently well, and as a result blood may pool and clot. If a blood clot moves to an artery in the brain, AF can lead to a stroke. AF is also associated with increased risks of congestive heart failure and cardiomyopathy.

Atrial fibrillation can be divided into *acute* and *chronic* forms [1]. Acute AF generally refer to AF lasting less than 48 hours, and has a high likelihood of a successful conversion to sinoatrial rhythm. There are three types of chronic forms: *paroxysmal*, *persistent* and *permanent*. Paroxysmal atrial fibrillation is defined as recurrent episodes of spontaneously terminating atrial fibrillation. Persistent atrial fibrillation is defined by the persistence of the arrhythmia until cardioversion, the process that converts AF back to normal rhythm. Permanent atrial fibrillation is refractory to attempts at cardioversion. Thus, cardioversion is used only in cases of acute and chronic persistent atrial fibrillation and not in cases previously demonstrated to be refractory.

Current therapies

Several approaches are used to treat and prevent an abnormal beating of the heart, depending on the course of AF. In the current state, methods to prevent AF and restore sinus rhythm are: medication, surgical procedure, radiofrequency catheter ablation and electrical stimulation. Medications are used to slow down the rapid heart rate associated with AF. These treatments may include drugs such as digoxin, beta blockers, quinidine, etc. Surgical or radiofrequency catheter ablation may be effective in some patients when medications fails to work. A surgical incision or a burst of radiofrequency energy is delivered to destroy tissue that triggers abnormal electrical signals or to block abnormal electrical pathways. Electrical cardioversion may also be used to restore normal heart rhythm by means of an electric shock, or an atrial pacemaker can be implanted to regulate the heart rhythm.

Investigation approaches

These days, *simulation* has been adapted for a wide variety of contexts: basic science, life science, engineering, economy etc. Simulation is the process of designing a *model*¹ of a real or imagined *system*² and the conducting of experiments with that model. The

¹A model is a simplified description of a complex entity or process.

²A system is an assemblage of inter-related elements comprising a unified whole.

purpose of simulation experiments is to understand the behavior of the system or evaluate strategies for the operation of the system [3]. Models have been constructed for almost every system imaginable such as: factories, communications, computers networks, integrated circuits, highway systems, flight dynamics, national economies, social interactions, and virtual worlds. The modeling of systems has proved to be more cost effective, less dangerous, faster or otherwise more practical than experimenting with real systems. On the other hand, a model is not a faithful representation of the real system due to the availability of data for describing the behavior of the system. This issue must be addressed prior to the design of the model to minimize its impact once the model is completed. For this reason, simulations usually do not provide an exact solution for a specific situation but merely an indication of general trends.

The various treatments of atrial arrhythmia remain largely based on empirical considerations. Thus new approaches to investigate and understand AF are clearly required. That is why numerical models to simulate AF have been proposed to answer questions such as the mechanism involved in AF initiation or perpetration and the efficiency of therapy techniques. Despite their inherent limitations, this due to trade-offs between accuracy of the representation of atrial electrical activity details and computation requirements, a biophysical model provides a framework to test hypotheses and suggest new experimental or clinical studies and atrial therapies.

In the early days, only a small patch of tissue was modeled, with highly simplified electrical propagation properties. Thanks to advances in the development and improvement of various technologies, it has been possible to design more realistic models. These new techniques have assisted investigations from the molecular level (*e.g.*, patch clamp techniques) to the whole organ (*e.g.*, MR images).

The integration of current knowledge from various fields such as math, engineering, biology and medicine have led to the implementation of a biophysical model of the human atria. Biophysical models (experiments performed *in silico*) have several advantages when compared to animal or human experiments (experiments performed *in vitro*):

- reproducibility of the experiments and results;
- full access to data compared to a small set of parameters accessible in electrophysiological experiments;
- uncoupling of several phenomena, due to the fact that it is possible to control each parameter individually.

Objectives

The work presented in this thesis is a part of a larger project attempting the establishment of a general research framework for AF. It is the continuation of the two previous theses accomplished by Olivier Blanc in 1998 [4] and Vincent Jacquemet 2004 [5]. With an additional contribution by Steeve Zozor in 2003 [6]. This above mentioned research focused

mainly on the development of a biophysical model of the human atria: development of an atrial geometry, implementation of membrane kinetics models and to study of electrogram signal morphology. Based on this biophysical model of the human atria the objectives of this present study are:

- to characterize different types of AF, which can be generated by the biophysical model of human atria;
- to investigate the effectiveness of surgical and radiofrequency catheter therapies;
- to investigate electrical therapies, particularly atrial antitachypacing.

The present research presented here has been realized in the framework of a project linking Medtronic Europe, the Service of Cardiology of the Vaud University Hospital and the Signal Processing institute Laboratory of the Swiss Federal Institute of Technology, with the support of the Commission for Innovative Technology and the Theo-Rossi-Di-Montelera Foundation.

1.2 Organization of the dissertation

The dissertation is organized in eight chapters, divided into three main parts:

Part I (chapter 2-3): The first chapter (chapter 2) reviews briefly the biophysical modeling of human atria. The concepts of cell excitability and action potential are introduced. An overview of modeling atrial tissue and electrical propagation is presented using a bottom-up approach, starting from the microscopic level with membrane kinetics models and carries through to the organ level. Two membrane kinetics models (Luo-Rudy I and Courtemanche-Ramirez-Nattel), which are used throughout this work, are summarized. The second chapter (chapter 3) presents the different type of AF, which can be generated with such a biophysical model. First, simple arrhythmia such as *atrial flutter* is presented and then more complex arrhythmias lasting from several seconds up to several minutes of simulated time are discussed.

Part II (chapter 4-5): The second part describes several methods to measure and quantify the spatio-temporal organization during atrial fibrillation. Chapter 4 presents a measure of organization based on simulated electrogram signals computed on the surface of the atria. Local and global atrial activity during AF are quantified by a high density mapping system, as well as by electrodes placed uniformly on the surface of the atrial geometry. In addition, chapter 5 describes spatio-temporal organization at the cellular level. The mechanisms responsible for AF perpetuation are analyzed for different types of AFs.

Part III (chapter 6-7): The last part of this dissertation investigates atrial therapies. Chapter 6 concentrates on the effect of different ablation patterns during chronic AF. The protocol of ablation lines are described as well as the modeling of the lines. The results are compared with those obtained from clinical studies. Chapter 7 shows results of electrical

stimulation during different type of arrhythmia. First, a new algorithm of electrical stimulation is presented. Then it is used to pace several types of arrhythmias in the biophysical model.

Finally, chapter 8 concludes the dissertation with a summary of this research and its possible future extensions.

1.3 Original contributions

The major contributions¹ of the research presented in this dissertation are summarized as follows.

- Simulation of atrial arrhythmias (chapter 3):
 - simulation of atrial flutters.
- Measures of organization (chapter 4-5):
 - implementation of algorithm to measure organization during different type of AF;
 - phase singularities tracking during AF.
- Investigation of ablation procedure (chapter 6):
 - implementation of ablation procedure;
 - comparison between standard ablation procedures;
 - study of simpler ablation patterns;
 - validation of the biophysical model with clinical data;
 - proposition of an ideal ablation pattern;
- Investigation of pacing (chapter 7):
 - detection of pacing gap;
 - implementation of pacing algorithms;
 - pacing of atrial flutter;
 - pacing of atrial fibrillation.

¹See also the list of publication in the curriculum vitae attached at the end of the dissertation.

Part I

A biophysical model of the human atria

The first part of this thesis presents the biophysical modeling of human atria. Its first chapter (chapter 2) reviews briefly the concepts developed until now in previous works: cardiac cell properties and mathematical formulations. The second chapter (chapter 3) is focused on the different types of arrhythmia that can be reproduced by means of the biophysical model.

From the cell to the biophysical model

2

2.1 Introduction

SINCE the last century, the development and improvement of various technologies have allowed scientists to gain a better understanding of the function of the heart. These new techniques have assisted the investigations from the molecular level (*e.g.*, patch clamp techniques [7]) to the whole organ (*e.g.*, MR images [8]). A broader understanding has led to the development of a number of mathematical models (table 2.1) based on these experimental investigations, which can successfully simulate the form and functions of the heart, as we currently understand them. These models can be separated into two fields: the cell structures or the membrane kinetics modeling and the entire cardiac system modeling. Prior research has been devoted mainly to the modeling of the ventricles, due to the fact that its dysfunctionality can directly lead to death.

It is only since the 1960s that scientists have focused their interest on the modeling of atrial electrical activities: Moe (1964) [9], Macchi (1974) [10], Kafer (1991) [11], Killmannn (1991) [12], Lorange (1993) [13], Wei (1995) [14], Gray (1998) [15], Blanc (1999) [16], Ellis (2000) [17], Zemlin (2000) [18], Harrild (2000) [19], Vigmond (2001) [20], Virag (2002) [21], Höper (2003) [22].

This chapter reviews the biophysical model of the atria that was initiated by Olivier Blanc [4] in 1998, developed by Steeve Zozor [6] and Vincent Jacquemet [5] in 2000. The bottom-up approach was used to model the electrical activity of the atria. Firstly the cellular properties of this model are presented. Subsequently, the tissue level and the whole organ is exposed.

Action potential models	Domains	Year
Nerve action potential model		
Hodgkin Huxley	Squid giant axon	1952
Cardiac action potential models		
FitzHugh-Nagumo	Cardiac action potential model	1961
Noble	Purkinje fiber	1962
Bassingthwaighte	Cardiac excitation contraction	1973
McAllister-Noble-Tsien	Calf Purkinje fibre	1975
Beeler-Reuter	Calf ventricular fiber	1976
DiFrancesco-Noble	Ventricular fibre	1984
Luo-Rudy	Guinea pig ventricle	1991
Demir-Giles	Sinoatrial node	1998
Courtemanche-Ramirez-Nattel	Human atria	1998
Nygreen <i>et al.</i>	Human atria	1998
Winslow <i>et al.</i>	Canine ventricle	1999
Michailova-McCulloch	Canine ventricle	2001

Table 2.1 – *Mathematical membrane kinetics models: continuous equation representations.*

2.2 Modeling the cardiac cell membrane

2.2.1 Cardiac cell properties

The cardiac tissue consists of more than one billion cells; $250 \cdot 10^6$ of which form the atria and about 10^9 the ventricles. Cardiac cells are represented by a cylinder shape of 30-100 μm long and 8-20 μm wide [23]. They are surrounded by a *lipid bilayer*¹ membrane which separates the *intracellular medium* from the *extracellular medium*. The membrane is selective in which molecules or ions are allowed to pass in and out and is, therefore, *semi-permeable*. The different mechanisms involved in the transport of particles are schematically represented in figure 2.1. Transport through the cell membrane occurs either by *passive transport* or *active transport* [7]. Passive transport consists of two types: 1) *simple diffusion* which allows small molecules to cross directly the membrane via diffusion and 2) *facilitated diffusion* which utilizes particular protein channels. Active transport is also divided into two categories: 1) *primary active transport* and 2) *secondary active transport*. Primary active transport involves the use of energy (usually through adenosine triphosphate (ATP) hydrolysis) within the membrane protein itself to cause a conformational change that results

¹lipid bilayer is composed of a thin film of lipids only 2 molecules thick that is continuous over the entire cell surface [7].

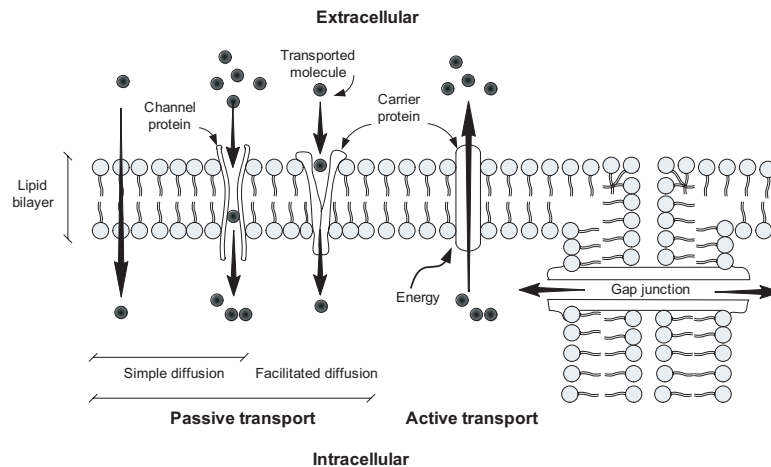


Figure 2.1 – Transport pathways through the cell membrane and the basic mechanism of transport. Passive transport constitutes of simple diffusion and facilitated diffusion. Active transport requires the expenditure of energy to transport molecules across the membrane.

in the transport of the molecule through the protein. Secondary active transport involves using energy to establish a gradient across the cell membrane, and then utilizing that gradient to transport a molecule of interest up its concentration gradient. In both instances, transport depends on *carrier proteins* that penetrate through the membrane, the same as is true for facilitated diffusion. However, in active transport, the carrier protein functions differently from the carrier in facilitated diffusion because it is capable of imparting energy to the transported substance to move it against an electrochemical gradient. Furthermore, intracellular transport flows from one cell to another due to the *gap junctions* that allow relatively free diffusion of ions.

Electrical potential differences are set up across the membrane, determined primarily by three factors: 1) the concentration of ions on the intracellular medium and extracellular medium; 2) the permeability of the cell membrane to those ions (*i.e.*, ion conductance); and 3) by the activity of electrogenic pumps (*e.g.*, Na^+/K^+ -ATPase and Ca^{2+} transport pumps) that maintain the ion concentration differences across the membrane. In any electrical model of a cardiac cell, the ions of primary interest are potassium (K^+), sodium (Na^+), and calcium (Ca^{2+}). At steady-state equilibrium, the difference potential between the intracellular domain and the extracellular domain, also called *membrane potential* or *transmembrane potential* V_m , is maintained approximately at -80 mV.

Cardiac cells become excited when they undergo an external stimuli and produce an *action potential*, which constitutes a rapid change in the membrane potential (figure 2.2). This is a fast, all-or-none signal, which propagates along the surface of the cell and transmits from cell to cell through gap junctions. Once *voltage-gated channels*¹ begin to open, ion influx through them produces further changes in the membrane potential, in turn recruiting

¹Voltage-gated channels are ion channels in a membrane that open and close in response to changes in membrane potential.

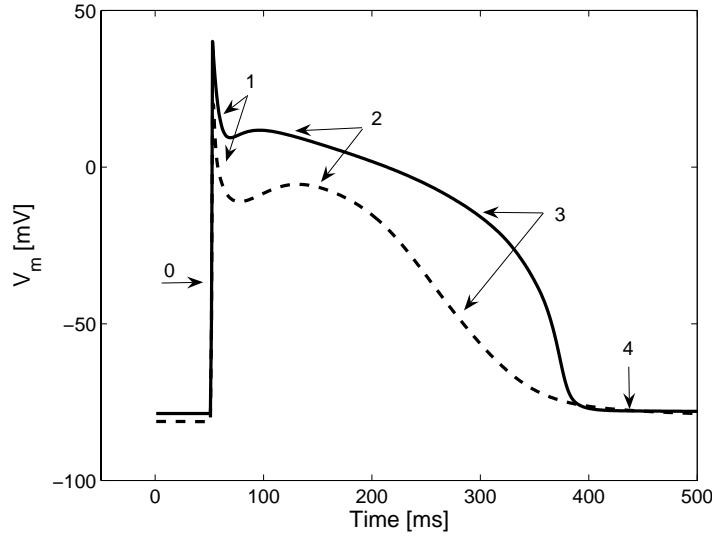


Figure 2.2 – *Electrical response of cardiac cells. The continuous line is a ventricular action potential using the Luo-Rudy [24] membrane kinetics model and the dashed line is an atrial action potential produced by the Courtemanche-Ramirez-Nattel [25] membrane kinetics model. (0) Upstroke, (1) Early repolarization. (2) Plateau. (3) Late repolarization. (4) Resting potential.*

additional channels to open. Ca^{2+} ions move down its electro-chemical gradient introducing positive charges to the cell thus producing additional depolarization which in turn activates more Ca^{2+} channels until the entire population is activated. A similar process activates Na^{+} channels in contractile cells (atrial, ventricular). Thus, a rapid influx of Ca^{2+} or Na^{+} ions produces an inward current which depolarizes the cell membrane synchronously.

When an outside stimulation is applied and reaches a threshold, membrane potential V_m is depolarized following the curve in figure 2.2. Five distinct phases in the time course are defined: (0) Upstroke, (1) Early repolarization. (2) Plateau. (3) Late repolarization. (4) Resting potential.

During the phase (0)-(2) and a part of phase (3), no stimulus can generate a new action potential, this interval is called the *effective refractory period* (ERP).

In order to determine the ERP, several stimuli were applied at different time instants until a new propagation was generated. As this method is time consuming, the *action potential duration* (APD) is used instead and it is related to the ERP [26]. APD is defined as the time interval between the upstroke and 90% of the repolarization level. The APD depends on the previous *diastolic interval* (DI), *i.e.* the time interval between the end of the first action potential (S_1) and the onset of the second one (S_2) (figure 2.3(A)). The relation between APD and DI is described by the *restitution curve* (figure 2.3(B)). The cycle length (CL) is the sum of APD and DI, *i.e.*, the elapsed time between the first and second stimuli.

The APD curve is known to play a crucial role in the initiation and perpetuation of

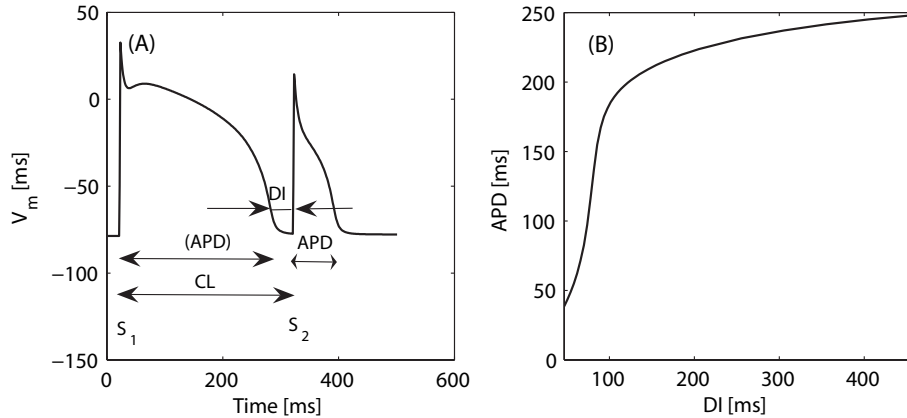


Figure 2.3 – Definition of APD-DI for the Luo-Rudy membrane kinetics model. (A) Action potential duration (APD), diastolic interval (DI) and cycle length (CL). (B) Restitution curve.

*reentrant wave*¹ patterns like the spiral waves that are measured during same type of atrial arrhythmia (see chapter 3 and [27, 28]).

2.2.2 Modeling the active membrane properties

The conception of both realistic and complex models has become possible due to recent advances in experimental technologies and the increase in computing power. When modeling a system, major steps forward have to be taken into account; realistic representation of the logical process and computation costs. Simplifications and approximations are needed to ensure reasonable computation time, while keeping the representation precise enough.

In the case of the cardiac cell, the active transport mechanism is generally neglected and gap junctions are considered as passive and non-selective ionic exchangers. Based on a number of experiments in giant squid axons, Hodgkin and Huxley [29] implemented the first quantitative model of electrical excitability of neurons. This model describes three ionic currents: fast inward sodium current, time-dependent outward potassium current, and time-independent leakage current. The total transmembrane current I_m can be expressed as:

$$I_m = C_m \frac{dV_m}{dt} + I_{ion} - I_{stim}, \quad (2.1)$$

where C_m is the transmembrane capacitance, V_m is the difference between the intra- and extra-cellular potential (Φ_i and Φ_e):

$$V_m = \Phi_i - \Phi_e, \quad (2.2)$$

I_{ion} is the sum of the ion currents and I_{stim} , an external stimulation current. In the case of an isolated cell, by conservation of current, $I_m = 0$. The transmembrane potential can be

¹A reentrant wave is a circulating excitation wave in the heart, rather than moving outward and then stopping.

written as:

$$\frac{dV_m}{dt} = -\frac{1}{C_m}(I_{\text{ion}} - I_{\text{stim}}). \quad (2.3)$$

Each of the individual currents summed under the term I_{ion} has the form:

$$I_k = \bar{g}_k y(V_m - E_k). \quad (2.4)$$

I_k is the current associated with the ion of type k , \bar{g}_k is the maximum conductance of the corresponding ion channels, y a *gating variable* ($0 \leq y \leq 1$) expressing the mean state of these ion channels. The term E_k represents the Nernst potential [7] of an ion of the type k given by:

$$E_k = \frac{RT}{zF} \cdot \ln \left(\frac{[k]_e}{[k]_i} \right), \quad (2.5)$$

with R the universal gas constant, T the absolute temperature, z the valence of ion k , F , Faraday's constant and $[k]_e$ and $[k]_i$ the extracellular and intracellular ion concentrations.

The transition of the gating variable y between the closed ($y = 0$) and opened states ($y = 1$) can be written:



where the gate rate α_y and β_y in ms^{-1} correspond respectively to the opening and closing of the ion channels. In an intermediate state, the fraction of gates open (or in their α state) is y . Then the fraction of gates closed (or in their β state) is $1-y$. The change in the fraction of the gates open is hence governed by:

$$\frac{dy}{dt} = \alpha_y(1 - y) - \beta_y y. \quad (2.7)$$

The temporal evolution of the gating variable y is thus described by this first order differential equation. This process of the opening and closing of the gates is called *gate kinetics*.

The following sections summarize each of the two membrane kinetics models used in this particular research.

The Luo-Rudy membrane kinetics model

The Luo–Rudy membrane kinetics model [24] is the next significant update to the Beeler–Reuter [30] mammalian ventricular model. It is known as the Luo-Rudy I (LRI) model because it is the first of the two Luo–Rudy models. The total current I_{ion} is composed of six individual currents and eight gating variables:

$$I_{\text{ion}} = I_{\text{Na}} + I_{\text{si}} + I_{\text{K}} + I_{\text{K1}} + I_{\text{Kp}} + I_{\text{b}}. \quad (2.8)$$

Each individual ion current is handled by gate kinetics equations of the form (2.7) and table 2.2 presents the main characteristics of each current.

Current	Time dependency	Direction	Gating variables
Sodium channel			
I_{Na}	Yes	Inward	m, h, j
Calcium channel			
I_{si}	Yes	Inward	d, f
Potassium channels			
I_K	Yes	Outward	X, X_i
I_{K1}	No	Outward	$K1$
I_{Kp}	No	Outward	
I_b	No	Outward	

Table 2.2 – *Ionic currents in the LRI membrane kinetics model.*

An improved version of this model, the Luo-Rudy Phase II (LRII) model was published in 1994 [31]. The main improvement to the previous version was the inclusion of intracellular ionic *homeostasis*,¹ for sodium and potassium.

The Courtemanche-Ramirez-Nattel membrane kinetics model

The Courtemanche-Ramirez-Nattel membrane kinetics model (CRN) [25] is based on the Luo-Rudy II one and it attempts to simulate action potentials of human atria. This model includes the dynamics of intracellular currents of the *sarcoplasmic reticulum*² (SR) and the *non-junctional sarcoplasmic reticulum* (NSR). The total current I_{ion} is composed of twelve individual currents:

$$I_{ion} = I_{Na} + I_{Na,b} + I_{K1} + I_{to} + I_{Ks} + I_{Kr} + I_{Kur} + I_{Ca,L} + I_{Ca,b} + I_{p,Ca} + I_{NaK} + I_{NaCa}. \quad (2.9)$$

The ionic gating variables corresponding to each current are all governed by differential equations as formulated by (2.7). The details of each current are fully described in [25]. Table 2.3 summarizes the main properties of each current.

2.3 Modeling myocardial tissue

2.3.1 The bidomain model

Recently, the bidomain model has been widely accepted as the most widely used approach for theoretical and numerical investigations of macroscopic electric phenomena in cardiac tissue [32, 33]. It is based on the representation of tissue as two interpenetrating domains:

¹The ability to maintain a relatively constant internal environment

²A sarcoplasmic reticulum is a membrane network within the cytoplasm of muscle cells involved in the synthesis, modification, and transport of cellular materials.

Current	Time dependency	Direction	Gating variables
Sodium channels			
I_{Na}	Yes	Inward	m, h, j
$I_{\text{Na,b}}$	No	Inward	
Potassium channels			
I_{K1}	No	Inward	
I_{to}	Yes	Outward	o_a, o_i
I_{Ks}	Yes	Outward	x_s
I_{Kr}	Yes	Outward	x_r
I_{Kur}	Yes	Outward	u_a, u_i
Calcium channels			
$I_{\text{Ca,L}}$	No	Inward	d, f, f_{Ca}
$I_{\text{Ca,b}}$	No	Inward	
Pumps			
$I_{\text{p,Ca}}$	No	Outward	
I_{NaK}	No	Outward	
Ion exchanger			
I_{NaCa}	No	Inward	
Sarcoplasmic reticulum fluxes			
I_{leak}	No	NSR \rightarrow I	
I_{up}	No	I \rightarrow NSR	
I_{tr}	No	NSR \rightarrow JSR	
I_{rel}	Yes	JSR \rightarrow I	u, v, w

Table 2.3 – Ionic currents in the CRN membrane kinetics model. NSR: network sarcoplasmic reticulum. JSR: junctional sarcoplasmic reticulum. I: intracellular space.

the extra- and the intracellular domain. The current flows are described by the coupled reaction-diffusion equations constituting the bidomain model:

$$\frac{1}{S_v} \nabla \cdot (\mathbf{D}_i \nabla \Phi_i) = I_m, \quad (2.10)$$

$$\frac{1}{S_v} \nabla \cdot (\mathbf{D}_e \nabla \Phi_e) = -I_m, \quad (2.11)$$

where S_v is the cell surface-to-volume ratio, \mathbf{D}_i and \mathbf{D}_e are the intracellular and extracellular conductivity tensors determined by gap junction resistivities and I_m is the transmembrane current per unit area that is a function of the transmembrane potential V_m . The ratio S_v is related to the interaction of two kinds of contributions: volumetric flows through the intra and extracellular spaces and flows through the membrane surface. Because of the continuous nature of the tissue model, the conductivity tensors \mathbf{D}_i and \mathbf{D}_e reflect electrical properties that are spatially averaged over several cardiac cells.

Replacing (2.2) in (2.10) and (2.11), the two following equations describe the current flow in the intracellular domain and the current conservation between the two domains:

$$\frac{1}{S_v} \nabla \cdot (\mathbf{D}_i [\nabla V_m + \nabla \Phi_e]) = I_m, \quad (2.12)$$

$$\nabla \cdot (\mathbf{D}_e \nabla \Phi_e) + \nabla \cdot (\mathbf{D}_i [\nabla V_m + \nabla \Phi_e]) = 0. \quad (2.13)$$

It is assumed that there is no current flow between the intracellular and extracellular domain through the gap junctions:

$$\vec{n}^T \cdot \mathbf{D}_i \nabla \Phi_i = 0, \quad (2.14)$$

where \vec{n} is a unit vector normal to the tissue interface. On the exterior boundary of the bath, corresponding to the body surface a no-flux boundary condition is also assumed:

$$\vec{n}^T \cdot \mathbf{D}_e \nabla \Phi_e = 0, \quad (2.15)$$

In the extracellular domain, in the absence of any source current, it is assumed that:

$$\nabla \cdot \mathbf{D}_e \nabla \Phi_e = 0. \quad (2.16)$$

Other boundary conditions may also be taken into account [32, 34]. For example, when modeling defibrillation, the defibrillation electrodes applied directly to the thorax or through a conductive bath, are considered.

2.3.2 The monodomain model

The numerical resolution of the bidomain equations is not a straightforward task in the general case, it requires the simultaneous computation of the two potential fields Φ_e and V_m [35, 36]. It is fortunately possible to simplify efficiently the bidomain formalism and restrain the computation to the intracellular domain only [23]. A commonly used simplification of the bidomain equations to save computation costs results from assuming that [6]:

- the tissue is thin and lies in an extensive bath;
- the extracellular potential variations are sufficiently small, so that the intracellular potential variations are approximately equal to the transmembrane potential variations;
- the effect of the extracellular potential on the transmembrane current sources is small, so the bidomain equations can be decoupled.

Under these assumptions, a cardiac tissue can be described by a monodomain equation:

$$\frac{1}{S_v} \nabla \cdot (\mathbf{D} \nabla V_m) = C_m \frac{\partial V_m}{\partial t} + I_{\text{ion}} - I_{\text{stim}}, \quad (2.17)$$

where the conductivity tensor \mathbf{D} is equal to \mathbf{D}_i . The no-flux boundary condition in the intracellular domain can be written as:

$$\vec{n}^T \mathbf{D}_i \nabla V_m = 0. \quad (2.18)$$

An alternative way for conceiving a monodomain model is to assume an isotropic tissue or a tissue with a constant ($\mathbf{D}_i = k\mathbf{D}_e$, where k is a constant [5]).

In this context the conductivity tensor can be conveniently expressed as a function of the intracellular tissue resistivity ρ with:

$$\mathbf{D} = \frac{1}{\rho} \mathbf{I}, \quad (2.19)$$

where \mathbf{I} is the identity matrix. By modifying the conductivity tensor field \mathbf{D} , anisotropic conduction can be generated. The conduction velocity (CV) is related to the resistivity ρ , by the approximate law: $\rho \propto CV^{-2}$ [37].

2.3.3 Electrograms

Clinical electrophysiology data of the heart are mainly based on electrical signal recordings such as the electrocardiogram (ECG)¹. Transmembrane potentials of the atria tissue are not directly accessible in clinical studies. Therefore, it is necessary to compute electrical signals measured on the atrial surface (atrial *electrogram signals*), corresponding to endocardial catheter electrode recordings or electrical mappings, to obtain comparable measurements.

The Unipolar electrogram, Φ are computed according to the current source approximation [5]. The extracellular potential at the position \mathbf{x} and at time t is given by:

$$\Phi(\mathbf{x}, t) = \frac{1}{4\pi\mathbf{D}} \int_{\Omega_{epi}} d\mathbf{y} \delta \frac{S_v I_m(\mathbf{y}, t)}{\|\mathbf{x} - \mathbf{y}\|}, \quad (2.20)$$

where Ω_{epi} represents the epicardial surface, $d\mathbf{y}$ is an infinitesimal surface element, δ is the thickness of the tissue, \mathbf{D} the surrounding bath conductivity, I_m the current source per unit area of membrane surface, and S_v is the cell surface-to-volume ratio.

2.4 Geometry of human atria

2.4.1 Monolayer 3D surface

The atrial model is based on MR images acquired from a healthy adult female subject, provided by Medtronic Inc. The surface of the atria was semi-automatically segmented slice-by-slice and a 3D atrial structure was reconstructed. Its coarse, meshed surface represented the epi- and endo-surfaces of the atrial walls with major geometrical problems, such as valve

¹An electrocardiogram is a graphic produced by an electrocardiograph, which records the electrical voltage in the heart in the form of a continuous strip graph. It is constructed by measuring electrical potential differences between various points on the body surface using a galvanometer.

and vein delimitations [4]. Therefore, the surface was refined using 3D splines provided by Ideas[®] (SDRC Inc.). Finally, from the parameterized surface, several triangular meshes of different spatial resolutions ($\Delta x = 0.6$ mm (50'000 nodes) and $\Delta x = 0.4$ mm (100'000 nodes)) were generated [5]. This last one is used to run standard simulations. The final geometry represents a monolayer 3D-surface shown in figure 2.4 including the opening corresponding to all valves and veins, as well as the septum. Table 2.4 summarizes the dimensions of this complex geometry representing the atria.

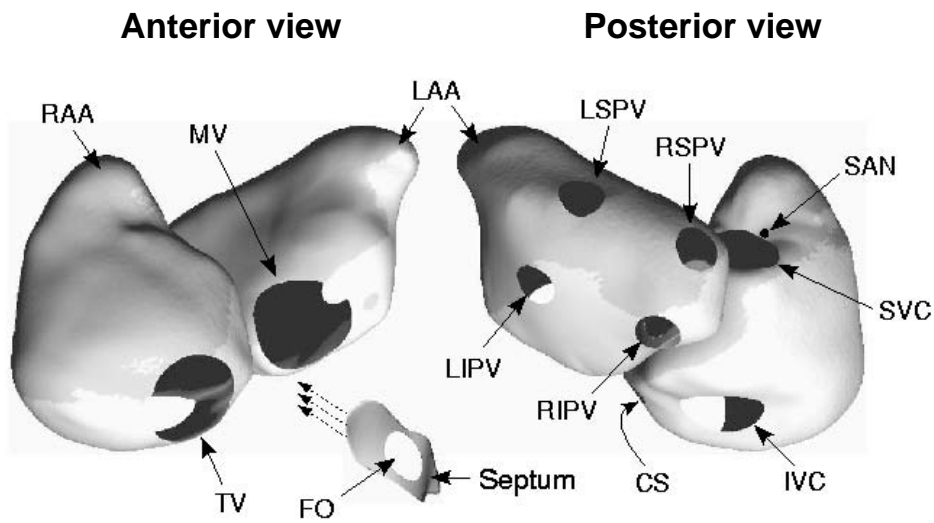


Figure 2.4 – Geometry of human atria based on MR images. The left/right atrium appendages are indicated by LAA/RAA. The major vessels and valves are included: tricuspid valve (TV), mitral valve (MV), inferior vena cava (IVC), superior vena cava (SVC), pulmonary veins (LSPV, RSPV, LIPV and RIPV), coronary sinus (CS) and fossa ovalis (FO). The sinoatrial node (SAN) is represented by a dot.

Right atrium	RA	SVC	IVC	TV	CS	
	84.20	2.84	3.14	4.29	0.54	
Left atrium	LA	LSPV	RSPV	LIPV	RIPV	MV
	72.10	1.07	1.02	0.89	1.08	4.57
Septum	SEPT	FO				
	3.79	1.17				

Table 2.4 – Dimensions of the atrial geometry. The right/left atrium are indicated by RA/LA; dimensions are indicated in cm^2 .

2.4.2 Multilayer 3D structure

Based on the monolayer surface, thickness was first added by duplicating the first layer in the direction perpendicular to the surface. Each vertex was replaced by a cable (1D structured mesh) and the connections between each layer were completed [5].

The current version, also based on the triangular mesh surface Σ , uses a spatial regular discretization. The formulation of the domain Ω representing the atrial wall is:

$$\Omega = \left\{ \mathbf{x} \mid \min_{\mathbf{y} \in \Sigma} \|\mathbf{x} - \mathbf{y}\| < R \right\}, \quad (2.21)$$

where, $R > 0$ is half of the wall thickness and \mathbf{x}, \mathbf{y} are spatial coordinates. The domain is described by computing its intersection with a regular grid:

$$\Omega_{discr} = \Omega \cap \{ \mathbf{x} = (i\Delta x; j\Delta x; k\Delta x) \mid i, j, k \in \mathbb{Z} \}, \quad (2.22)$$

where Δx is the space step. The atrial wall thickness is set to 1.2 mm with a spatial discretization of 300 μm , leading on average to 4-5 layers. The total number of nodes is inferior to 1'000'000, which corresponds to a reasonable computation time. Besides the thickness, fast conduction boundaries such as the crista terminalis (CT), the pectinate muscles (PM) and the Bachmann's bundle (BB) were included in the biophysical model (figure 2.5). These structures were implemented manually based on data from the literature [5, 38, 39].

2.5 Implementation of a biophysical model

The spatial and temporal coupling of the reaction-diffusion process described in (2.17) and (2.18) are spatially and temporally discretized using an unstructured meshed [6] and an adaptive time step [40] method, in the case of the monolayer surface. Whereas, finite difference methods are used for the structured 3D monolayer surface [41, 42].

Equations (2.5) and (2.18) are solved in two stages [40]. Firstly, the diffusion part is considered and secondly the reaction part, which leads to the following set of equations:

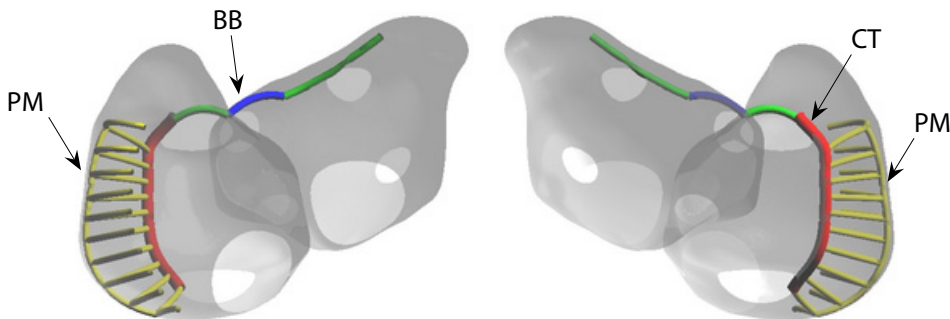


Figure 2.5 – Geometry of the multilayer 3D atria showing the position of the atrial bundles: Crista terminalis (CT), pectinate muscles (PM) and Bachmann's bundle (BB). (Produced by V. Jacquemet)

Diffusion:

$$\frac{\partial V_m}{\partial t} = \frac{1}{C_m S_v} \nabla \cdot (\mathbf{D} \nabla V_m), \quad (2.23)$$

with the no-flux boundary condition:

$$\vec{n}^T \mathbf{D}_i \nabla V_m = 0. \quad (2.24)$$

These equations are solved by means of the forward Euler scheme [4].

Reaction:

$$\frac{\partial V_m}{\partial t} = -\frac{1}{C_m} (I_{\text{ion}} - I_{\text{stim}}), \quad (2.25)$$

which is solved using an adaptive time step to optimize computation time [40].

2.6 Summary

In this chapter, the atrial biophysical model developed in the two previous theses by O. Blanc [4] and V. Jacquemet [5], has been briefly discussed. An overview of modeling methods has been presented using a bottom-up approach. This approach starts from the microscopic level with cellular membrane kinetics models and carries it through to the organ level.

The cellular membrane structure has been presented with its simplifications required for its implementation in a biophysical model. The electrical activity, at steady-state and under an external stimulus, has been discussed. The engendered currents have been exposed and the two membrane kinetics models (the Luo-Rudy I and the Courtemanche-Ramirez-Nattel) used later in this dissertation have been summarized.

The principle of coupled tissue models and their implementations have been touched upon. The geometry of the atria based on MR images has been presented.

This chapter lays down the principles, the terms and the tools that will be used throughout the dissertation.

Simulations of atrial arrhythmias

3

3.1 Introduction

THE goal of this project is the development of a biophysical model of human atrial arrhythmias. The model will first be an instrument to assist electrophysiologists and clinicians to understand more fully the occurrences of arrhythmias and their behavior. Second, it will be used to investigate therapeutic interventions. The state of the art in modeling normal atrial conduction is the work of Harrild and Henriquez [19], entailing a full real 3D atrial structure and the Nygren *et al.* [43] membrane kinetics model. But alas, as pointed by their authors, such a detailed model is not suitable for studying complex arrhythmic propagation because of its computational requirements. In the present study, a tradeoff was made between model complexity and computational load in such a way as to allow several arrhythmias such as atrial flutter (AFL) and sustained atrial fibrillation (AF) to be simulated during several seconds of real time.

The previous chapter described briefly the membrane kinetics models and the atrial geometry used in the biophysical model. In the present chapter, the different types of atrial arrhythmia that can be simulated with such a model are presented. The mechanisms underlying the initiation and the perpetuation of atrial arrhythmias are discussed: action potential duration (APD), restitution curve and heterogeneity. The different dynamics of the several types of arrhythmia are analyzed.

First, the atrial flutter, which is the most organized arrhythmia, is presented using the Courtemanche-Ramirez-Nattel (CRN) membrane kinetics model in the 3D monolayer surface and there afterwards on the 3D multilayer structure. Second, Jacquemet's results [5] on less organized arrhythmia are recapitulated. The experiments were performed using the

Luo-Rudy I (LRI) and the CRN membrane kinetics models in the monolayer surface.

These various types of arrhythmia will be used to investigate atrial therapies in chapter 6 and 7.

3.1.1 Sinoatrial rhythm

In healthy atria, the cardiac rhythm is governed by the sinoatrial node (SAN), the intrinsic pacemaker, which delivers an electrical impulse approximatively every second. This impulse spreads throughout both the right and left atria and down the interatrial septum to the atrio-ventricular node (AVN). The total activation time from the SAN to the left atrium appendage is about 110 ms, as shown in figure 3.1. An example of an electrogram signal complex, computed (see section 2.3.3) in the middle of the right anterior atrium free wall, is displayed (figure 3.1, E_1).

During atrial arrhythmias, this rhythm may be perturbed either by a different pathway used by the wavefront or by multiple wavebreaks.

3.1.2 Atrial flutter

The earliest usage of the term atrial flutter has been attributed to MacWilliam [44], who observed in 1886 a rapid, seemingly regular excitation of the atrium. In 1911, Jolly and Ritchie clearly distinguished AFL from AF: the typical flutter was described as inducing negative sawtooth waves in the electrocardiogram (ECG) leads II, III and aVF [45].

A typical atrial flutter results from a right macro-reentrant circuit bounded anteriorly by the tricuspid valve orifice (TV), posteriorly by the specific arrangement of anatomical obstacles (orifice of the superior vena cava (SVC), the inferior vena cava (IVC) and Eustachian ridge), and functional barriers (regions of the crista terminalis (CT)) [46]. In

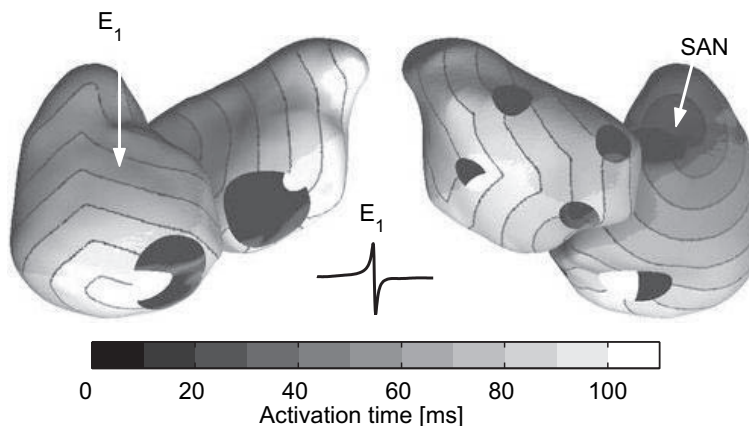


Figure 3.1 – Activation time map and isochrones during normal sinoatrial propagation. Isochrones are drawn in black every 10 ms. The point E_1 denotes the position of the unipolar electrodes used to compute the electrogram. (Reprinted with permission from V. Jacquemet)

humans, the most common direction of activation of the AFL circuit (90%) follows a pathway between TV and IVC along the isthmus in the direction of the septum. This has been described as counter-clockwise reentry and clockwise reentry if the activation occurs in the opposite direction. Depending on the rate of the cycle length (CL), two classes of AFL were initially established: AFL type I and AFL type II. The former one is characterized by an atrial rate ranging from 240 to 340 beats per minute (bpm) and the latter, by an atrial rate ranging from 240 to 433 bpm [47].

More recently, as the result of advanced mapping techniques [48], a new classification and terminology of AFL has been defined [49–51]. The first category regroups right atrium AFL and the second one, left atrium AFL. Right atrium AFL is divided into two subgroups: *cavotricuspid isthmus dependent* (CTI) AFL and *non-CTI dependent* AFL.

In the CTI AFL subgroup, the majority of the flutter circuits involve electrical activation around the tricuspid annulus (TA), and the isthmus represents a critical part of the circuit. Among the CTI AFL, five different types of flutters have been described: counter-clockwise (CCW)/clockwise (CW) atrial flutter, double-wave reentry (DWR), lower-loop reentry (LLR) and intra-isthmus reentry (IIR), whose circuit is bounded by the medial CTI and the coronary sinus ostium; the lateral CTI not being involved [52, 53]. CCW and CW flutters have been detailed in the previous paragraph (AFL type I). The DWR flutter appears if a premature beat is able to invade the circuit. Then two wavefronts may occupy the original circuit. DWR is usually produced by extrastimuli and is usually, short-lived. It may also serve as a trigger for AF. The LLR flutter involves a reentrant circuit around the IVC. This flutter may coexist with a typical CCW or CW flutter and involves posterior break-through(s) across the CT.

In the non-CTI AFL subgroup, electro-anatomic voltage maps from the right atrium often reveal scars, the result of surgical repair of congenital heart defects; or low voltage areas which act as the central obstacle to the reentrant. Tai *et al.* [54] have described an upper loop reentry (ULR), this type of atypical flutter involves the upper portion of the right atrium with transverse conduction over the CT.

The second category, regroups left atrium atrial flutters are far less common than right atrial CTI. Three subgroups have been identified: *mitral annulus AFL* [55], *pulmonary vein AFL* [56] and *left septal circuits AFL* [57].

3.1.3 Atrial fibrillation

The earliest concept of atrial fibrillation was proposed by Winterberg [58] in 1906 and Lewis, in 1912, who advocated that rapid focal activity from one or more centers accounted for AF. In the 1960s Moe [9] proposed the theory of randomly propagating multiple wavelets as the main mechanism underlying AF. A critical mass of atrial tissue is required to sustain the minimal number of simultaneous circuits necessary for arrhythmia perpetuation. In humans, approximatively six wavelets are required to sustain AF [59]. The wavelets in AF travel largely in a random fashion around islets of refractory atrial tissue. This hypothe-

sis has become widely accepted, particularly after the appearance of mapping studies by Allesie *et al.* [59].

Recently, Jalife and his colleagues [60] have questioned the randomness of atrial activity in AF. Their study suggests the presence of a possible *mother rotor*¹ that serves as a periodic background focus. The presence of anatomical obstacles such as scars and orifices lead to a break up of the wavefront from the mother rotor into multiple wavelets.

In 2002, Kneller *et al.* [61] proposed a two-dimensional computer model of cholinergic AF using a model of canine atrial tissue. Vagal actions were formulated based on patch-clamp studies of acetylcholine (ACh) effects. Their results suggest that heterogeneities in ACh concentration are sufficient to create fibrillatory conditions despite the complete loss of rate adaptation (*i.e.* restitution curve flattened) [62, 63].

3.2 Atrial flutter in the biophysical model

The selection of a membrane kinetics model is determined by the desired accuracy of the representation of the cell properties and by the available computer power. Since the atrial flutter is the most organized arrhythmia and does not involve several wavelets, it is not necessary to follow temporal evolution for a long period. The Courtemanche-Ramirez-Nattel membrane kinetics model, designed specifically to reproduce human atrial cell electrophysiology, is well adapted for this purpose.

3.2.1 Atrial flutter in the monolayer 3D model

In the present approach, it was decided not to include anisotropic fast-conducting regions, fiber orientation, crista terminalis (CT) and pectinate muscles (PM), to simplify the complexity of the model and retain a better control over the simulations. In spite of these limitations, an uncommon sustained atrial flutter could be simulated.

When using the unmodified CRN membrane kinetics model, the spatial wavelength λ is too long to sustain a flutter. The wavelength is longer than the circuit around the tricuspid valve leading the wavefront to collide with the wave tail and to collapse. The TV perimeter is 5.19 cm and the wavelength of the CRN baseline membrane kinetics model is 21 cm. The wavelength is the result of the product between the conductance velocity ($c = 70$ cm/s) and the action potential duration (APD = 300 ms).

In order to induce self-sustained AFL, the parameters of the membrane were modified to reasonably approximate APD restitution curve of remodeled human atria cells measured by Kim *et al.* [64]. Figure 3.2 presents the remodeled action potential shapes and restitution curves. Such changes (*remodeling*) in APD are often seen experimentally and clinically after many seconds of atrial arrhythmia. Remodelled cells were shown to be characterized by shorter APDs and reduce rate adaptation, *i.e.* flattened APD restitution.

¹A mother rotor is a stable source of reentry that generates multiple wavelet breaks

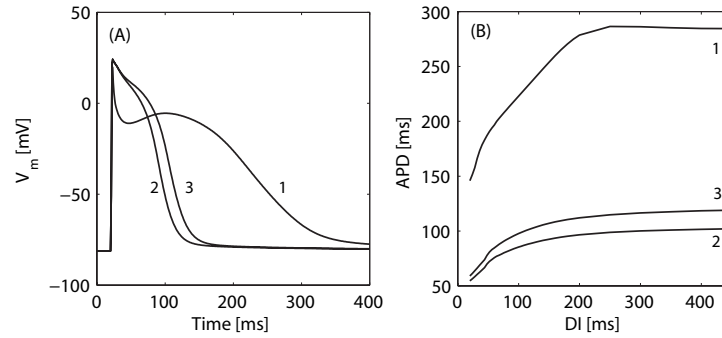


Figure 3.2 – Flutter on the monolayer model: action potential and restitution curve using the CRN membrane kinetics model. (A) Action potential. (B) Restitution curve. (1) Baseline model, (2) Remodeled with: I_{to} , $I_{Ca,L}$, I_{Kur} reduced to 20%, 70%, 10%, and I_{Kr} increased to 600%. (3) Remodeled with: I_{to} , $I_{Ca,L}$, I_{Kur} reduced to 20%, 70%, 10%, and I_{Kr} increased to 450%.

The simulations were conducted with a normal conductive tissue ($\rho \simeq 200 \Omega\text{cm}$, $c = 70 \text{ cm/s}$). The APD was reduced to 100 ms by modifying some currents (see table 2.3). The transient outward current (I_{to}), the calcium current ($I_{Ca,L}$) and the ultra rapid potassium (I_{Kur}) was reduced to 20%, 70% and 10%, respectively, and the time-independent potassium (I_{Kr}) was increased first to 600% (figure 3.2, curve (2)) and then reduced to 450% to obtain the appropriate restitution curve (figure 3.2, curve (3)). It was not possible to initiate the flutter directly by setting the I_{Kr} too 450%; the wavelength would be too long and the wavefront and wave tail would collide.

The flutter was artificially initiated by placing a block of conduction ($c = 0 \text{ cm/s}$) between TV and IVC. The conduction block was removed after 150 ms.

Figure 3.3 presents a transmembrane potential distribution map (TMPDM) during AFL initiation. A stimulus was applied in the isthmus region. Since there was the conduction block, the generated wavefront could only be propagated in the septum direction. The two wavefront extremities remained automatically anchored around TV and IVC. At 120 ms, the wavefront completed a cycle around the valve and vein, and was stopped by the conduction block. At 150 ms, the conduction block was removed and the wavefront could continue to propagate, but remained anchored around the valves. The time instant at which the conduction block is removed is critical. If it is removed too early, the wavefront may collide with the wave tail leading so to AFL termination. On the other hand, if it is removed too late, not enough current can propagate. By remodeling, not only the APD was shortened (figure 3.2(B)), but also the wavelength ($\lambda = c \cdot APD$), allowing a complete cycle to be obtained around TV. The wavelength should be shorter than the perimeter of the TV to ensure flutter. The cycle length was 150 ms (400 bpm), which corresponds to the rate of an AFL type II [47].

The steady-state was reached after one second. The wavefront extremity, which was anchored previously around the IVC during the initiation phase, was then anchored around the SVC. Figure 3.4 displays the TMPDM, the membrane potential and the unipolar elec-

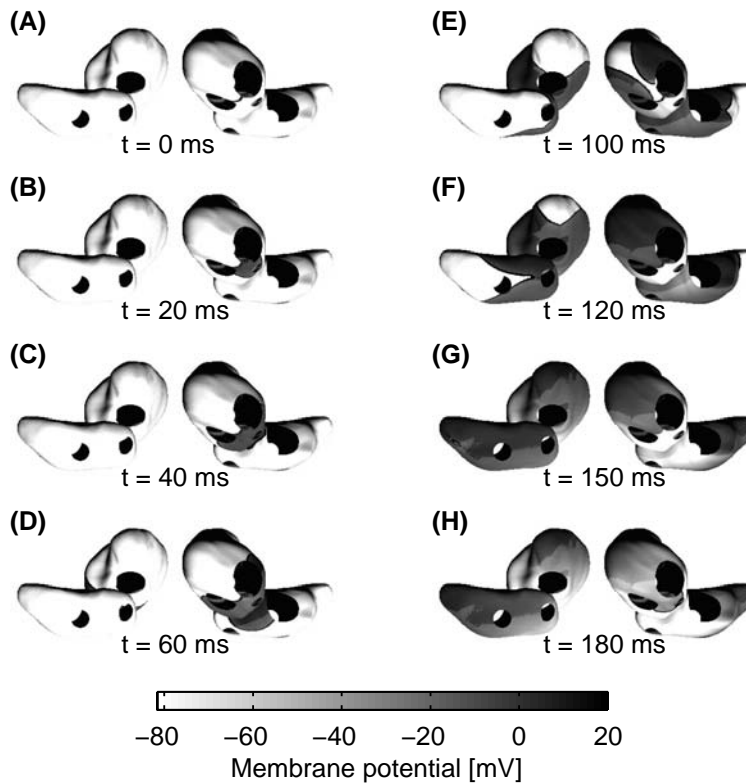


Figure 3.3 – Initiation of atrial flutter using the CRN membrane kinetics model. Superior and inferior view of the atria. TMPDM: (A) Stimulation with a conduction block between TV and IVC. (B) Propagation of the wavefront in the direction of the septum and blocked in the opposite direction due to the conduction block. (C-E) Propagation of the wavefront around valves/veins. (F) Wavefront has completed a cycle around TV. (G) The conduction block removed. (G) Perpetuation of the wavefront around TV and IVC.

rogram computed in the middle of the anterior right atrium, the percentage of excited tissue¹, and the number of wavelets after 4 s of simulated time. The steady state was subsequently achieved, the AFL remained stably anchored around TV and SVC (figure 3.4(A)). At 4.14 s the wavefront around SVC started to release from it (indicated by an arrow on figure 3.4(G-H)). This instability was due to the fact that the time taken for the wavefront extremity to cross the SVC perimeter was shorter than the CL. The wavefront extremity collapsed with its tail and was unable to stay stable around the SVC. The potential membrane and unipolar electrogram showed alternations between short and long potentials. The percentage of the excited tissue does not evolve regularly. Around 4.5 s, wave breaks appeared, as shown in figure 3.4(L).

Figure 3.5 displays the TMPDM after 4.6 s. The wavefront extremity previously anchored around the SVC was completely detached and evolved freely, as shown in figure 3.5(E-H) by the arrows.

¹The percentage of excited tissue is defined as the the percentage of nodes with an action potential above a fixed threshold (-60 mV)

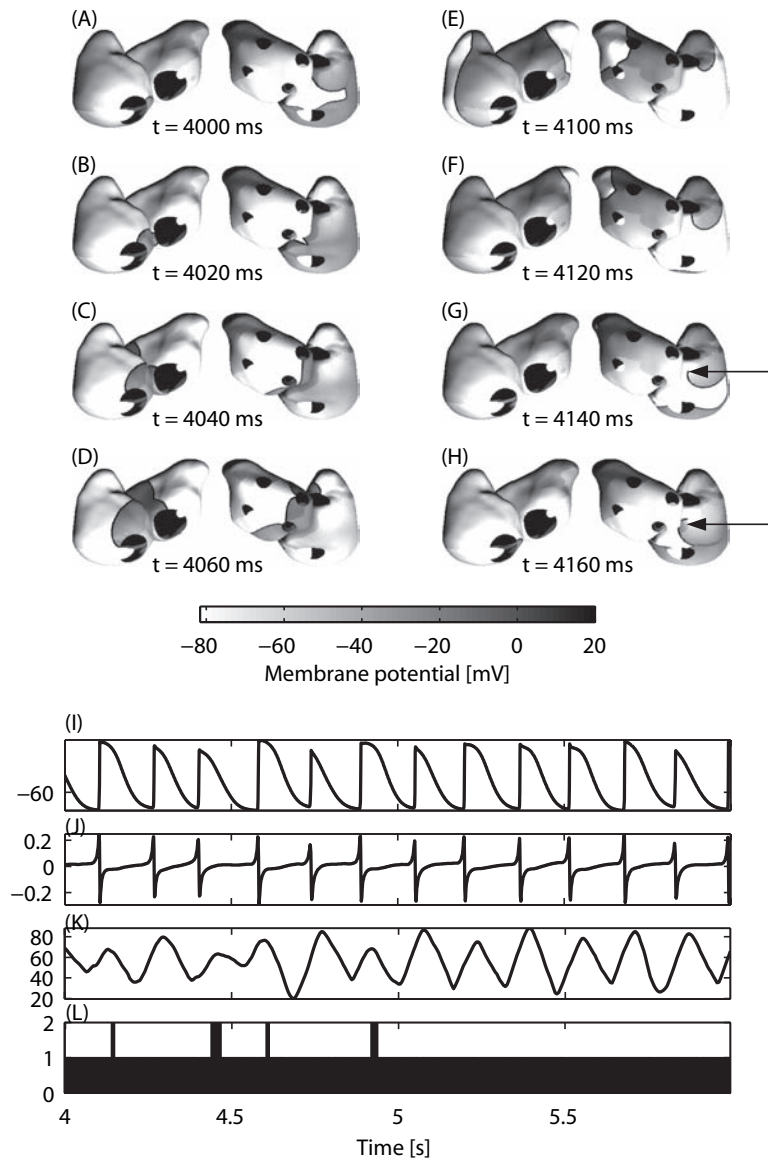


Figure 3.4 – Atrial flutter using the CRN membrane kinetics model (at 4 s). (A-F) TMPDM: Wavefront anchored around TV and SVC. (G-H) TMPDM: instability, wavefront leaving SVC. (I) Membrane potential computed in the middle of the anterior right atrium. (J) Unipolar electrogram computed in the middle of the anterior right atrium. (K) Percentage of excited tissue. (L) Number of wavelets.

The AFL presented in this section cannot be considered as an AFL type I in the strict sense. First, the flutter rate was twice as fast (400 bpm). Secondly, the flutter was unstable and did not have a constant circuit. It can be considered as an atypical right flutter or a CTI AFL, not previously reported in the literature.

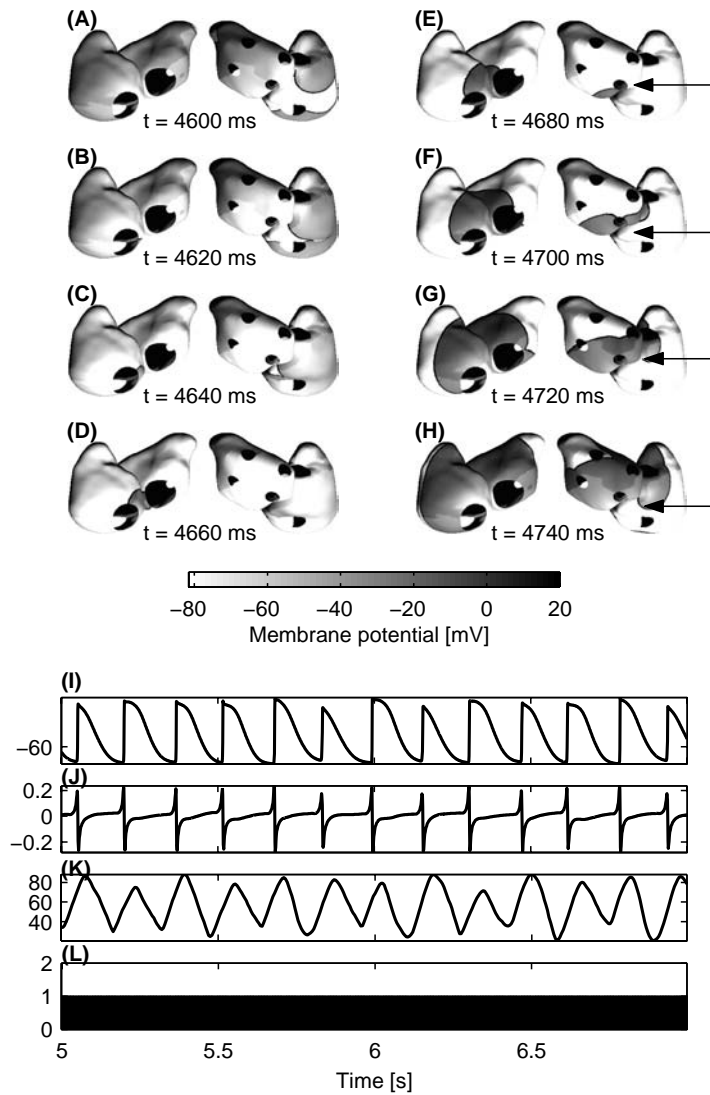


Figure 3.5 – Atrial Flutter using the Courtemanche model (at 5 s). (A)-(H) TMAPDM: One wavefront extremity is anchored to TV and the second one (indicated by an arrow) evolves freely. (I) Membrane potential computed in the middle of the anterior right atrium. (J) Unipolar electrogram computed in the middle of the anterior right atrium. (K) Percentage of excited tissue. (L) Number of wavelets.

3.2.2 Atrial flutter in the multilayer 3D model

Since the slow and fast conduction velocity boundaries plays a crucial role during AFL [46], in the present section, the 3D multilayer model is used to study atrial flutter. It includes anisotropic fast-conducting regions: the crista terminalis (CT), the pectinate muscles (PM) and the Bachmann's bundle (BB). Two slow regions was also considered: the isthmus region and the septum ring region. To obtain a sustained AFL, the APD was be reduced using the CRN membrane kinetics model, as in the previous section.

The simulation was conducted with a normal conductive tissue ($\rho \simeq 150 \Omega\text{cm}$, $c = 75 \text{ cm/s}$). Different conduction regions were considered: the crista terminalis ($\rho \simeq 80 \Omega\text{cm}$, $c = 115 \text{ cm/s}$), the pectinate muscle ($\rho \simeq 80 \Omega\text{cm}$, $c = 115 \text{ cm/s}$) the Bachmann's bundle ($\rho \simeq 50 \Omega\text{cm}$, $c = 135 \text{ cm/s}$), the isthmus region ($\rho \simeq 500 \Omega\text{cm}$, $c = 40 \text{ cm/s}$), the septum ring region ($\rho \simeq 800 \Omega\text{cm}$, $c = 10 \text{ cm/s}$) and the septum region ($\rho \simeq 500 \Omega\text{cm}$, $c = 40 \text{ cm/s}$) [65–68].

The APD was reduced to 150 ms with a transient outward current ($I_{\text{Ca,L}}$), the calcium current ($I_{\text{Ca,L}}$) and the ultra rapid potassium (I_{Kur}) reduced to 20%, 50% and 10%, respectively. The time-independent potassium (I_{Kr}) was increased first to 600% and then reduced to 250%, compared to 450% in the monolayer 3D model. Since a slow conduction region was added, it was possible to increase the APD duration slightly. The isthmus region allowed the macro-reentrant to slow down around TV and avoided the wavefront colliding with its tail. The membrane kinetics was not modified in the CT. The initiation protocol involved a line of conduction block as in the previous experiment.

Figure 3.6 represents schematically the AFL pathway in the presence of anisotropic fast-conduction regions. First, the wavefront coming from the isthmus region crosses the CT, which depolarizes (figure 3.6(A-B)). Second, due to the difference of action potential durations in the CT and the tissue, the CT creates a line of functional block (figure 3.6(C-E)). The action potential duration along the CT is much longer than in the tissue. So, when a wavefront has performed a cycle around the IVC, it cannot go through the CT, because it is still in the refractory period. Finally, the CT arrives in a resting state and the wavefront can cross and depolarized it (figure 3.6(F)).

Figure 3.7 presents the TMPDM of the AFL in the 3D biophysical model. With the APD modification on the CT and the functional block, the CL was increased to 180 ms (333 bmp). The depolarization of the CT is shown in figure 3.7(A-B). Consequently the CT was blocked, and the wavefront propagated along the CT (figure 3.7(C-G)). Finally the CT was repolarized and a new wavefront could cross it (figure 3.7(H)).

Despite the addition of major fast conduction structures and a slow conduction region, this flutter cannot be considered as a typical flutter, because during the cycle, the functional block is not always persistent. According to the literature, the CT should be always blocked and no transverse conduction are possible during AFL [65–67]. This flutter looks more like a LLR flutter, involving a reentrant circuit around the IVC and a superior circuit around the SVC.

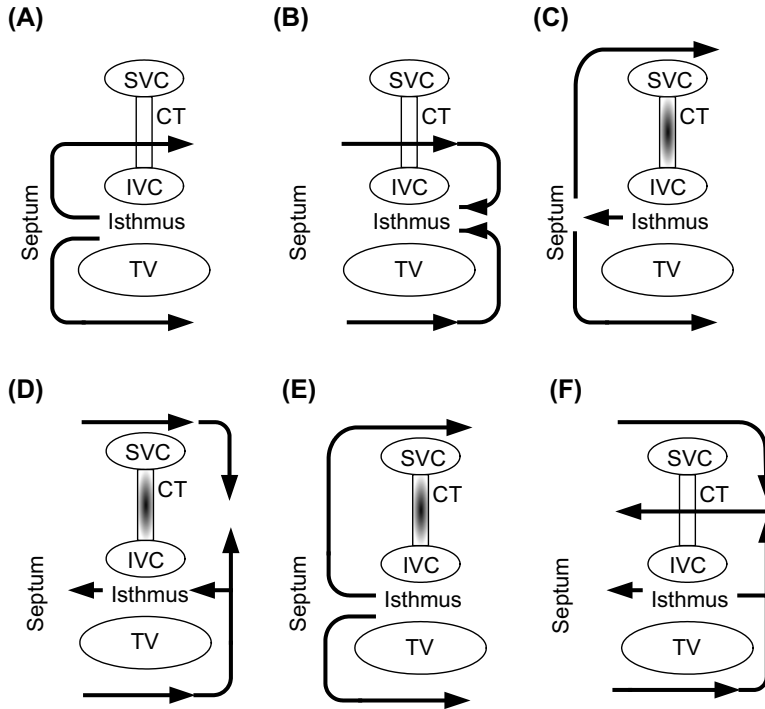


Figure 3.6 – Atrial flutter pathway using the 3D model. The pathway is indicated by arrows. (A)-(B) Wave is anchored to TV and IVC and the wavefront crosses the CT. (C)-(E) CT functional block due to the long action potential duration. (F) The CT is repolarized and the wavefront can cross it.

To remedy to this situation, the APD needs to be readjusted as shown in figure 3.8. In the tissue, the currents $I_{Ca,L}$ and I_{Kr} were reduced to 10% and in the CT, besides the two previous currents, the current I_{to} , was reduced to 50%. The APD curve was completely flattened.

The induction of the flutter was initiated as done previously and furthermore the CT was blocked momentarily (by setting the conductivity to zero). After initiation, the classical circuit was established, the CT was unblocked and the AFL type I was maintained for several cycles. After a while, the same mechanism as described in figure 3.6 became visible. The instability of the flutter around the CT may be explained by the fact that in the present biophysical model, the conductivity of the CT is homogenous. In reality, myocardial fibers packed in parallel along the SVC and IVC exhibit rapid conduction in a longitudinal direction, but very slowly in a transverse direction, with a ratio of 10:1 [69]. This remarkable difference in conduction velocity is due to a high resistivity of side-to-side cell coupling [70], related to a preferential distribution of gap junctions in end-to-end locations [71].

An alternative to creating a constant AFL type I, was to maintain the conductivity of the CT region at zero and to initiate an AFL as previously described. The AFL obtained followed a pathway such as that described in the literature. But this is unrealistic, because

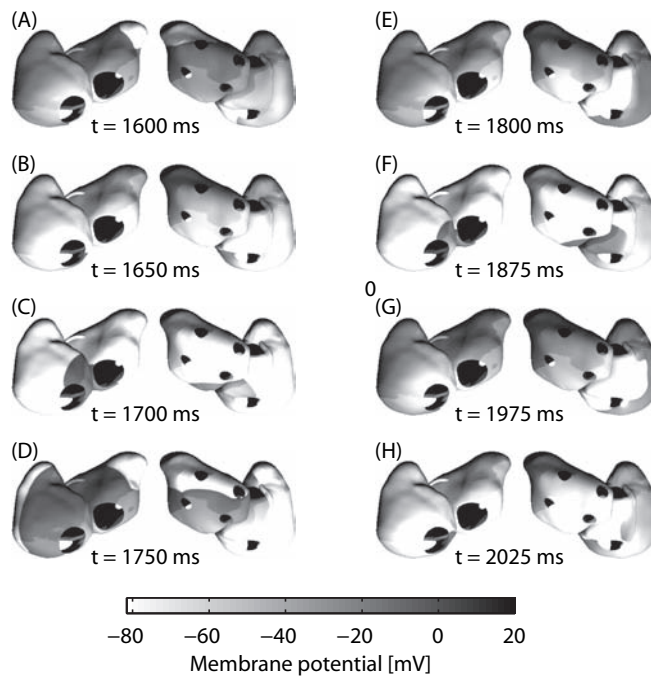


Figure 3.7 – Atrial flutter using the 3D model: TMPDM. (A) Depolarization of the CT. (B) Repolarization of the CT and tissue. (C)-(G) Functional block of the CT. (H) CT is excitable.

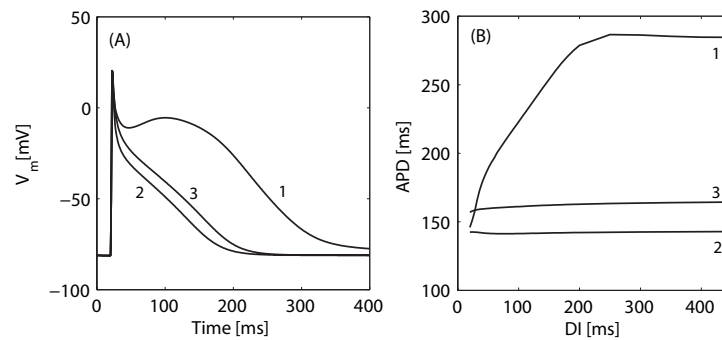


Figure 3.8 – Flutter on the multilayer 3D model: action potential and restitution curve using the CRN membrane kinetics model. (A) Action potential. (B) Restitution curve. (1) Baseline model. (2) Remodeled with $I_{Ca,L}$ and I_{Kr} reduced to 10% in the tissue (3) Remodeled with $I_{Ca,L}$ and I_{Kr} reduced to 10% and I_{to} reduced to 50% in the CT.

CT would not recover its conductivity after *cardioversion*¹ or during sinus rhythm.

¹Cardioversion refers to the process of restoring the heart's normal rhythm by applying a controlled electric shock.

3.3 Atrial fibrillation in the biophysical model

In the following sections, various type of AF, which can be reproduced in the biophysical model are briefly reviewed (see more details in [5]). Three different mechanisms of AF have been reproduced with the model: chronic AF, meandering AF and cholinergic AF. It has been decided not to consider firing focus activity maintaining AF[72], which would have required the design of a subset of the atrial tissue in order to achieve adequate automaticity, or a rapid pacing of this region this region.

3.3.1 Initiation of atrial fibrillation

Initiation of atrial fibrillation was performed by means of an injection of intracellular current ($I_{\text{stim}} = 80 \mu\text{A}/\text{cm}^2$) in a small region of $\sim 3 \text{ mm}^2$ during 2 ms. Several clinical protocols are possible [73, 74]:

- programme stimulation protocol ($S_1 - S_2 - S_3$): three sites are selected and each stimulus S_i is delivered at each site with a different timing;
- burst pacing protocol: periodic pacing of 20-50 Hz;
- ramp protocol: incremental pacing, until AF is detected.

In the biophysical computer model, in most of the cases, a burst pacing protocol is preferable, because it does not need time adjustment between stimuli, which is a time consuming task.

3.3.2 Perpetuation of atrial fibrillation

Initiation of AF is not the only requirement of a biophysical model of human atria. It should be able to produce a number of wavefronts and wavelets that are self-sustaining. The first source of instability and induction of wavelet breakup is a steep restitution curve [5, 28, 75, 76]. While spontaneous wave breaks are associated with an increase in the slope of the restitution, AF is usually associated with a loss of rate adaptation and in general a flattening of the restitution dependence.

The second mechanism that can also lead to AF perpetuation is the inclusion of structural heterogeneities and gradients in APD. Kneller *et al.* [61] have recently developed a two-dimensional membrane kinetics model of cholinergic AF. Their results suggest that heterogeneities in acetylcholine concentration are sufficient to create fibrillatory conditions despite the complete loss of rate adaptation.

These mechanisms maintaining sustained AF (SAF) are used to simulate the different types of AF in the following sections.

3.3.3 Chronic atrial fibrillation

The first type of AF that can be generated by the biophysical model uses the coarse surface mesh (50,000 nodes, with a spatial resolution of $\Delta x = 0.6$ mm). A finer mesh (100,000 nodes, $\Delta x = 0.4$ mm) was used to check the accuracy and to ensure the absence of artifacts. The membrane kinetics model used was the LRI model. This model was originally developed to represent the electrical activity of ventricles.

The choice of the model was motivated by both the desire to reduce computation load and the simplicity of the model, which involves only six internal currents. To approximate the specific electrical properties of atrial cells, action potential duration (APD) was adapted by adjusting channel conductances G_{Na} to 16 mS/cm², G_K to 0.423 mS/cm² and G_{Si} to 0.085 mS/cm², corresponding to the membrane current I_{Na} , I_K and I_{Si} , respectively (see table 2.2). This setting corresponds to the baseline model (figure 3.9, curve (1)) with a maximum slope of the restitution curve greater than 1, which allows the initiation of AF [28, 77, 78]. After initiation, APD restitution plays a key role in maintaining sustained AF. The restitution curve should be flattened, therefore conductance channel G_{Si} was set to 0.055 mS/cm² (figure 3.9, curve (3)) with a maximum slope of the restitution curve being smaller than 1, which allows the maintenance of a sustained AF [5].

Figure 3.10 illustrates the TMPDM during SAF. The main characteristic of this model is very a short action potential duration (mean CL $\simeq 75$ ms); the percentage of excited tissue ranges between 40% and 60% and the number of wavelets varies between 1 and 11. Based on the latest information, it is shown that the number of wavelets does not indicate whatever AF will self terminate or not. An abrupt change appears in the percentage of excited tissue and number of wavelets (figure 3.10(L)). Thus, a single isolated wavelet may generate or maintain a sustained AF. Conversely, multiple wavelets may block or lead to annihilation of each other.

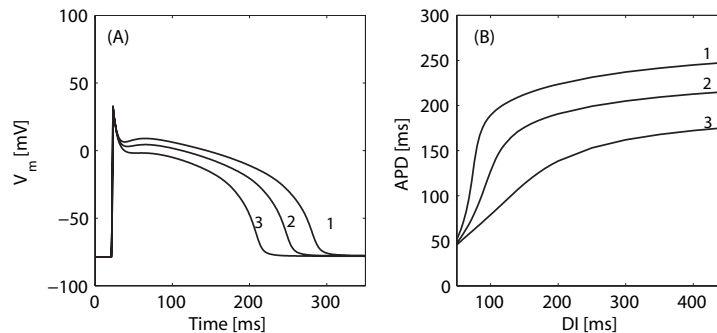


Figure 3.9 – *Chronic atrial fibrillation: action potential and restitution curve. (A) Membrane potential. (B) Restitution curve. (1) Baseline model $G_{Si} = 0.085$ mS/cm². (2) Remodeled with $G_{Si} = 0.070$ mS/cm², (3) Remodeled with $G_{Si} = 0.055$ mS/cm²*

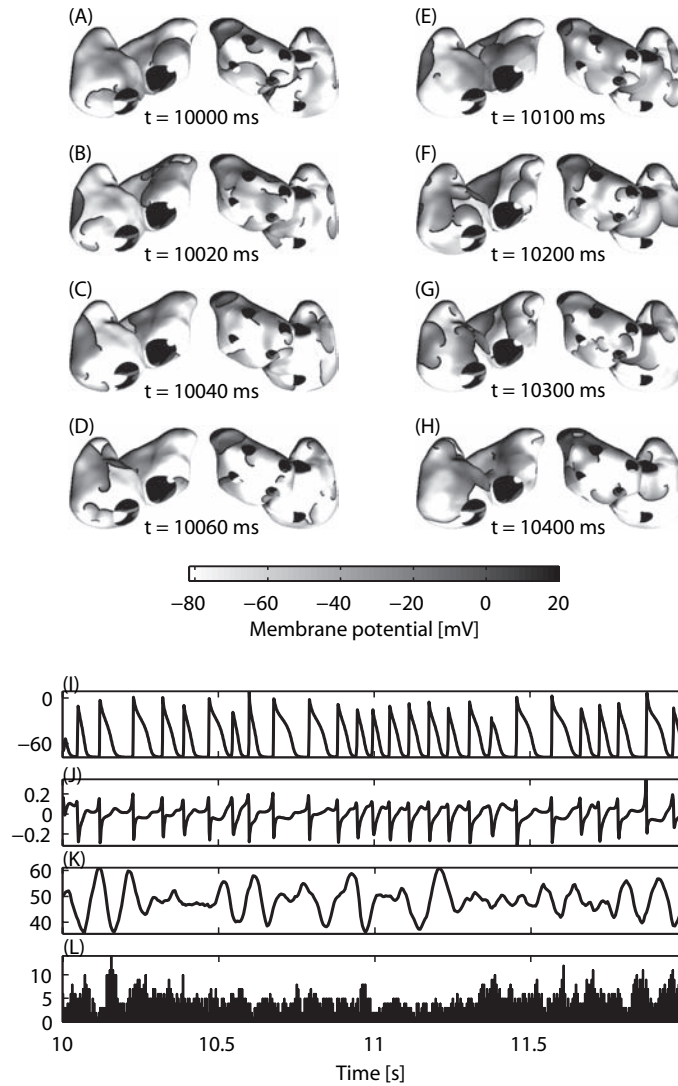


Figure 3.10 – Chronic AF in isotropic tissue using the LRI membrane kinetics model. (A)-(H): TMPDM during SAF. (I) Membrane potential computed in the middle of the anterior right atrium. (J) Unipolar electrogram computed in the middle of the anterior right atrium. (K) Percentage of excited tissue. (L) Number of wavelets.

3.3.4 Meandering atrial fibrillation

The second type of AF was reproduced using the CRN membrane kinetics model. This model was designed to reproduce more realistically the human atrial cell electrophysiology. The action potential duration is much longer than the LRI. SAF occurred only for a few seconds [5], when it was initiated. In order to maintain SAF, the restitution curve should be modified (figure 3.11, curve (2)) as proposed by Courtemanche *et al.* The currents I_{to} , I_{CaL} and I_{Kur} , were reduced by 80%, 30% and 90%, and I_{Kr} increased by 50%.

Figure 3.12 presents the TMPDM. Contrary to the previous model, this one presents a lower rate and beat-to-beat interval as shown in figure 3.12(I,J). Note also the effect of alternance between a short and a long action potential. The percentage of excited tissue could reach 80% mainly due to the long APD ranging from 150 to 200 ms (figure 3.11(B), curve (2)). The reduced complexity in this simulated AF can be observed in the number of wavelets that ranges between 1 and 3.

3.3.5 Cholinergic atrial fibrillation

Several animal experiments used isolated atria with acetylcholine addition to initiate AF [79, 80]. Kneller *et al.* have recently developed a two-dimensional computer model of cholinergic AF using canine atrial tissue [61]. This model based on the Courtemanche model, includes additionally an acetylcholine-driven potassium current $I_{K(ACh)}$ to the list of membrane currents (table 2.3). The parameter associated with this current allowing it to modify the APD is $g_{K(ACh)}$ [5]. The resulting action potential has a triangular shape (figure 3.11(A), curves (3,4)) and the restitution curve is almost constant (figure 3.11(B), curves (3,4)).

The presence of heterogeneities presumes to be an arrhythmogenic factor [81–83]. The inclusion of some random heterogeneity patch size, in the range of 1.5 mm to 2.5 mm, facilitates a fibrillatory condition [5]. The ERP was set to 95 ms in the heterogeneity

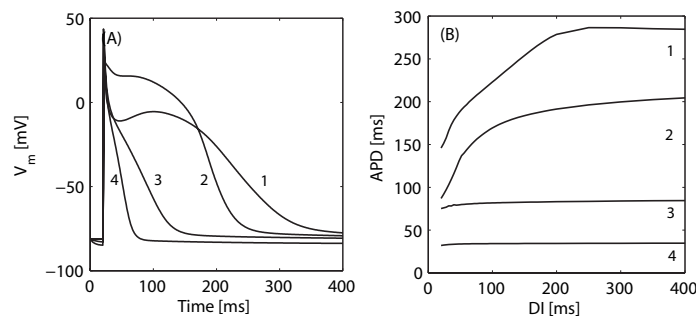


Figure 3.11 – Atrial fibrillation restitution curve using the CRN membrane kinetics model. (A) Action potentials. (B) Restitution curves. (1) Baseline model. (2) Remodeled for the meandering AF. (3) Remodeled for the cholinergic AF with acetylcholine-driven potassium current $g_{K(ACh)} = 7 \text{ ms}^{-1}$. (4) Remodeled for the cholinergic AF with acetylcholine-driven potassium current $g_{K(ACh)} = 25 \text{ ms}^{-1}$.

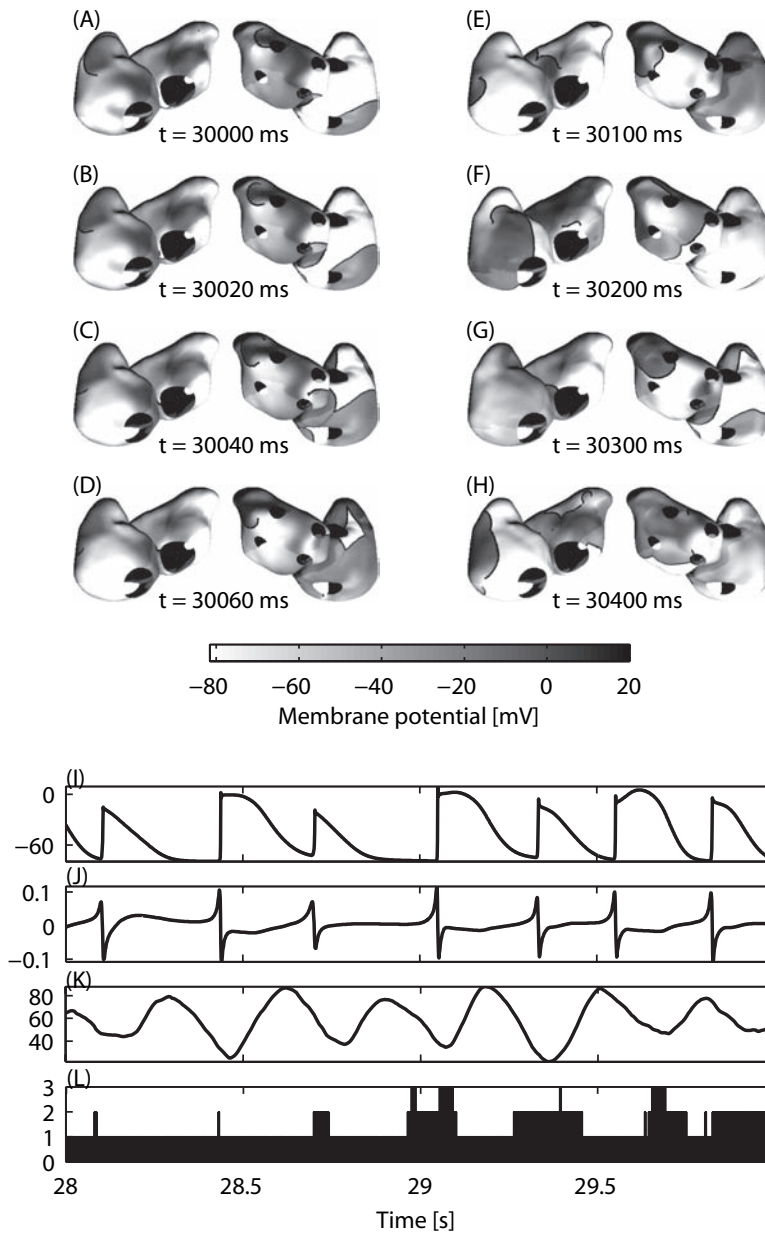


Figure 3.12 – Meandering AF in isotropic tissue using the Courtemanche model. (A)-(H): TMPDM. (I) Membrane potential computed in the middle of the anterior right atrium. (J) Unipolar electrogram computed in the middle of the anterior right atrium. (K) Percentage of excited tissue. (L) Number of wavelets.

region (dark region, in figure 3.13(A)-(H)) and 45 ms elsewhere.

Figure 3.13 displays the TMPDM of a cholinergic SAF, which was maintained thanks to the heterogeneities. Those served as a stable source of wavelets reentries (mother rotor) as indicated by an arrow on the left atrium appendage (figure 3.13(A)). The membrane potential and the electrogram signal revealed a beat-to-beat interval around 90 ms (11 Hz), comparable to that of the chronic AF model (section 3.3.3). This similarity is also

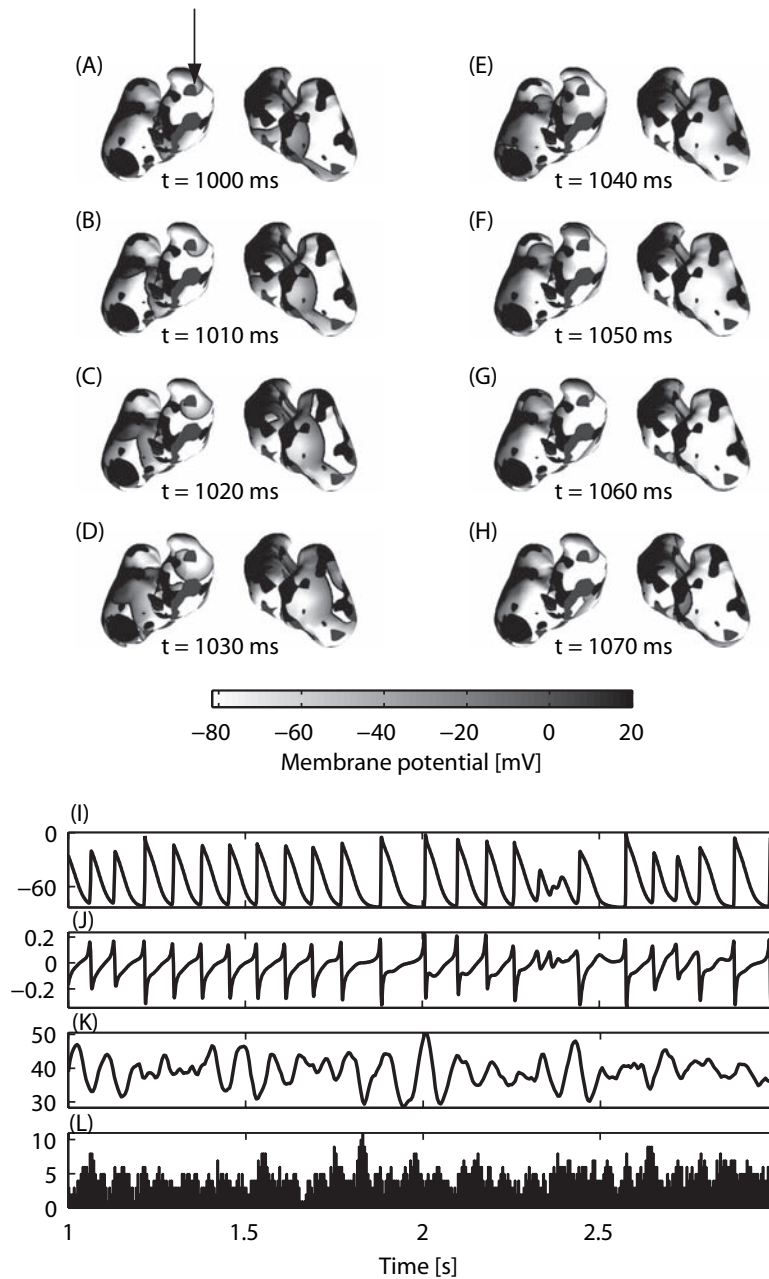


Figure 3.13 – Cholinergic AF in isotropic tissue using the Courtemanche model. (A)-(H): TMPDM. (I) Membrane potential computed in the middle of the anterior right atrium. (J) Unipolar electrogram computed in the middle of the anterior right atrium. (K) Percentage of excited tissue. (L) Number of wavelets.

confirmed by the percentage of excited tissue ($\approx 50\%$) and the number of wavelets (≈ 5). Note that around 2.4 s oscillation in the electrogram signal was observable (figure 3.13(J)), induced by discontinuities between the tissue and heterogeneities [84].

3.4 Conclusions

In this chapter several types of arrhythmia simulated with the biophysical model have been presented.

First, a low complex arrhythmia involving only one macro-reentrant circuit was exposed. It was initiated on the monolayer and multilayer 3D model. Second, more complex arrhythmias characterized by several wavelets and fast rhythm were reviewed. Among these, there was some unrealistic arrhythmia which utilized acetylcholine to initiate and maintain AF, which could only be found in animal experiments.

These different types of arrhythmia (atrial flutter, chronic AF, meandering AF and cholinergic AF) are used in the remainder of the dissertation to measure the spatio-temporal organization and to investigate atrial therapies.

Part II

Measures of organization

This second part describes several methods to measure and quantify the spatio-temporal organization during atrial fibrillation (AF). Its first chapter (chapter 4) presents spatio-temporal measures of organization as derived from the analysis of the electrogram signals. Classical signal processing methods are used to evaluate AF complexity. The second chapter (chapter 5) is focused on AF activities at the cellular level. The mechanisms responsible for AF perpetuation are analyzed.

Spatio-temporal organization

4

4.1 Introduction

DURING atrial fibrillation (AF) several wavebreaks and reentries are involved, leading to an irregular atrial activity. When studying the electrophysiology of AF, the main interests are: the investigation of wavefront propagation, as well as the mechanisms responsible for reentry and perpetuation of the arrhythmia; the assessment of the electrophysiological properties of the cardiac substrate from the perspective of optimizing atrial therapies. Several intra and extra-atrial mapping techniques such as electrogram mapping, basket catheters or high-resolution video imaging have been used to study the complexity of the AF dynamics [85–89].

In the 1980s, Allessie *et al.* [59] mapped the cardiac electrical activity during AF and provided the first experimental evidence supporting Moes multiple wavelets hypothesis [9, 90]. According to this hypothesis, during AF several wavefronts of electrical activity propagate randomly throughout the surface of both atria, forming complex and ever-changing patterns of electrical activity. Konings and colleagues [89], by using a high density epicardial mapping system, described the activation pattern during AF in the free wall of the right atrium. Several authors have suggested, but never proved, that there is a strict correlation between organization and number of wavelets entering the atrial region close to the recording electrodes [9, 90, 91]. It has been speculated that the likelihood of termination to a normal rhythm is inversely related to the number of propagating wavelets.

The early methods were mainly based on measurements extracted from atrial rate and, to a minor extent. Since there is no standard definition of organization, various approaches have been adopted to collect AF recordings and several signal processing algorithms have

been developed to quantitatively assess the spatial and temporal organization of AF. Those latter approaches can be put into three different groups: time-domain, frequency domain and non-linear dynamics approaches [85]. These methods can be applied to a single signal or to a set of signals measured at several positions.

One of the main advantages of a biophysical model is the possibility provided to access each action potential computed at each node of the meshed surface. Using this information once can: (1) evaluate and track the spatio-temporal evolution of the propagation, (2) capture an endocardial electrogram at any location. These electrogram signal recordings are used to compare with those obtained by electrophysiologists in experimental and clinical studies.

In the first part of this chapter, a high density mapping system is used to estimate the local organization during AF. In the second part, the entire atrium is considered. This approach is used to investigate the number of regions or electrodes necessary to quantify AF complexity. Then measures of complexity are defined, two of them based on principal component analysis, in order to determine the number of electrodes needed on the surface of the atria to access the dynamics of AF. Next, these measures are applied to monitor the spatio-temporal evolution for different situations: sinoatrial rhythm, chronic AF, meandering AF and cholinergic AF. In a later chapter (chapter 7), these methods are used to measure AF complexity during atrial pacing as well.

4.2 Measures of organization

4.2.1 State of the art

Although most of the research dealing with automated processing and analysis of intracardiac signals has been devoted to methods and schemes for recognition and classification of cardiac arrhythmias in implementable devices, interest has recently grown for developing methods aimed at electrophysiological investigations.

Several different indices of signal complexity have been developed and applied to biomedical signals, and in particular to electrocardiograms or electrogram signals. These methods have been applied to a single signal or to a set of recorded signals. The table 4.1 summarizes the main current methods used for the analysis of AF from intra-atrial signals. These methods are grouped as time-domain, frequency domain and non-linear dynamics approaches.

The main attempts to interpret the signal processing indexes in terms of electrophysiological properties or mechanisms use the concepts of organization, synchronization and complexity. Unfortunately standard definitions of these terms in the context of the phenomenon of AF do not exist and none of the various methods proposed in the literature have yet demonstrated themselves to be useful for the identification of regions sustaining AF [85].

Besides these methods, other signal processing approaches such as pattern matching,

Time domain	
Botteron (1995) [86]	Cross-correlation, space constant calculation.
Jais (1996) [92]	Complex electrical activity and FF interval.
Sih (1999) [91]	Adaptive transfer function estimation.
Barbaro (2000) [93]	Comparison of time domain and frequency domain.
Censi (2000) [87]	Recurrence plot analysis.
Frequency domain	
Sahakian (1992) [94]	Magnitude-squared coherence spectra.
Lovett (1997) [95]	Coherence spectrogram.
Jalife (1998) [96]	Spectral estimation.
Complex dynamics theory-based	
Hoekstra (1995) [97]	Correlation dimension and correlation entropy.
Pitschner (1998) [98]	Fractal dimension.
Berkowitsch (2000) [99]	Algorithmic complexity.

Table 4.1 – *Main methods to analyze atrial fibrillation.*

wavelet-based methods, archetypal analysis, etc. are currently being investigated.

4.2.2 Local high density mapping

To study local organization during AF two standard methods are used in experimental setups: optical mapping [100] and electrical mapping [89]. Optical mapping enables the visualization of the wavelets dynamics. The cardiac tissue is stained with fluorescent voltage-sensitive dye. By illumination, variations of membrane potential are recorded by a high-speed CCD video camera. Electrical mapping focuses on the depolarization and repolarization process. A set of electrodes are applied directly onto the epicardium or endocardium and the electrical potential is recorded.

In the present study, a simulated electrical mapping system, developed by Jacquemet [5], was used to emulate unipolar electrode recordings (section 2.3.3) in a manner similar to that used by Konings [89] in experimental studies. The mapping system consists of an array of 16 by 16 electrodes placed at 1 mm from the tissue on the right anterior atrial free wall (figure 4.1). The distance between electrode pairs is 2.25 mm, and the mapped surface is approximatively 11.4 cm².

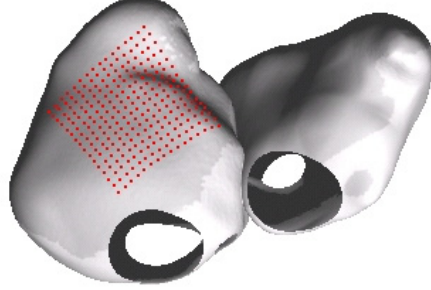


Figure 4.1 – *Local high density mapping. The electrodes positions (16 x 16) are indicated by dots and located at 1 mm from the tissue.*

4.2.3 Global mapping

Since the atrial geometry is meshed with triangular meshes of different spatial resolutions (50'000 or 100'000 nodes), it is not conceivable to consider the entire information resulting from each node. To reduce the complexity of the analysis, the atria are split into regions of equal area and electrodes are placed in the center of each region to record electrical activity. The number of regions is defined as:

$$\text{Number of regions} = 2^{\text{Split level}} \quad (4.1)$$

In this way, each atrium is split into $2^{\text{Split level}-1}$ regions (figure 4.2). An iterative procedure is used to split the tissue. Each iteration is designed to split an arbitrarily shaped surface into two regions of equal area. It is based on the momentum of inertia (2^{nd} order) taken at the center of gravity of the surface. The momentum of inertia I of the initial tissue patch is computed as:

$$I = \int_V \rho(x, y, z) \begin{bmatrix} y^2 + z^2 & -xy & xz \\ -xy & x^2 + z^2 & -yz \\ xz & -yz & x^2 + y^2 \end{bmatrix} dx dy dz, \quad (4.2)$$

where ρ is the density, V the volume and x, y and z are coordinates relative to the center of gravity of the tissue patch. Under the assumption of a constant monolayer thickness, ρ is equal to 1 on the surface and 0 elsewhere. The three principal axes of the tissue are found by computing the eigenvectors of the tensor. The plane that is orthogonal to the first principal axis of inertia, and contains the center of gravity, is described by $ax + by + cz$ with a, b, c corresponding to the coordinates of the center of gravity. Finally, the plane parallel to the plane containing the center of gravity is selected. It separates the initial surface into two regions of equal area (*i.e.* equal number of nodes).

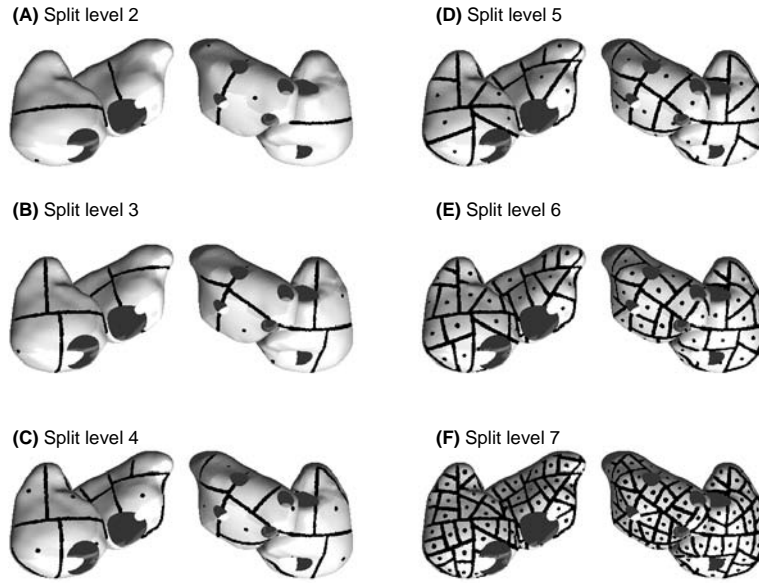


Figure 4.2 – Global high density mapping with respect to split level. (A)-(F) Split level 2-7. The center of gravity of each region where position of electrodes are place are marked by a dot.

4.2.4 Multidimensional signal analysis

To study local organization, multidimensional *bipolar* electrogram signals computed on the surface of the high density mapping system are considered. A bipolar electrode is modeled as the difference in electric potential between two points close to each other, *i.e.* difference between two unipolar electrode signals. Thus a set of 8 by 8 bipolar electrogram signals are obtained. The correlation space-constant method (see next section), proposed by Botteron *et al.* [86], are applied on the signals.

To access global organization, two sets of multidimensional signals are considered on the split atrial model. The first set is that of the unipolar electrogram signals computed at the center of each region, 1 mm from the surface. The second set of multidimensional signals uses these same signals, to which the first three processing steps described in the next section are applied. The electrogram signal sampling frequency is 1 kHz. Two different signal processing methods, principal component analysis and entropy, (see next section) are associated with these signals to evaluate the complexity.

Correlation space-constant

Botteron *et al.* [86] proposed a measure of organization based on the maximum cross-correlation between two pairs of signals. The procedure is composed of the following steps applied on N digital signals $x_i(t)$, each one representing a bipolar electrogram recorded by two electrodes located at \mathbf{d}_i and sampled at 1 kHz:

- filter the signals with a third-order, zero-phase Butterworth band-pass filter with

cutoff frequency at 40 and 250 Hz;

- fake the absolute value of the filtered signals;
- filter the signals with a third-order, zero-phase Butterworth low-pass filter with a cutoff frequency at 20 Hz;
- remove signal mean values and normalize. The resulting filtered signal is called y_i ;
- correlation coefficients: for each pair of signals y_i and y_j :
 - compute the Euclidean distance $d_{i,j} = \|\mathbf{d}_i - \mathbf{d}_j\|$;
 - compute the cross-correlation $c_{i,j}(\tau)$ between y_i and y_j ;
 - the correlation coefficient $C_{i,j}$ is defined as the maximal cross-correlation $C_{i,j} = \max_{\tau}(c_{i,j}(\tau))$;
- plot a graphical representation: (1) group together the points with the same distance $d_{i,j}$, (2) plot the pairs $(d_{i,j}, C_{i,j})$ and display instead the mean and standard deviation;
- fit the function $C(d) = e^{-d/\delta}$ to the data to determine the space constant δ .

An interesting property of this method is that the resulting space constant δ gives an approximation of the average wavelength λ through the simple formula $\lambda = 2\pi \cdot \delta$ (see Botteron [86] and Jacquemet [5] for more details).

Principal component analysis and entropy

Principal component analysis (PCA) [101] (also called Karhunen-Love transform) involves a mathematical procedure that transforms a number of (possibly) correlated variables into a (smaller) number of uncorrelated variables called *principal components*. The first principal component accounts for as much of the variability in the data as possible, and each succeeding component accounts for as much of the remaining variability as possible. The objective of PCA is to discover or to reduce the dimensionality of the data set and to identify new meaningful underlying variables. The aim is to find a set of M orthogonal vectors in data space that account for as much as possible of the data's variance. Projecting the data from their original N -dimensional space onto the M -dimensional subspace spanned by these vectors then performs a dimensionality reduction that often retains most of the intrinsic information in the data. This technique is used in various fields such as signal processing, biology and economy.

Let $x_r(t)$ be the unipolar electrogram computed in the middle of the region r at time t . Let $\mathbf{X}(t) = [x_1(t), \dots, x_N(t)]^T$, where N is the number of regions. In a stationary situation, the estimation of the sample covariance matrix ($\mathbf{C}_\mathbf{X}$) of $\mathbf{X}(t)$ provides an efficient and simple way to characterize how the vectors $x_r(t)$ are spatially related to each other. From a symmetric matrix such as the covariance matrix, an orthogonal basis can be calculated

by finding its eigenvalues and eigenvectors. The principal components are then given as: $\mathbf{M}_{\text{PC}} = \mathbf{M}_{\text{E}} \cdot \mathbf{X}(t)$, where \mathbf{M}_{PC} and \mathbf{M}_{E} denote the matrix with the principal component and eigenvectors, respectively.

The total energy captured in a principal component analysis decomposition of a numerical or experimental data set is defined as the sum of all eigenvalues (μ):

$$E = \sum_{k=1}^N \mu_k, \quad (4.3)$$

where μ_k is the k^{th} eigenvalue of C_X sorted in decreasing order. The relative energy captured by the k^{th} mode (or principal component), E_k is defined by:

$$E_k = \frac{\mu_k}{\sum_{j=1}^N \mu_j}. \quad (4.4)$$

A first measure of complexity used is ($CEig_{95\%}$), is defined by:

$$CEig_{95\%} = \min \left\{ k \left| \sum_{i=1}^k E_k \geq 0.95 \right. \right\}. \quad (4.5)$$

$CEig_{95\%}$ may be seen as an “effective” dimension, *i.e.* the dimension of the hyperplane the vectors are mostly confined to. By neglecting the latest eigenvalues, 95% of the total energy is conserved by the projection on the principal components.

The second measure, which is reminiscent of Shannon’s entropy [102], consists of computing a pseudo-entropy of the same eigenvalues:

$$CEnt = - \sum_{l=1}^N \left(\frac{\mu_l}{\sum_{k=1}^N \mu_k} \log \frac{\mu_l}{\sum_{k=1}^N \mu_k} \right). \quad (4.6)$$

$CEnt$ quantifies the flatness of the eigenvalue distribution. This measure is continuous, whereas $CEig_{95\%}$ is discrete. The entropy, as defined by (4.6), measures the energy distribution among the modes in the principal component spectra. The entropy is low when the energy is concentrated in a few modes. A zero entropy indicates that only one eigenfunction, with maximal energy, is needed to reproduce the dynamics. The entropy increases when the energy spreads across a large number of modes, indicating complex behavior [103].

To study the time evolution of the complexity, the above measures are derived from data within moving time windows of one second with an overlap of 0.5 s.

The two following sections present results on the measures of organization for several types of simulated AF. First, spatial organization is measured locally and globally. Then temporal evolution of this organization is analyzed.

4.3 Spatial organization

4.3.1 Local high density mapping

Figure 4.3 presents results using the correlation space-constant method on the high density mapping system. Four different cases were analyzed: (1) sinoatrial rhythm, (2) chronic AF, (3) meandering AF and (4) cholinergic AF. Electrogram signals were computed in a 8 by 8 grid of bipolar electrodes located in the right atrium free wall. During sinoatrial rhythm, the correlation coefficient was close to 1 and remained constant for all distances (1-4 cm). During chronic AF, the correlation was significantly smaller due to the multiple wavelet reentries. The space constants of activation δ measured during chronic and meandering AF were found to be respectively 1.27 ± 0.24 cm and 1.66 ± 0.24 compared to 1.84 ± 0.36 measured in humans [104]. The exponential curve for the meandering AF was close to that of chronic AF, although the action potential of the latter was significantly shorter. During cholinergic AF, the space constant was approximately 3.70 ± 0.70 cm, which was higher than during chronic or meandering AF. This was at first unexpected, since the addition of heterogeneities should increase wave breaks and reentries. But by analyzing the transmembrane potential distribution map (TMPDM) of figure 3.13, it was found that a mother wavelet anchored on the left atrium appendage was present. This wavelet generated a periodic wavefront starting from the left atrium and passing through the right atrium, occasionally producing wavebreaks due to heterogeneities. These induced at first the generation of AF by breaking the wavefront into multiple wavelets due to a difference of action potential duration in the tissue. However, heterogeneities favored wavelet anchoring and generated a stable mother rotor, sweeping other wavelets off.

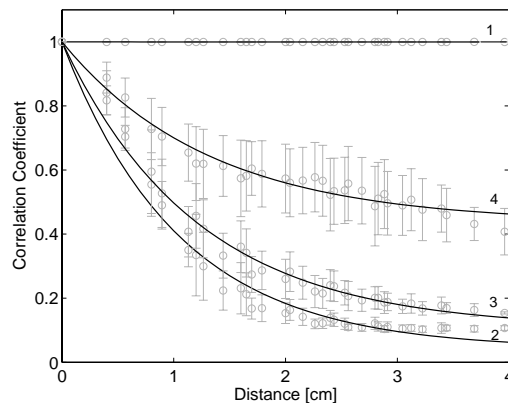


Figure 4.3 – *Spatial correlation at the anterior right atrium. 1 Sinoatrial rhythm. 2 Chronic AF. 3 Meandering AF. 4 Cholinergic AF. Means and standard deviations are respectively denoted by circles and bars.*

4.3.2 Global density mapping

The complexity for the sinoatrial rhythm and for different types of AF in terms of the number of eigenvalues used to achieve 95% of the energy $CEig_{95\%}$ and the entropy $CEnt$ were plotted as a function of the split level for unfiltered signals and filtered signals in figure 4.4 and in figure 4.5, respectively. The curves presented are the average complexity derived from 10 measurements of one second each.

The complexity increased with the number of regions even for a normal sinoatrial rhythm, and saturated rapidly above split level three for unfiltered electrogram signals, as well as for the filtered electrogram signals (figure 4.4, curve (1) and figure 4.5, curve (1)).

In the case of atrial fibrillation, $CEig_{95\%}$ and $CEnt$ increased with split level and reached a plateau for split level six for the filtered electrogram signals (figure 4.5, curves

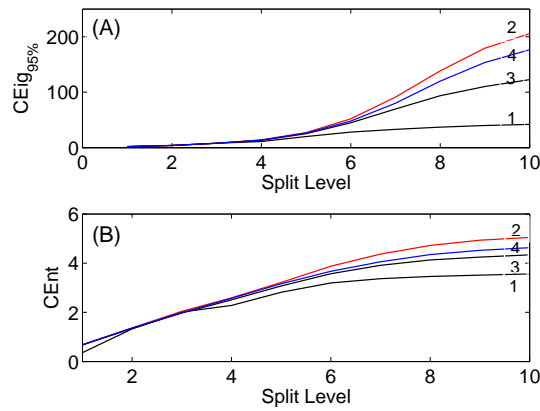


Figure 4.4 – Measure of complexity as a function of the split level using unfiltered electrogram signals. (A) $CEig_{95\%}$. (B) $CEnt$. 1 Sinoatrial rhythm. 2 Chronic AF. 3 Meandering AF. 4 Cholinergic AF.

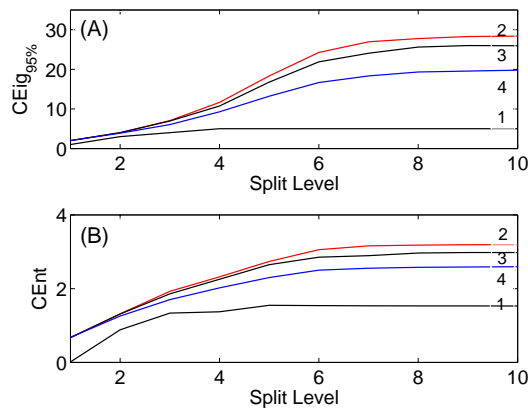


Figure 4.5 – Measure of complexity as a function of the split level using filtered electrogram signals. (A) $CEig_{95\%}$. (B) $CEnt$. 1 Sinoatrial rhythm. 2 Chronic AF. 3 Meandering AF. 4 Cholinergic AF.

(2-4)). Split level six corresponds to 32 regions per atrium. The area of a tissue patch at this split level is 1.3 cm^2 and the distance between electrodes, placed in the center of each neighborhood patch, is approximately 1.2 cm. Since there is not additional information above split level six, this value was used to study temporal complexity evolution in the next section.

4.4 Temporal organization

Figure 4.6 shows the temporal evolution of complexity for different types of AF, using the filtered electrogram signals. A split level of six was used and a moving time window of one second, with an overlap of 0.5 s, was used to estimate the covariance matrix (\mathbf{C}_X) on the multidimensional signals. Four cases were studied: (1) sinoatrial rhythm, (2) chronic AF, (3) meandering AF, and (4) cholinergic AF.

For the sinoatrial rhythm and the chronic AF, the measurements remained very stable over time (figure 4.6, curves (1-2)). Meandering AF (figure 4.6, curve (3)) showed a larger variation, in particularly between 0 and 5 s. After that, the complexity $CEig_{95\%}$ and $CEnt$ were comparable but remained on average lower than to that of chronic AF. During cholinergic AF (figure 4.6, curve (4)), the largest variations were visible. The complexity $CEig_{95\%}$ decreased to 10 and $CEnt$ to 2 between 10 and 15 s. This instant corresponds to a mother rotor anchored around an heterogeneity, which maintained a single principal wavefront and a few wavelets. But between 0-5 s and after 18 s, the values of the complexity measure were higher, meaning that several wavelets were present and that a mother rotor was either not present or less effective. This was confirmed by observing the transmembrane potential distribution map during the simulation.

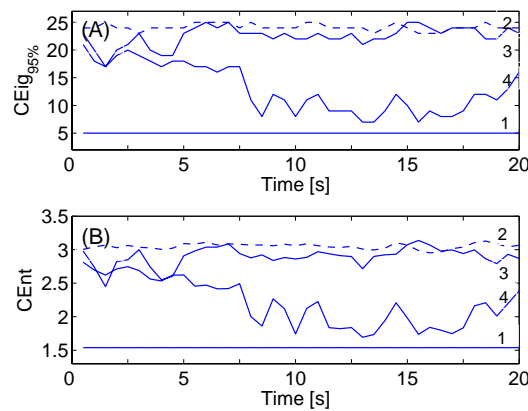


Figure 4.6 – Measure of complexity over time using filtered electrogram signals. (A) $CEig_{95\%}$. (B) $CEnt$. 1 Sinoatrial rhythm. 2 Chronic AF. 3 Meandering AF. 4 Cholinergic AF.

4.5 Conclusions

In this chapter, measures of spatio-temporal organization during sinoatrial rhythm and different types of AF were investigated. High density mapping and a geometrical splitting of the atrial geometry were shown to be efficient ways of investigation local and global activity during AF. To simplify the number of electrogram signals needed to quantify AF organization, a geometrical splitting of the atria was used in order to find an optimum decomposition.

Three signal processing methods were presented to study the complexity of atrial activity, two of them based on principal component analysis. Results show that using a split level six corresponding to 32 regions per atrium was sufficient to capture AF complexity. The corresponding region area is 1.3 cm^2 and the distances between electrode localization is 1.2 cm.

These measures were applied to different cases: sinoatrial rhythm, chronic AF, meandering AF and cholinergic AF, and several atrial activities were differentiated. By observing the local and global activities, chronic AF and meandering AF exhibited less organized activity during AF. However, cholinergic AF manifested higher organization during AF, when there was a mother rotor nearby.

The methods presented will be used in the chapter 7 to quantify AF organization during atrial electrical stimulation.

Tracking of phase singularities

5

5.1 Introduction

As is now well known, atrial fibrillation (AF) is a common form of cardiac arrhythmia, characterized by rapid and irregular atrial activity. Current hypotheses about AFs suggest that they are caused by: a rapid cell discharge, atrial foci, single reentry circuits, or multiple functional reentrant circuits [105]. Regardless of the causes initiating AF, it is always associated with the presence of rotating waves of electrical excitation. The centers, or cores of these waves generate and maintain AF.

The application of electrical mapping and optical mapping methods to obtain high-resolution recordings of electrical activities promises to improve considerably the understanding of AF mechanisms. When a wavebreak occurs through the interaction of the wavefront with anatomical or functional obstacles, a phase singularity (PS) appears (figure 5.3), whereby electrical waves may rotate uninterruptedly and, in a self-sustaining manner, give rise to high frequency electrical activity that propagates throughout the tissue [106–109]. The concept of PS has contributed substantially to the current understanding of mechanisms of spontaneous initiation and maintenance of reentrant arrhythmia.

The wave of excitation rotating around a PS for one or more cycles is defined as a *rotor*. The identification of these PSs is essential in order to be able to analyze the mechanisms underlying AF in experimental or mathematical models. Understanding the mechanisms of PS formation, and determining its location and lifespan can be important in the development of effective therapies. Effectively, by isolating PSs using surgical ablations (chapter 6) or by sweeping PSs off using electrical stimulations (chapter 7), it could be possible to cardiovert AF into sinoatrial rhythm.

In the 1990s, Jalife [110] provided evidence of PS being present in an isolated Langendoff-perfused rabbit heart using a voltage-sensitive dye [111]. Since then, several biophysical models have been developed to understand the mechanisms underlying PS formation. Until now, PS localization and tracking have been studied on cell grids of varying sizes or on biophysical ventricular models [77, 79, 106, 112–115].

However, neither the experiments nor current state-of-the-art models have been able to examine the myocardial tissue during AF on human atria and neither they can identify phase singularities at the core of the reentrant pathways.

This chapter presents a new approach to PS localization and tracking based on a realistic atrial geometry meshed with triangular elements. This method is applied to several types of AF (see chapter 3) which can be generated by the biophysical model and PS behavior is observed in each type.

5.2 Phase singularity detection

5.2.1 Cardiac phase

The phase $\theta(\vec{r}, t)$ is a cardiac variable which uniquely defines the state of a cell at any time t and location \vec{r} [107]. In the past, phase was most often defined as the fraction of time elapsed following the last activation or event [116]. However, during atrial fibrillation all sites do not undergo “full-blown” action potential. This makes the definition of the *activation time*¹ difficult. Therefore, Iyer *et al.* [117] proposed a definition of phase that is independent of the activation time. According to this definition, two variables are needed to uniquely calculate the phase. However, in practice, only one variable (the transmembrane potential V_m) is typically recorded. The required two variables, namely $V_m(\vec{r}, t)$ and $V_m(\vec{r}, t + \tau)$, can be obtained from the single recorded signal $V_m(\vec{r}, t)$ by means of a delay embedding technique [118].

The delayed embedding technique uses two variables obtained from the transmembrane potential measured at the same site but with a time delay τ . The measurement at every site generates a so-called reconstructed state space that is topologically equivalent to the true state space [119]. Figure 5.1 illustrates schematically these two variables and the phase $\theta(\vec{r}, t)$.

The three tags A, B and C in figure 5.1 illustrate the relation between an action potential and its return map. The tag A represents the phases (0) and (1) described in chapter 2. They correspond to a rapid change in the transmembrane potential V_m with respect to time. Thereby for a fixed value of τ , a small variation of $V_m(t)$ may imply a large variation of $V_m(t + \tau)$. Conversely, during the plateau tagged as B, $V_m(t)$ remains relatively constant. Therefore the slope of the corresponding segment of the return map is small. The repolarization, tag C, is represented approximatively by a decreasing linear segment. This

¹The activation time for a given position is defined as the time instant at which the membrane cell depolarizes.

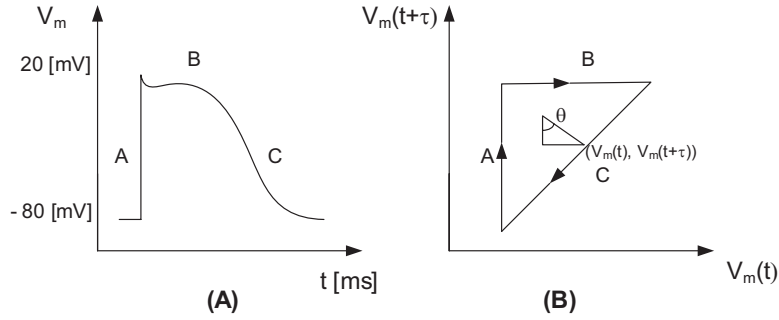


Figure 5.1 – Illustration of the meaning of the phase variable. (A) Transmembrane potential. (B) Return map ($V_m(t + \tau)$ vs. $V_m(t)$) of this action potential for a phase value θ .

representation may vary depending on the time delay τ such as illustrated in figure 5.2. If τ is a very small value and tends to zero, the return map tends to be a linear curve with a slope of 1. Conversely, if τ is set to a too large value, the depolarization phase is not detected in the phase map (figure 5.2(D), $\tau = 200$ ms).

The mathematical expression of the phase variable is given by (5.1) and is illustrated in figure 5.1(B):

$$\theta(\vec{r}, t) = \arctan \left(\frac{V_m(\vec{r}, t + \tau) - V^*(\vec{r})}{V_m(\vec{r}, t) - V^*(\vec{r})} \right). \quad (5.1)$$

Here $V^*(\vec{r})$ is the potential at the chosen origin of the phase space and $\vec{r} = (x, y, z)$ represents the coordinates of the analyzed site. The resulting phase has a value between

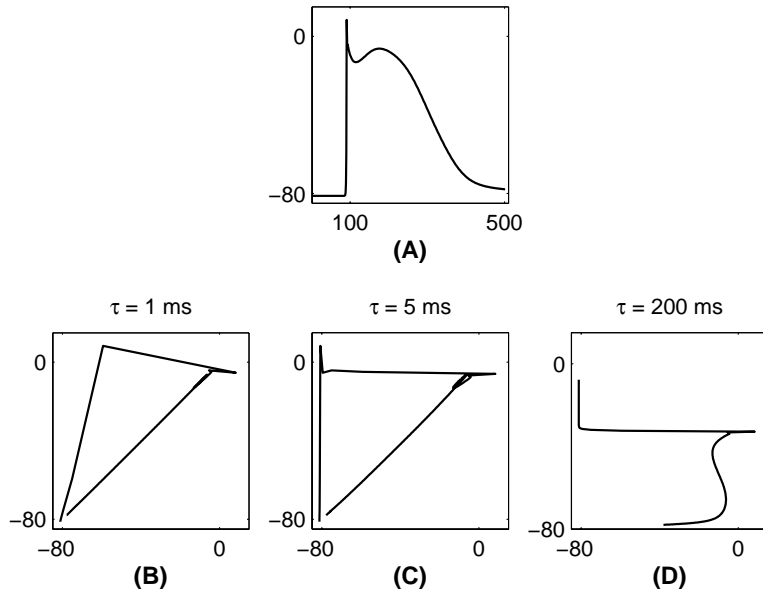


Figure 5.2 – Phase space in function of different time delay τ . (A) Transmembrane potential. (B)-(D) Phase space with $\tau = 1, 5, 200$ ms, respectively.

$-\pi$ and π . Any point in the state space around which the closed loop trajectory shown in figure 5.1(B) revolves exactly once, is an admissible origin point for computing the phase [117]. In this study, two different points were tested as possible origins:

- the spatial average point, *i.e.* the mean value of $V_m(\vec{r}, t)$ over all recorded sites (*i.e.* at each node of the meshed surface) at time t ;
- the temporal average point, *i.e.* the mean value of $V_m(\vec{r}, t)$ over all time records at site \vec{r} .

The two phase maps resulting from using both of these two origins were very similar. Only a slight shift of one node on the mesh was sometimes observed. This shift corresponds to a maximum distance difference in the range of 200 to 400 μm depending on the spatial discretized geometry used (50 000 nodes or 100 000 nodes). Since the computation of the spatial average point is less computationally expensive, it was set as the default origin for the localization algorithm developed.

A phase map shows the instantaneous value of the phase $\theta(\vec{r}, t)$ for all cells situated at a site $\vec{r} = (x, y, z)$ at a particular instant t . Figure 5.3 shows an action potential map and its corresponding phase map. The tip of the spiral is visually more explicit and intuitive in the phase map than in the action potential map. This visual effect results from two causes:

- the output value range is smaller for the phase map than for the action potential map. Indeed, the phase has mainly three distinct values corresponding to the three possible states shown in figure 5.3(B). Thereby the differences are clearer;
- the transmembrane potential V_m is not a unique measure of the state of the heart. Indeed, during an action potential, a value of say -30 mV is reached twice: once during the depolarization and once during the repolarization.

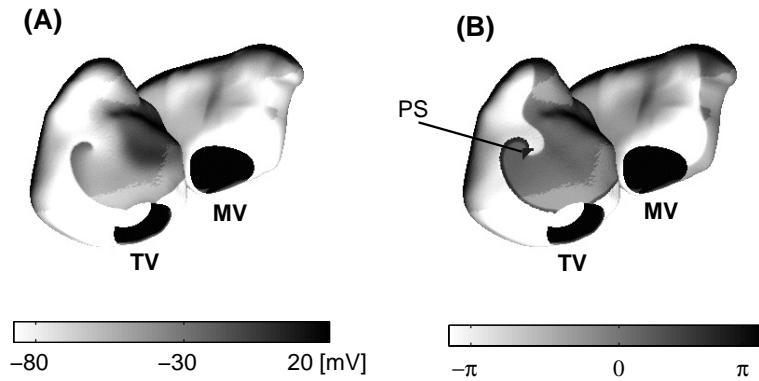


Figure 5.3 – (A) Transmembrane potential distribution map. (B) Its corresponding phase map. The localization of the PS is indicated by an arrow.

5.2.2 Phase singularity

A unique spatial pattern exists near the tip of the rotating wave: the phase at the exact center is undefined whereas neighboring sites exhibit a continuous progression of the converging phase value. This center is commonly named the phase singularity. Specifically, a PS is present where the line integral of the gradient of the phase around a site equals $\pm 2\pi$ [117]. The sign indicates the direction in which the associated wavefront circulates around the singularity with respect to the close path of the integral. The mathematical definition of a PS is:

$$\vec{r} \left| \oint \nabla \theta d\vec{l} = \pm 2\pi \right. \quad (5.2)$$

5.3 Localizing of phase singularities

At first sight, any path used for the integration to detect a PS is conceivable, on condition that the path is closed. Since the biophysical model is meshed with triangular elements, the path along the side of the triangle is considered. The length of the discretized closed path varies according to the situation:

- in the general case, the discretized closed path is the path along three nodes constituting a triangular mesh. Such a mesh is the smallest element defining the monolayer structure of the biophysical atrial model. The main advantages are the detection of all potential PSs and the avoidance of implementing an algorithm to define a path;
- if a wavelet extremity is anchored around a macroscopic anatomical obstacle, the discretized path encloses all the nodes constituting the contour of the vein orifice or valve ring.

These two cases are discussed in the following sections.

5.3.1 Phase singularities in the general case

Generally, the PSs are located in the conductive tissue of the atria. The location of a potential PS is within the triangular mesh whose corners have three different possible phase values, as depicted in figure 5.1. In other terms, the sum of the three phase differences obtained at each segment of this triangular element must be equal to the value of $\pm 2\pi$ (see (5.3)). The phase differences can be associated with a vector linking two adjacent nodes. Indeed, this value is related to a direction and a location.

Automatic PS localization is performed using (5.2). The continuous closed integral is changed into a discretized sum of phase difference values expressed in (5.3). Since the sum is made over a closed path computing N nodes, the phase θ_{i+1} computed for the last node corresponds to the first element of the discrete sum as illustrated in figure 5.4. Phase values

θ_i are computed using (5.1). The time delay τ is set to 5 ms for the whole process, as this value is sufficient to detect the membrane depolarization. Prior being used in (5.3), each computed phase difference $\Delta\theta_i$ is rescaled in the $[-\pi, +\pi]$ interval according to (5.4).

$$\sum_{i=1}^N \psi(\Delta\theta_i) = \sum_{i=1}^N \psi(\theta_{i+1} - \theta_i) = \pm 2\pi \quad (5.3)$$

$$\text{with } \theta_{N+1} = \theta_1 \text{ and } \psi(\theta) = \begin{cases} \theta + 2\pi, & \text{if } \theta < -\pi \\ \theta - 2\pi, & \text{if } \theta \geq \pi \\ \theta, & \text{otherwise} \end{cases} \quad (5.4)$$

The three nodes forming a triangular mesh are always accessed in a counterclockwise order as illustrated in figure 5.4. This ordering corresponds to that of the biophysical model viewed from the epicardium surface. Thus, the sign of the discrete sum in (5.3), which indicates the *chirality*¹ is consistent for the whole set of meshes.

5.3.2 Phase singularities anchored around a macroscopic anatomical obstacle

Through simulation it has been noticed that sometimes one wavelet extremity gets anatomically anchored around a vein orifice, a valve ring, or the fossa ovalis. The PS of this wavelet is close to the center of the macroscopic anatomical obstacle. However, these anatomical barriers are holes and are therefore not defined by meshes. The potential singularities cannot be detected by the standard case method presented above.

Instead of summing over a triangular mesh, the sum over all the nodes defining the contour of a particular vein orifice or valve ring is computed.

In order to be consistent with the discretized sum over a triangular element, the sum has to be computed over a closed path traversed in a counterclockwise direction. Since the contour of macroscopic anatomical obstacles is set by nodes randomly stored, the contour nodes have to be first sorted into an appropriate order.

¹The chirality associated with a PS corresponds to the direction in which its wavefront circulates around the singularity.

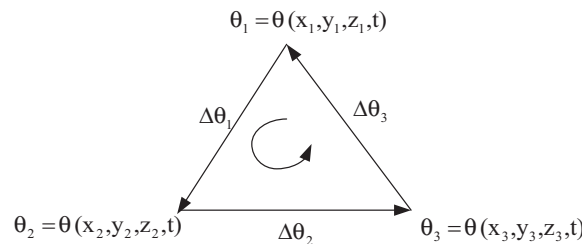


Figure 5.4 – Phase variable on a triangular mesh.

The direction of rotation around the vein orifice or valve ring is defined by the sign of the scalar product between the vectors $\vec{n}_{\text{triangle}}$ and \vec{n}_{cross} . The sign is positive/negative if the direction is clockwise/counterclockwise. The vector $\vec{n}_{\text{triangle}}$ is the processed normal of a triangle touching the vein orifice or valve ring. The vector \vec{n}_{cross} is the cross product between the vectors \vec{v}_1 and \vec{v}_2 defined by three points at the macroscopic anatomical obstacle as shown in figure 5.5. In this figure the direction of \vec{v}_1 or \vec{v}_2 has to be changed in order to make their cross product point in the counterclockwise direction.

Several singularities can be anatomically anchored at the same time around a macroscopic anatomical obstacle, this applies especially for the large mitral and tricuspid valve (TV) rings. The number of anchored singularities is determined by the result of the discretized sum in (5.3). Indeed, the quotient of the division by 2π indicates how many PSs are temporally attached to it. Yet, pairs of singularities with opposite chirality, which are both anchored at the macroscopic level, are filtered out. This case can be considered as a unique wave whose wavefront is split into two because of the obstacle. Figure 5.3(B) shows such a case since only one wavefront crosses the TV.

In order to easily store the position of a PS (formed by three nodes) in the case of a wavelet extremity anchored around a vein orifice or a valvular ring, among three nodes forming the PS, the one on the orifice is selected. The wavefront is defined by the phase maximum. It is easier to track the tip of the wavelet when it leaves the obstacle.

The procedure to detect the contour nodes at the wavefront is as follows:

1. a suitably chosen threshold is applied to the phase map (the nodes at the macroscopic anatomical obstacle that are larger than the threshold form non-touching subsets as depicted in figure 5.6(1-4));
2. the maximum phase value of every subset is stored as a PS.

This process is launched only if the absolute value of the discrete sum described in (5.3) is only larger than 2π .

When the process is used, false PS detection may occur due to the fact that this procedure is unable to differentiate between a wavelet anchored around an orifice by one of its extremities and a unique wavelet temporally splits into two because of a macroscopic anatomical obstacle. Figure 5.6 illustrates such situation: PSs (1) and (4) are true PSs,

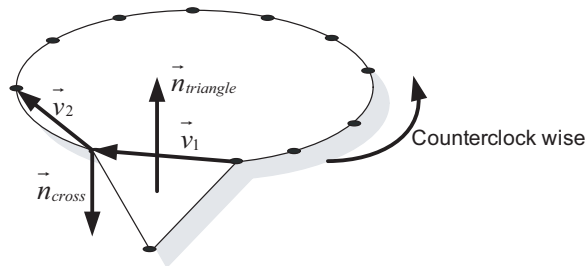


Figure 5.5 – Determination of the rotation direction at veins/valves using the sign of a scalar product.

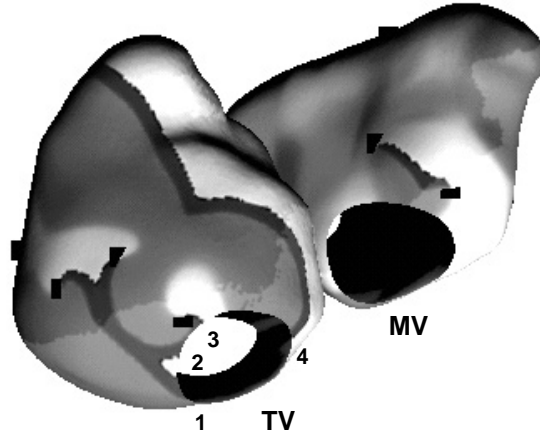


Figure 5.6 – *Illustration of true and false phase singularities detected when several singularities are anchored around a macroscopic anatomical obstacle. (PSs are numbered).*

conversely, PSs (2) and (3) constitute false PS detections. The latter are discarded by the tracking algorithm. The discrimination method is presented in section 5.4.

5.4 Tracking of phase singularities

In addition to localizing the PSs, we are also interested in automatically tracking them over a certain period of time.

The tracking method consists of finding the best association for each pair of successive phase maps so as to generate trajectories. The best association criterion allows the algorithm to successfully connect two successive representations of the same phase singularity computed for t and $t + \tau$. This criterion relies on two parameters: the minimal distance and the sign of the discrete sum.

The minimal distance between two consecutive representations of the same PS is the main parameter. Indeed, most of the time, the displacement of PSs between two successive phase maps is small. This distance is computed between the gravity centers of every triangular element enclosing a PS. In the case of wavelets anchored around a vein orifice or a valve ring, the distance is computed from the coordinates of the single node considered as a potential PS.

The sign of the discrete sum (5.3) is a advantageous parameter in the cases where several PSs detected are close. It helps the tracking algorithm to connect the correct pairs since the sign of the PS remains unchanged. As mentioned in section 5.2.2, the sign indicates the direction of rotation at the wavelet tip with respect to the counterclockwise direction of the closed path.

The tracking method was made more robust against incorrect connections by adding the following three constraints:

- a limited search area;
- an exclusion of PSs already assigned;
- a constraint on the creation of new trajectories starting at a vein orifice or valve ring.

These three criteria are discussed in the following sections.

5.4.1 Limited search area

The search for the minimal distance is only processed within a search circle centered on the PS to be connected. Such a limitation is needed for example, to solve the case in which a PS “dies” due to a collision with a wavefront or an anatomical obstacle at time t but is however wrongly linked to a relatively close one at time $t + \tau$.

Zou *et al.* suggested a radius of 5 mm in [115]. In this study, a radius of 7.63 mm was chosen in accordance with the following experiment. First, the PSs detected on the Luo-Rudy I (LRI) membrane kinetics model, which shows the highest wavelet reentrant, without any distance limitation, are associated by the algorithm. Then a manual check was performed to determine the maximal distance beyond which the link proved to be incorrect.

Large distances between PSs can occur in the case of wavelet collisions, when spirals became anchored to a vein orifice or valve ring, or in the case of PS jumps. The leap is due to repolarization wavebacks. This phenomenon is illustrated in figure 5.7 on the right of the PS indicated by an arrow. Because the cells constituting this refractory front cannot momentarily be stimulated, a part of the activation wavefront (on the right side) stops while the other part, not located in this refractory area, continues to move. Thus the PS appears to jump.

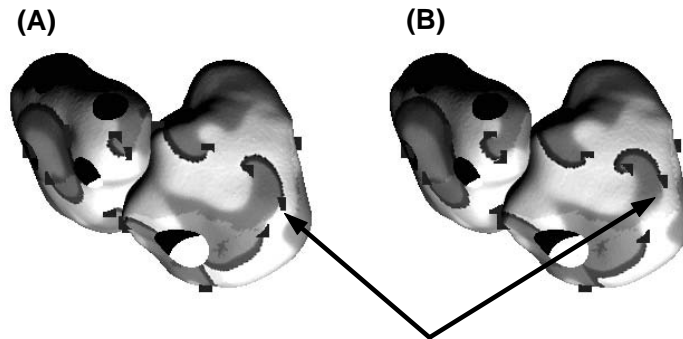


Figure 5.7 – Illustration of a jumping phase singularity (indicated by an arrow) due to the to a refractory front. (A) Phase map at instant t . (B) Phase map at instant $t + \tau$

5.4.2 Exclusion of PSs already assigned

This constraint is especially needed when a PS vanishes. It prevents the linking of a PS detected at time t , with a PS detected at time $t + \tau$ if the latter has already been assigned to another, much closer, PS. The expression “much closer” is mathematically expressed by an arbitrarily chosen distance.

Figure 5.8 demonstrates the utility of the constraint on already assigned PSs. The algorithm allows a “fusion” between PSs (1) and (2) (figure 5.8(A)), since they are approximately at the same distance, figure 5.8(B). Nevertheless, the constraint avoids the merging of PS (3) with PS (1+2) between figure 5.8(B) and (C). Indeed PS (1+2) has to die out: the collision between two wavelets propagating in the same direction generates a junction of the two wavefronts.

5.4.3 Constraint on the creation of new trajectories starting at vein orifice or valve ring

As explained in section 5.3, the PS localization procedure may detect false PSs. The false positive detections are at the intersection points of a unique wavelet split in two, due to macroscopic anatomical obstacles. This error is common in the largest anatomical barriers such as the valve rings when using the LRI membrane kinetics model, which has the highest number of wavelets during AF.

The implemented method consists of eliminating new starting trajectory points according to the number of potential PSs detected around macroscopic anatomical obstacles. If a new trajectory is identified and starts at a vein/valve at which more than two PSs have been previously detected, it will not be considered as a new PS.

Figure 5.9 shows an example of the use of this constraint. When a single wavelet is split because of the superior vena cava (SVC), the two new resulting PSs ((2) and (3) in figure 5.9(B)) are not considered because of the constraint. They are therefore not assigned to any trajectory. In figure 5.9(C) two wavefronts fuse, which results in a merging at the SVC contour (PS (1+2)). Since only two PSs from the same sign are detected, the inferior

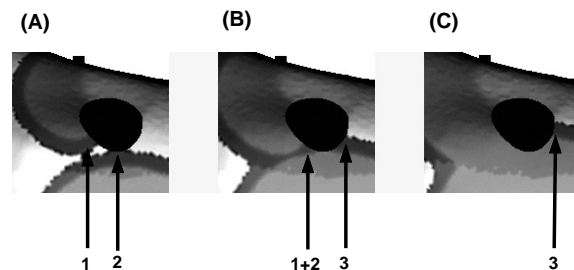


Figure 5.8 – *Illustration of an exclusion of a PS already assigned. (PSs are numbered and valve/vein are in dark). (A) Association of PS (1) and (2). (B)-(C) PS (3) cannot be associated to PS (1+2), because PS (1) and (2) are already associated.*

PS (3) is considered as a trajectory starting point. The PS (3) trajectory will continue in Figure 5.9(D) and successive phase maps.

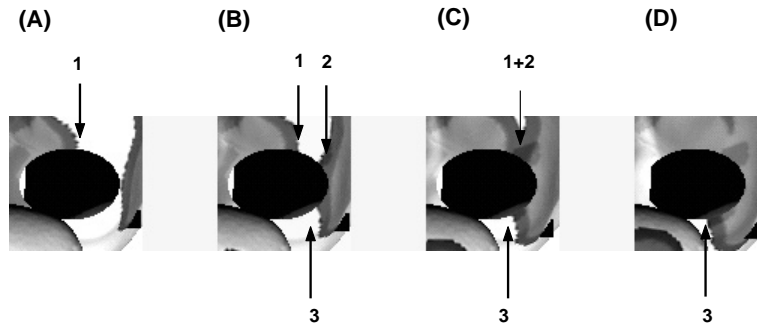


Figure 5.9 – *Illustration of the constraint on the creation of new trajectories starting at an orifice. (PSs are numbered and valve/vein is in dark).*

Figure 5.10 illustrates an example of a weakness of the constraint imposed on the creation of new trajectories starting at a vein orifice or valve ring. An error occurs when a unique wavelet, which will be split by a macroscopic anatomical barrier, is just tangent to the obstacle during one phase map as shown in figure 5.10(B). Since the limitation is only active when more than two PSs have previously been detected, no constraint is applied in such a case. Therefore the tangent point is wrongly assimilated as a true PS and a new trajectory is currently initiated.

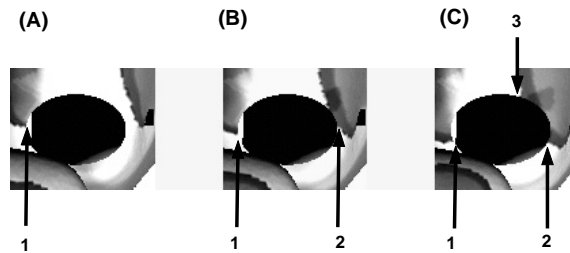


Figure 5.10 – *Illustration of the weaknesses on the constraint on the creation of new trajectories at vein orifice or valve ring. (PSs are numbered and valve/vein is in dark).*

The next three sections present results of the PS localization and tracking applied on AF simulations in the biophysical model of the atria. The analysis is mainly focused on simulations performed with the chronic AF model (section 3.3.3) using the LRI membrane kinetics. First, the total amount of PSs localized on the surface of the atria is estimated. Next, the tracking algorithm is used to study PSs lifespan. The effect of the fast inward current I_{si} , on the LRI membrane kinetics, on the PSs evolution, is investigated. Finally, the spatial distribution of PSs is considered with the inclusion of heterogeneities, with the Courtemanche-Ramirez-Nattel (CRN) membrane kinetics model.

5.5 Number of PSs during simulated AF

The time course of the number of detected PSs per phase map during simulated AF was studied in detail. In most of the cases, it oscillated between 2 and 30 (figure 5.11), which corresponds to 1 and 15 wavelets respectively.

Figure 5.11 shows the three main steps of an AF cycle for chronic AF (LRI membrane kinetics model, $G_{si} = 0.055 \text{ mS/cm}^2$ with the 50 000 nodes geometry, see section also 3.3.3), through the number of detected PSs per phase map. The number of detected PSs for the AF model after a certain delay, increased until it saturated once the fibrillation was sustained. Then it oscillated around the steady state value. The same compartment was observed by Clayton and Holden in [112] in their study of the number of filaments¹ detected in the ventricles. However the increase rates were different in the two experiments: a rise of 45 filaments was observed by Clayton in 0.7 s (64 PSs/s) whereas an increase of 30 PSs was detected in 2 s (15 PSs/s) in the biophysical model during chronic AF.

During initiation of AF on the right atrium (RA) by a burst pacing lasting 3 seconds, the mean number of PSs on the RA was 4.4, while it was 0.7 on the left atrium (LA). During steady state, the average numbers of PSs on the RA and LA were comparable, namely 6.9 PSs and 6.3 PSs, respectively. Finally, when the AF self-terminated, a decreasing average number of PSs on the LA of 3.5 was observed and 7.2 PSs for the RA.

The number of detected PSs per phase map seemed to depend mainly on the number of detected PSs in the RA as shown in figure 5.11 (in gray). This behavior can be explained by the fact that all simulated AFs were initiated near the sinoatrial node. This explains the predominant role of the RA. In addition, the RA had a larger tissue surface area than the LA and the location, number and size of macroscopic anatomical obstacles was more favorable to wavelet propagation.

At times relatively large variations in the number of detected PSs per phase map were observed. These fluctuations can be explained by considering the fibrillation phenomenon

¹The wavetip of a functionally reentrant wave in two dimensions generalizes to a linear filament in three dimensions.

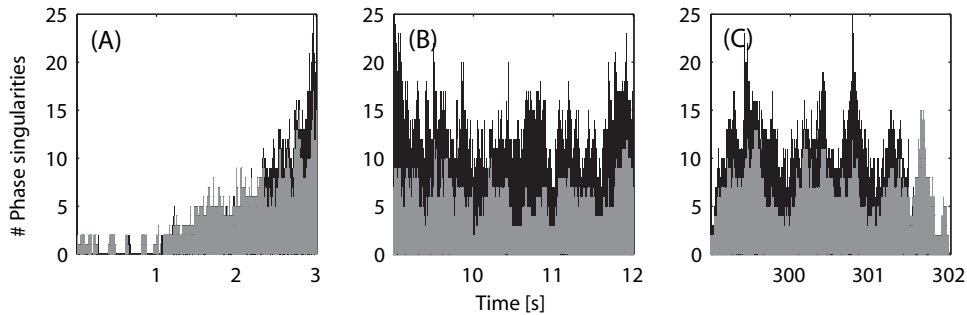


Figure 5.11 – Time evolution of phase singularities (PSs on the RA are indicated in gray and PSs on the LA are indicated in black). (A) AF initiation by a burst pacing on the RA. (B) Sustained AF. (C) Three seconds before self-termination.

as a model of an *extension of a population* with a limited amount of resources. At the beginning, the few wavelets propagated freely and collided with each other, which increased their numbers. However, once a certain amount was reached, areas of refractory period were well spread out over the whole surface. Thereby the propagation of wavelets was harder and most of them vanished, which in turn decreased the area of tissue in the refractory period.

As depicted in figure 5.11(B) the number of PSSs per phase map fluctuated around a mean value and it was observed that an odd number of PSSs were present. This phenomenon is explained in the next section. The effect of the slow inward current G_{si} on the number of detected PSSs is presented as well.

5.5.1 Parity of the number of detected PSSs

It was first thought that the number of detected PSSs was always even. Indeed wavelets have always two extremities, so two PSSs. In addition, potential incorrect detections at macroscopic anatomical obstacles, as explained in section 5.4, mostly come by pairs. However, it was noticed that sometimes an odd number of PSSs was detected. This relates to two phenomena:

- as shown in figure 5.12, it may happen that two different wavelets have a common extremity lying within the septum. The septum is the relatively small tissue area that the left and the right atria have in common. Thus, every wavelet traveling from one atrium to the other has to pass through it;
- incorrect detections at macroscopic anatomical obstacles may also happen separately. As explained in section 5.4 (figure 5.10), when a unique wavefront is just tangent to a macroscopic anatomical obstacle at which another wavefront is already anchored, the constraint imposed on the creation of new trajectories does not effectively work.

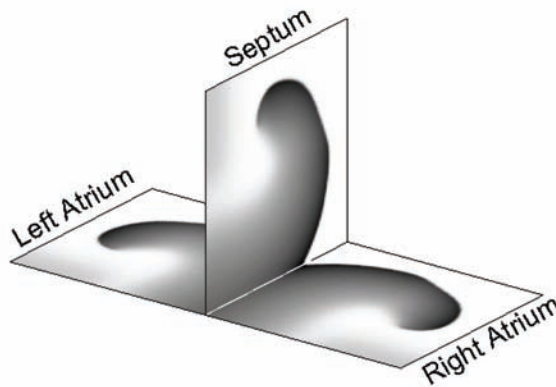


Figure 5.12 – *Phase singularities in the septum.*

5.5.2 Effect of the slow inward current G_{si}

The slow inward current G_{si} is used as a control parameter to affect the action potential duration (APD) and restitution properties of the LRI membrane kinetics model (as explained in chapter 2). Decreasing G_{si} reduces the APD and flattens the restitution curve. As the APD decreases, the mean number of wavelets increases, due to the decrease in wavelength [105]. Such a trend can be observed in figure 5.13.

In this study, the initiation phase was separated from the perpetuation phase. Sustained AF was induced using burst pacing protocol near the sinoatrial (SAN) region on the baseline membrane kinetics model. The SAN region was paced at a frequency of 20 Hz. After 3 seconds, pacing was stopped and the system evolved freely. Simulated sustained atrial fibrillation (SSAF) lasting longer than 5 minutes was obtained. Ten seconds after the beginning of the initiation, the value of the control parameter G_{si} was instantaneously reduced to produce shorter APDs and a flatter restitution curve. Five seconds of SSAF for each G_{si} value (0.085, 0.08, 0.075, 0.070, 0.065, 0.060 and 0.055) was selected to compute statistics.

In figure 5.13, statistical boxes have lines at the lower quartile, median, and upper quartile values. The whiskers are lines extending from each end of the box to show the extent of the remaining data. For display purposes, the values higher than 45 were considered as outliers and consequently not displayed. Several (up to 300) of these outliers were found for a slow inward current G_{si} of 0.080 and 0.085 mS/cm². These outliers are due to artefacts usually appearing during the initiation or self-termination of the AF simulated with high values of G_{si} . During the AF initiation process by rapid burst pacing near the SAN, when a wavefront collides with the wave tail of the previous one, its front brooked in several wavelets for only one phase map.

As expected, the higher the G_{si} value is the lower the median value of the PSs.

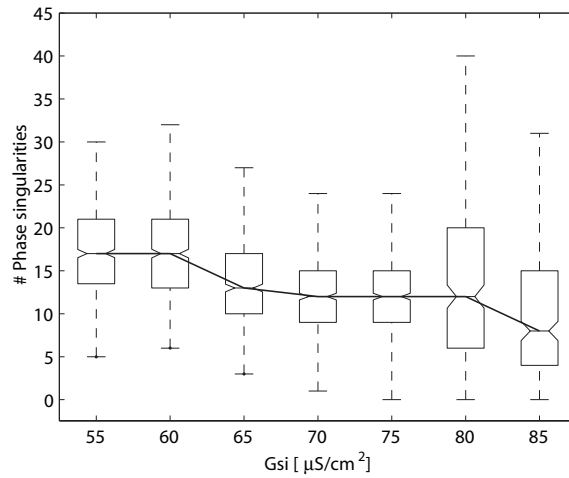


Figure 5.13 – Distribution of PSs with respect to G_{si} .

5.6 PSs lifespan during simulated sustained AF

The lifespan of the PSs, detected through different simulated sustained atrial fibrillations, were computed. In all the cases studied, the lifespan of most PSs and of their respective wavelets were found to be very short. One resulting histogram is shown in figure 5.14. The mean cycle length (CL) is indicated. The cycle length is the time interval between two successive action potential upstrokes. This duration is calculated by using the spatial and temporal average of beat-to-beat intervals recorded at each node of the meshed surface.

The lifespan distribution of figure 5.14 is skewed to the left, with 17% of PSs lasting only 5 ms or less. The mean lifespan of PSs was 94 ± 127 ms with a range of 5 ms (one phase map) to 1260 ms. A total of 69% lasted less than one mean CL (87 ms). The majority of these short-lived PSs were the result of break-up of broad spatiotemporal periodic waves [106].

Based on the experimentation made on six Langendorff-perfused sheep hearts in the presence of acetylcholine, Chen *et al.* [79] obtained significantly different results: the mean lifespan of their detected PSs was 19.5 ± 18.3 ms with approximately 98% existing less than the average cycle length. Such results could be compared by modifying the LRI membrane kinetics model. The LRI membrane kinetics model with $G_{si} = 0.080$ mS/cm² was the closest model to the results of Chen *et al.*

5.6.1 Effect of the slow inward current G_{si} on PSs lifespan

The results illustrated in table 5.1 were found after suppressing all PS durations less than or equal to 5 ms (one phase map). For all simulations processed with the LRI membrane kinetics model, AF initiations were identical.

In table 5.1, the percentage of PSs lasting more than one CL decreased from 31% to 0.2% as the slow inward conductance G_{si} was augmented. As already explained, the reason is the

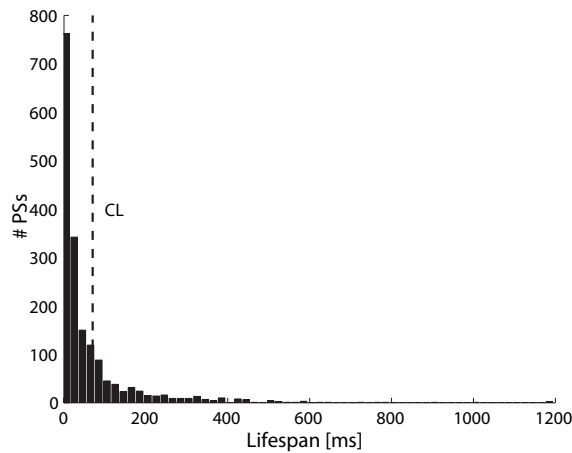


Figure 5.14 – Lifespan histogram providing from a simulation using the LRI membrane kinetics model. The dash line indicates the position of the mean cycle length (CL).

Membrane Kinetics Model	% of PSs > CL	CL	Av. Lifespan	Long. Lifespan
LRI (G_{si} [mS/cm ²])				
$G_{si} = 0.055$	31.1%	87	94±127	1265
$G_{si} = 0.060$	26.3%	99	78±89	710
$G_{si} = 0.065$	15.8%	125	66±72	590
$G_{si} = 0.070$	9.7%	131	53±61	545
$G_{si} = 0.075$	5.6%	150	46±58	570
$G_{si} = 0.080$	3.4%	167	46±42	260
$G_{si} = 0.085$	0.2%	232	36±39	245

Table 5.1 – PSs lifespan for different values of G_{si} for the LRI membrane kinetics model.

augmentation of the CL and hence so of the APD which leads to an augmentation of the area of refractory tissue. Consequently, at the same time, the limit separating short-living from long-lasting PSs is increased and the tissue becomes potentially more excitable.

5.6.2 Origin of long-lasting PSs

Some of the PSs are long lasting. One of the reasons is illustrated in figure 5.15. It displays the collision between two wavefronts with PS(1) and PS(2) trajectories. Whereas no doubt exists for PS(2), one could hesitate about the trajectory of PS(1). Indeed, two cases are most probable:

- the wavelet tip PS(1) in figure 5.15(C) is a new PS. The appearance of this new PS is due to the split of one wavelet;
- the PS(1) is the same over the three figures 5.15(A-C). This continuation is the result of the merging of two wavefronts with a part of the left-situated wavefront between figure 5.15(B-C).

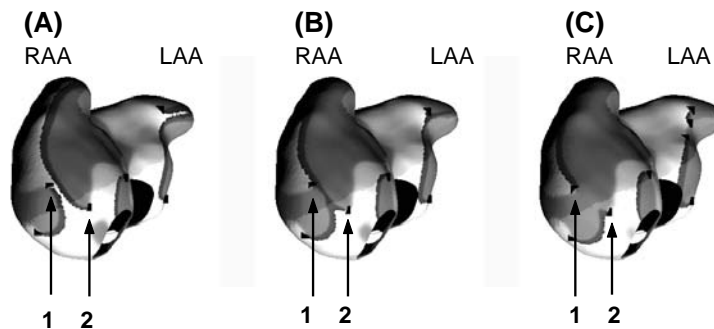


Figure 5.15 – Illustration of provenance of long-lasting PSs.

Since both situations are equal, the continuation solution was chosen arbitrarily for implementation simplification. If the first case is chosen, an algorithm on wavefront detection and tracking should be implemented, which was not studied in this work.

5.7 Spatial distribution of PSS

5.7.1 PS localization on a homogenous surface

In order to study the distribution of PSS on the epicardial surface of the atria, the chronic AF model was used (section 3.3.3). Fibrillation was initiated by a burst pacing near the sino-atrial node for 3 s at a frequency of 20 Hz. Following simulated sustained AF (10 s after the beginning of burst pacing), PSS were localized and tracked during 5 s. The coordinates of all PSS were recorded and displayed on the surface of the atrial geometry. Figure 5.16(A-F) presents the trajectory of PSS with a lifespan longer than 100 ms, 300 ms, 500 ms, 700 ms, 900 ms and 1000 ms, respectively. As expected, longer PS lifespans were mainly located on the RA, confirming the previous result (section 5.5) that higher numbers of PSS were found on the RA. The LA, due to its small area, does not allow long lifespans. The longest lifespan recorded (table 5.1) was localized around the left superior pulmonary vein.

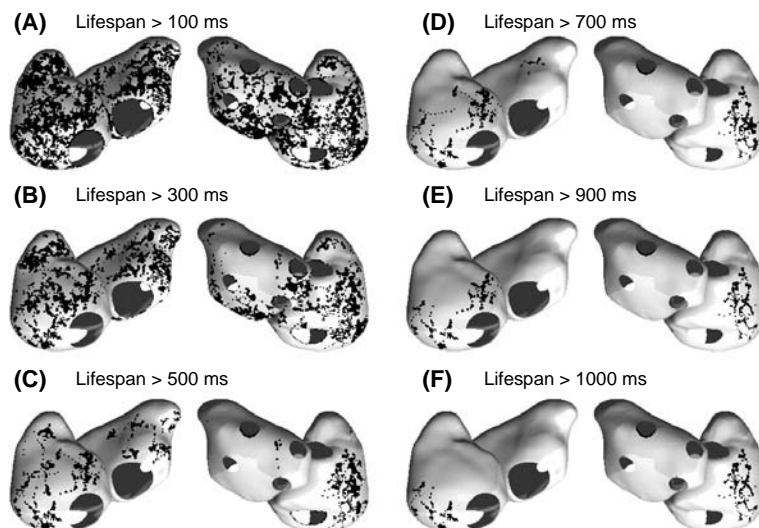


Figure 5.16 – Phase singularities localization during sustained AF using the LRI membrane kinetics model. (A) Trajectories > 100 ms. (B) Trajectories > 300 ms. (C) Trajectories > 500 ms. (D) Trajectories > 700 ms. (E) Trajectories > 900 ms. (F) Trajectories > 1000 ms.

5.7.2 PSs localization on an inhomogeneous surface

Three types of inhomogeneity were applied: (1) homogenous, (2) anisotropic and (3) heterogeneous. A fiber structure was included, based on histological data [5]. The anisotropy ratio between the longitudinal σ_l and transverse σ_t conductivities was set to 9:1 [5]. Heterogeneities were included, as previously described in section 3.3.5.

Different types of AF model using the CRN membrane kinetics model were used in these experiments. The meandering AF model (section 3.3.4) was used in the homogeneous and the anisotropic surface. The cholinergic AF model (section 3.3.5) was implemented on the heterogeneous surface. A period of five seconds of sustained AF was selected for each example of inhomogeneous surface in the PS analysis.

Table 5.2 presented results for the different types of inhomogeneity using the CRN membrane kinetics model. The CRN meandering AF model (see section 3.3.4) was specially developed to approximate the human atrial cells. Its action potential duration is longer than the LR1 membrane kinetics model and thus the meandering AF model is harder to fibrillate. Its percentage of PSs lasting less than one mean CL (table 5.2, homogenous) was closer to the value obtained by Chen *et al.* in [79] than the LR1 membrane kinetics model (table 5.1). Nevertheless, its mean PS lifespan was still too high. The addition of anisotropy did not affect significantly either the percentage of PSs longer than CL or the average lifespan. However heterogeneity increased the percentage of PSs longer than CL and their average lifespan. Furthermore, the membrane kinetics model used in addition to heterogeneity was the cholinergic AF model (section 3.3.5). Such a model has a very short APD, which allows easy maintenance of reentries.

Figure 5.17 presents the spatial localization of the different types of inhomogeneity included and the trajectories of PSs. The histogram of the lifespans is also displayed. For a homogeneous surface, PSs were uniformly distributed on both atria. Inclusion of anisotropy caused PS trajectories to be predominantly oriented along fibers, especially on the right atrium. Adding heterogeneity, PSs were detected around the discontinuity islands. Since they were rotating around these islands, the long lifespan of these found for the Heterogeneity I (table 5.2) was very long (5000 ms).

Inhomogeneity	% of PSS > CL	CL	Av. Lifespan	Long. Lifespan
CRN membrane kinetics model				
Homogenous	0.9%	274	30 ± 47	815
Anisotropy	0.5%	253	32 ± 39	340
Heterogeneity I	14.3%	74	48 ± 139	5000
Heterogeneity II	19.6%	89	57 ± 109	1310

Table 5.2 – PSS lifespan for different types of Inhomogeneities.

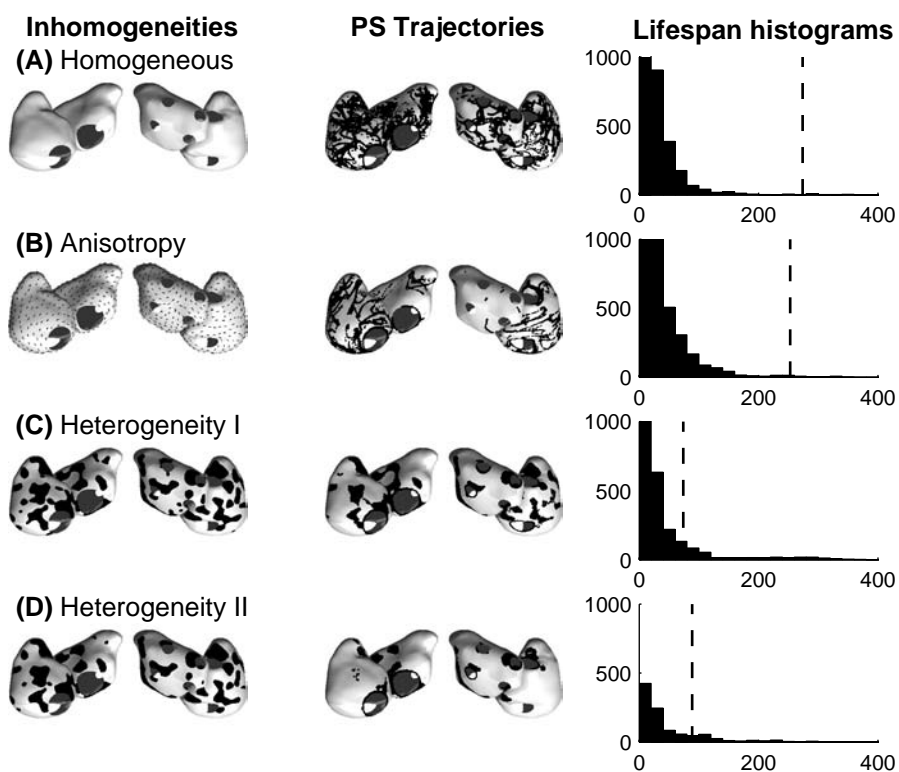


Figure 5.17 – Phase singularities trajectories for different types of inhomogeneities. Cycle length as indicated by the dashed lines in the lifespan histograms.

5.8 Conclusions

In this chapter, a new tool is described, which has been developed for a better understanding of the relatively unknown process of arrhythmias and in particular, atrial fibrillation.

The work was largely divided into three main steps: First the automatic localization of phase singularities, then their tracking, and finally the analysis of the obtained results. Their tracking was used to determine their favorite spatial location and lifespan during different simulations such as AF initiation, sustained AF and AF self-termination. Simulations were performed using several variants of the Luo-Rudy I and the Courtemanche-Ramirez-Nattel membrane kinetics model, as well as with the inclusion of different inhomogeneities.

Through all simulations it was found that most PSs were mainly located close to the large anatomical obstacles (MV, TV, SVC and IVC). The long-living PSs were clustered in space over the right and left atrium free wall. Through the analysis, it was observed that the PS lifespan depended on the membrane kinetics used for simulations. Relatively large differences in the lifespan distribution were noticed (from 31% to 0.2% of PSs lasting more than one cycle length). The addition of heterogeneities favored PS anchoring and long lifespan.

The algorithms developed in this study are robust and suitable for studying AF on the biophysical model of human atria. The PS localization process proposed is dedicated for a surface meshed with triangular element. The method proposed is a promising tool to localize and track PSs and can be used to classify several types of pathology associated with AF.

Part III

Therapies

The third part concerns the therapy methods investigated processes to cardiovert and prevent atrial arrhythmias. Its first part (chapter 6) deals with surgical ablation, a common clinical procedure. The second chapter (chapter 7) of this part focusses on more recent techniques using low electrical energy stimulation.

Surgical and catheter ablation

6

6.1 Introduction

ABLATION is a surgical procedure that cures atrial fibrillation by interrupting the sustained wavefronts that cause the abnormal heart rhythm. The surgical act involves making incisions in one or both atria. When the incisions heal, scar tissue forms, which blocks any abnormal sustained wavefront. In so doing, it corrects all major problems associated with atrial fibrillation: it stops atrial arrhythmia, it restores normal rhythm between the atria and the ventricles, and it preserves the ability of the atria to contract on its own. Present day ablation procedures can eliminate tachyarrhythmia with success rates between 70% and 100% and complication rates of < 1% to 2% [120].

In the 1980s several surgical procedures were introduced [121–123]. After one decade of experimental studies Cox *et al.* proposed an extremely effective ablation pattern based on the concept of a maze, namely the *Maze-III procedure* [124–126]. The Maze-III is used for patients, who need valve replacement. This procedure requires an open-heart operation. It necessitates a cardiopulmonary bypass that consists of the excision of the atrial appendages, isolation of the pulmonary veins, and creation of a narrow, tortuous path of atrial tissue by carefully placed incisions. This directs the sinus node impulses across the atria to the atrioventricular node. The incisions are placed so that no area is wide enough to sustain multiple reentry circuits, and thus atrial fibrillation cannot occur.

Over the past ten years, the development of new surgical instruments with energy delivered through catheters, provide an alternative to surgical ablation. These techniques are less invasive and the source of energy delivered by the catheters has several sources: radiofrequency (RF) , cryoablation, laser and ultrasound [127]. The first generation of

RF energy used in ablation techniques creates a burn in heart tissue, thereby destroying the areas of the heart generating AF. This burn can cause swelling and narrowing of the pulmonary vein (PV) openings, sometimes resulting in what is called PV stenosis. Also, particles of burnt tissue debris from RF ablation may get into the blood stream, causing blockages and even strokes. Current RF ablation techniques use cooled-tip and low wattage catheters to avoid these problems. Cryoablation, by freezing heart tissue rather than burning it, has the potential of eliminating the swelling (stenosis) after ablation. Laser and ultrasound methods, by not damaging the surface of heart tissue, have the potential of eliminating the damaged tissue debris that may get into the bloodstream when using RF ablation.

Based on the maze operation and other compartmentalization of specific anatomical features, different series of lesion patterns were suggested. An ideal pattern should prevent AF with the minimum number of ablation lines of minimal length, while allowing for a good contraction of both atria during sinus rhythm. This optimal ablation pattern is still unknown [128, 129]. Atrial ablation with ligation of the atrial appendages reduces atrial function relative to normal controls in sinus rhythm [130]. The clinical significance of this reduction has not yet been accurately assessed. Transthoracic Doppler echocardiography has been the most frequently used method of measuring atrial contraction after AF surgery, although its clinical usefulness has not been established [131].

Evaluation of the various lesion patterns is usually performed in clinical studies or in animal experiments. The main drawbacks of animal experiments are the difficulty of accessing the whole atria and the differences between animal and human hearts. An alternative is the use of a biophysical model of AF to evaluate the effect of different ablation patterns and to bring insight into the underlying mechanisms. Compared to clinical and animal studies, this approach has the advantage of repeatability of experiments under controlled conditions. This approach is discussed in this chapter.

In the first part, simulations of several standard maze and simpler surgical/RF procedures are presented applied on the chronic AF model (section 3.3.3). The second part evaluates the effect of imperfections in the standard Maze-III procedure and in the isolation of pulmonary veins is studied. In the third part, several isolations of the pulmonary veins procedure are analyzed. In the fourth part, comparison with clinical study is performed. Finally, an ideal ablation pattern based on the Maze-III is proposed at the end of this chapter.

6.2 Modelling ablation patterns

This section presents the different ablation patterns used during this work. First the implementation of the ablation line is described. Then the different ablation patterns are introduced: standard mazes, simpler surgical/RF ablation patterns, isolation of the pulmonary veins and an ideal ablation pattern. Third, imperfect ablation lines are added in the Maze-III, in the pulmonary veins isolations and in the Mini-Maze proposed by Ruchat [132],

which is used for the comparison with clinical study.

6.2.1 Ablation lines implementation

Ablation lines are therapeutic interventions that can be easily simulated in a computer model of atrial fibrillation [133, 134]. In the biophysical model, surgical/RF ablation lines are simulated by setting the conductivity tensor to zero between the cardiac cells located on both sides of the ablation line. The lines obtained correspond to ideal ablation lines, continuous and transmural (monolayer surface). To build an ablation line in the geometry, two nodes of the triangular mesh are selected (figure 6.1(A)). A principal vector is constructed between the starting node (S) and the end node (E). Vectors \overrightarrow{SE} from the starting node to its neighbor nodes (N_i) are computed. Each vector is projected on the principal vector and the vector with the largest projection value is selected as the new starting node (S') (figure 6.1(B)). The principal vector is then updated with this new node (figure 6.1(C)). The procedure is repeated until the end node is reached. Finally, the nodes which are selected during the iteration are part of the ablation line and their conductivities to their neighbors are set to zero (dashed line in figure 6.1(D)).

6.3 Simulated ablation patterns

6.3.1 Standard maze patterns

The objective of this section is to outline the different surgical procedures that have formerly been used in the treatment of atrial fibrillation. Four typical maze procedures, including the standard Cox's Maze-III, were tested. For which a high success rate was reported (> 90%) [129], in which both surgical and RF catheter procedures were included. The

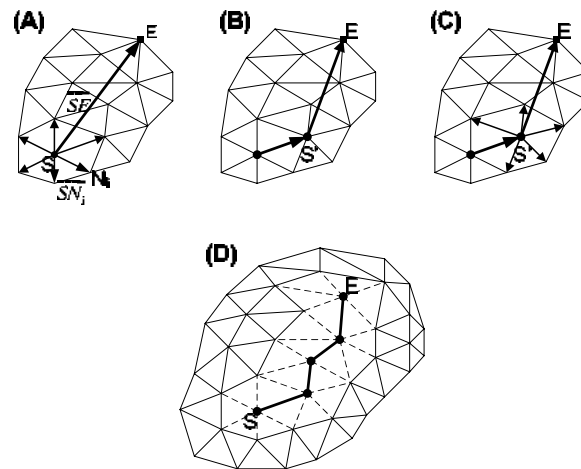


Figure 6.1 – Ablation line implementation: (A) Selection of the starting node and the end node. (B) Update of the starting node. (C) Selection of neighbor node. (D) Nodes on the ablation line.

ablation lines are reported as black lines on the MRI geometry in figure 6.2. Ablation line lengths, total boundary lengths (including ablation lines, valves and veins boundaries) and isolated areas are also indicated. The range of line lengths and isolated regions are highly variable, from 21.7 cm to 45.2 cm, and from 9.7 cm² to 32.2 cm².

The Maze-III (figure 6.2(A)) procedure isolates the region around the pulmonary veins (PVs), the left appendage (LA) and right appendage (RA), which represents approximately 20% of the entire atrial surface. The radiofrequency maze (RF-Maze, figure 6.2(B)) presented by Sie in [135] is inspired by the previous one but instead of having the PVs fully encircled by ablation lines, the right superior and inferior pulmonary veins are isolated separately from the left superior and inferior pulmonary veins. The main difference lies in the technique used to create ablation lines. The Maze-III is performed by surgical incisions and undergoing an open-heart surgery, whereas the RF-Maze use RF ablation, which is less invasive and time-saving. The radial incision approach maze (RIA-Maze, figure 6.2(C)) proposed by Nitta in [136] is a quite new experimental maze procedure which involves less isolated areas, allowing thus a better contraction of the atria. The particularities of this maze, as its name indicates, are the two radial ablation lines on the left atrium that do not

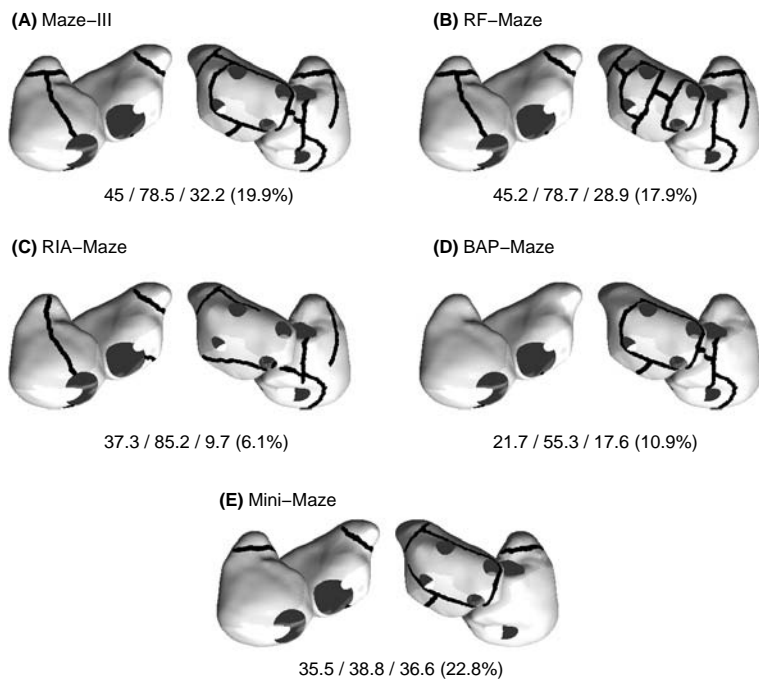


Figure 6.2 – Standard maze patterns. Under each pattern: ablations length (cm) / total boundaries due to ablation lengths and perimeters of natural obstacles such as veins and valves (cm) / isolated tissue surface (cm²) (percentage) are indicated. (A) Cox’s Maze-III procedure. (B) Radiofrequency modified maze procedure. (C) Radial Approach maze. (D) Bilateral appendage preserving maze. (E) Mini-Maze

isolate the pulmonary veins. The bilateral appendage-preserving maze procedure (BAP-Maze, figure 6.2(D)) suggested by Isobe in [137] preserves the two appendages, which are presumed to contribute to atrial transport and atrial natriuretic. More recently, Ruchat and co-workers [132] have proposed the Mini-Maze procedure (Mini-Maze, figure 6.2(E)). It is based on the Maze-III but involves only LA compartmentalization

6.3.2 Simpler surgical/RF patterns

Eleven less invasive patterns (figure 6.3) were also evaluated. Among these, some reflect the most commonly used in the clinic. The first row in figure 6.3 involve right atrial ablation lines only: a single ablation line through the isthmus between the inferior vena cava (IVC) and the tricuspid valve (TV) (figure 6.3(A)), a single ablation line between the superior vena cava (SVC) and IVC (figure 6.3(B)), and a combination of the two previous patterns (figure 6.3(C)). Two ablation patterns are limited to the left atrium: ablation lines connecting all four pulmonary veins (figure 6.3(D)), and ablation lines completely isolating the pulmonary veins (figure 6.3(H)). The six remaining ablation patterns involve both atria (figure 6.3(E-G) and figure 6.3(I-K)). The estimated total length of the ablation lines, approximated by the Euclidian distance between nodes arbitrarily placed along the line, ranges from 1 cm for the simplest pattern (figure 6.3(A)) to 45 cm for the Maze-III pattern of figure 6.2(A). The ablation patterns on the third line in figure 6.3 include a

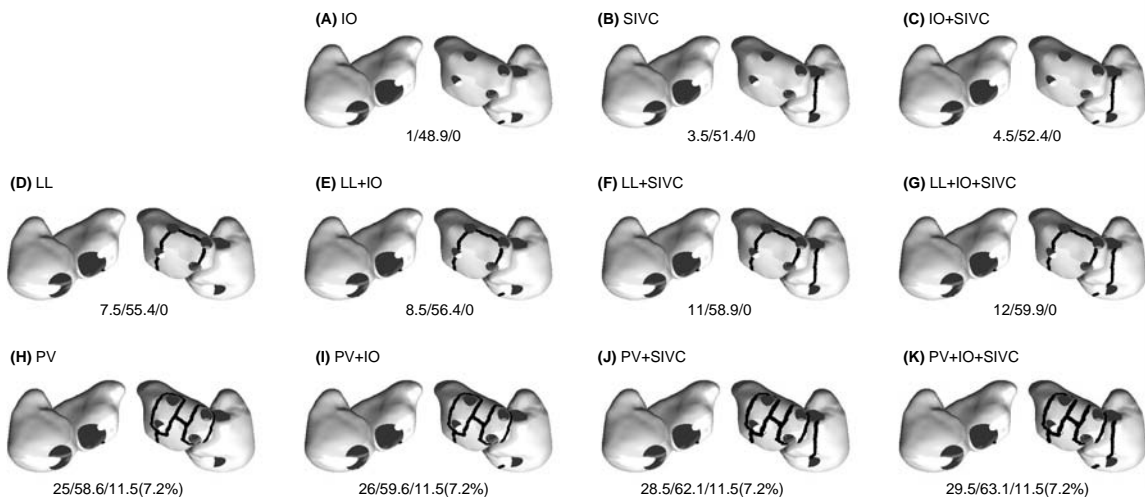


Figure 6.3 – Simple surgical/RF patterns. Under each pattern, ablations length (cm) / total boundaries due to ablation lengths and perimeters of natural obstacles such as veins and valves (cm) / isolated tissue surface (cm²) (percentage) are indicated. (A) Isthmus only, IO. (B) Sup./Inf. vena cava line, SIVC. (C) IO and SIVC, IO+SIVC. (D) Left line only, LL. (E) Left line and Isthmus, LL+IO. (F) Left line and Sup./Inf. vena cava line, LL+SIVC. (G) Left line, Isthmus and Sup./Inf. vena cava line, LL+IO+SIVC. (H) Pulmonary ablation lines, PV. (I) PV and IO, PV+IO. (J) PV and SIVC, PV+SIVC. (K) PV, IO and SIVC, PV+IO+SIVC.

complete isolation of the pulmonary vein region, implying that no electrical activity can be propagated from the pulmonary veins to the atria. The isolated area is 11.5 cm^2 , i.e. 7.2% of the whole atrial tissue. For the Maze-III procedure of figure 6.2(A), the isolated area is 32.2 cm^2 , i.e. 19.9% of the whole atrial tissue.

6.3.3 Isolation of the pulmonary veins

Pulmonary vein isolation (PVI) is commonly used to treat AF [72, 138]. Increasing the size of the isolated area possibly eliminates more foci and prevents them from triggering AF. However, larger isolated areas may be a substrate for atrial flutter (AFL) by creating narrow conduction isthmuses or anchoring sites. PVI was implemented in different patterns with increasing surface of excluded tissue. Figure 6.4(A-C) presents three different sizes of circular PVI: (A) Individual PVI 5 mm from ostia (10 cm^2 excluded area); (B) Individual PVI 7.5 mm from ostia (17 cm^2 excluded area) and (C) Individual PVI 10 mm from ostia (26 cm^2 excluded area) virtually resulting in posterior LA isolation.

Instead of having PVs individually isolated, some techniques isolate the PVs two by two [139]. Figure 6.4(D-F) presents three patterns with different distances d ($d = 5, 2.5$ and 0 mm) between the set of isolated PVs.

The pattern of figure 6.4(D) was also combined with linear ablation lines: a roof line between the two PV isolation areas in the upper left atrial region (figure 6.4(G)), a left

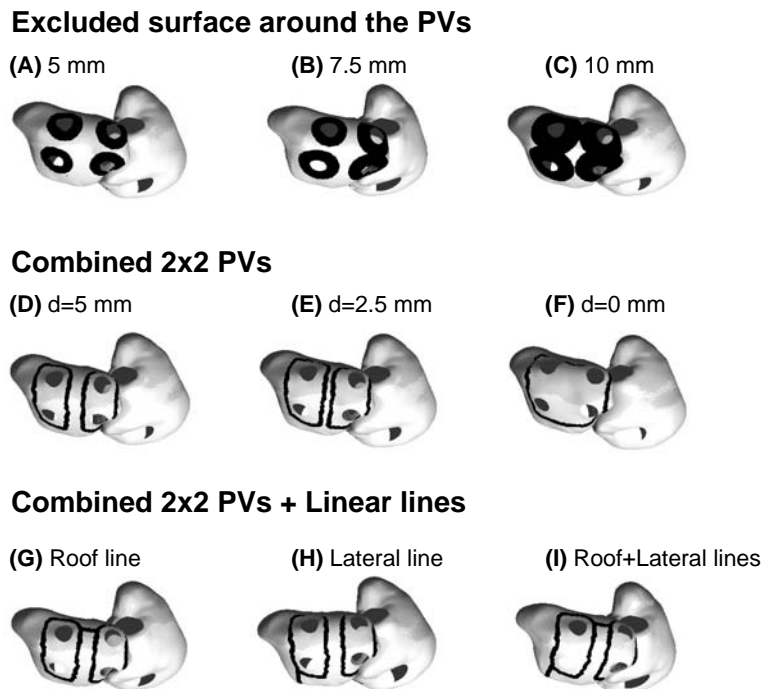


Figure 6.4 – Isolation of the pulmonary veins.

isthmus line connecting the left PV isolation area and the mitral valve (figure 6.4(H)), and both previous lines (figure 6.4(I)).

This study determines the effect of the distance d ($d = 5, 2.5$ and 0 mm) between the set of isolated PVs (figure 6.4(D-F)). For each linear lesion a conduction gap (see section 6.4) of 3 mm was also introduced in the middle of the line to evaluate the incidence of AFL.

6.3.4 Proposition of an ideal ablation pattern

The surgical Maze-III is the gold standard for the treatment of AF; however because of technical difficulties and high risks, less invasive ablation alternatives are investigated clinically. The present study identifies such alternative patterns. Figure 6.5 presents six different modified Maze-III procedures. Progressively ablation lines were implemented respectively around pulmonary veins (PV), left atrial appendage (LAA), left atrial isthmus (LAI), Cosio'isthmus (CI) and intercaval lines (SIVC), defining progressively modified Maze III patterns: MMP1=PV, MMP2=MMP1+LAA, MMP3=MMP2+LAI, MMP4=MMP3+CI, MMP5=MMP3+SIVC, MMP6=MMP5+CI.

6.4 Imperfect ablation lines

In clinical procedures, RF ablation lines are sometimes applied only to the endocardial side and the ablation lines may be incomplete. This introduces gaps allowing atypical flutter or fibrillation recurrence. Figure 6.6 depicts the two types of problems. The first one is due to a discontinuity in the ablation line when the surgeons misalign two lines. The second one is the non-transmurality during RF ablation. If the energy delivered by RF or cryo -ablation is too low or the time of energy application on the tissue is too short, non-transmurality can occur.

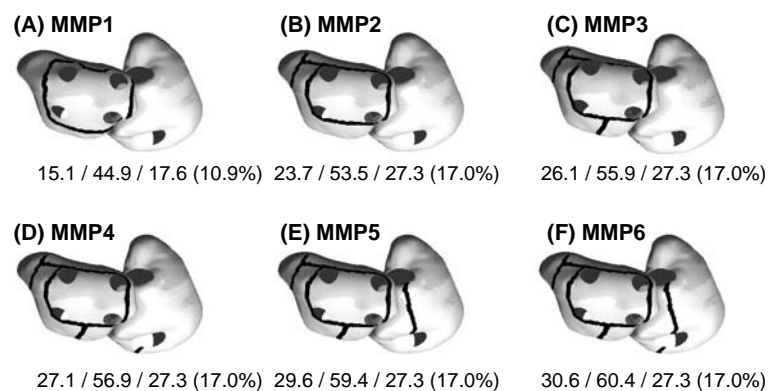


Figure 6.5 – Modified Maze III patterns. Under each pattern, ablations length (cm) / total boundaries due to ablation lengths and perimeters of natural obstacles such as veins and valves (cm) / isolated tissue surface (cm²) (percentage) are indicated.

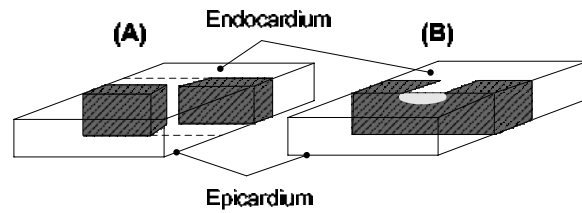


Figure 6.6 – Ablation gap types. (A) Discontinuity gap. (B) Non-transmural gap.

6.4.1 Incomplete Maze-III procedure

To reproduce these phenomena, discontinuities in the Maze-III ablation patterns were simulated. The first discontinuity (Gap I in figure 6.7) was placed along the ablation line connecting the pulmonary veins and the mitral valve annulus and the second (Gap II in figure 6.7) along the ablation line connecting the upper pulmonary veins. Four gap widths (1.3, 1.7, 2.4, and 3.0 mm) were simulated in the middle of the ablation line; the widest gap was also tested at both extremities of the ablation line. This protocol allowed the study of the effect of gap width and position separately with a minimum number of simulations.

6.4.2 Incomplete linear lesion in pulmonary veins isolation

For each linear lesion of the pulmonary vein isolations (figure 6.4(G)-(H)) a conduction gap of 3 mm was also introduced in the middle of the line. The objective was the study of AFL incidence.

6.4.3 Incomplete ablation line in clinical study

Further simulations were performed to compare the results obtained on the biophysical model with clinical data. The comparison is based on a simplified Maze-III procedure using RF ablation (Mini-Maze, figure 6.2(E)). This pattern has already been applied to 46

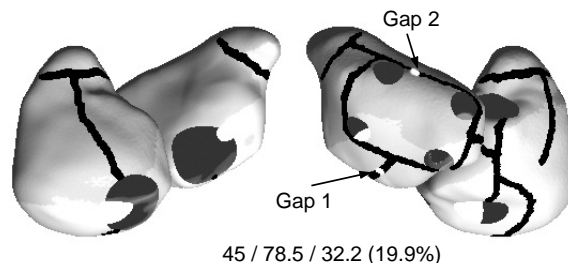


Figure 6.7 – Imperfect Cox's Maze-III procedure. Ablation lines are marked by dark lines and positions of introduced gaps are indicated by arrows. Gap 1 and Gap 2 have a gap width of either 1.3 mm, 1.7 mm, 2.4 mm and 3.0 mm. Ablations length (cm) / total boundaries due to ablation lengths and perimeters of natural obstacles such as veins and valves (cm) / isolated tissue surface (cm²) (percentage) are indicated.

patients with permanent drug refractory AF [132] and it was implemented in the biophysical model. The RF left atrial compartmentalization was performed during mitral valve repair or replacement in which the patients were divided into two groups: Group I with endocardial RF application only (20 patients) and Group II with both endo and epicardial RF application (26 patients). Both groups of patients were similar in terms of age, AF duration and left atrial size. Group II was modelled using the Mini-Maze of figure 6.2(E) with perfect ablation lines, while Group I was simulated in the biophysical model with a gap width of 3 mm on the left isthmus to mimic non-transmurality of the ablation.

6.5 Simulation protocol

6.5.1 Initiation of AF and application of ablation patterns

Before being able to test the different ablation patterns on the biophysical model, sustained AF needs to be initiated (see chapter 3). To this end, the SAN region was paced at a frequency of 20 Hz. After 3 seconds, pacing was stopped and the system evolved freely. Episodes of simulated sustained atrial fibrillation (SSAF) lasting longer than 5 minutes were obtained. To obtain suitable and random initial conditions (IC), several episodes of SSAF were selected with an interval of 1 s after the end of the burst pacing (*i.e.* 10 s after the beginning of burst pacing) for the application of the ablation patterns (further details on the ICs are discussed in section 6.5.2). These patterns were applied abruptly, after which the time to AF termination (TAFT) was documented. If no termination was observed within 30 seconds the ablation was considered as unsuccessful. This process was repeated for each of the ablation patterns studied.

For the perfect Maze-III maze procedure, a total of 118 simulations were performed with initial conditions selected successively with an interval of 1 s during sustained AF. For each of the three other standard maze patterns (figure 6.2(B-D)), the other 11 simpler ablation patterns (figure 6.3(A-K)), and the pulmonary vein isolation patterns (figure 6.4), 20 simulations were performed using the first 20 ICs used for the Maze-III protocol.

To evaluate the effect of imperfect ablation lines, the 118 initial conditions previously selected for the perfect Cox's Maze-III procedure were also used to simulate discontinuities in this pattern (gaps as shown in figure 6.3). Next, 20 and 26 time instants respectively were selected to simulate the Mini-Maze ablation in Group I and Group II (figure 6.2(E)). For the PVI patterns, 30 ICs were selected to simulate gap in the additional line of the two pulmonary veins isolation patterns (figure 6.4(G-H)). Finally, 40 simulations were performed for the definition of the appropriate ablation pattern in modified Maze-III (figure 6.5(A-F)).

TAFT values for the simulations ranged from 0.25 to 30 s. The computation time was approximately 1 h for 1 s of simulation on a standard PC (Pentium-III 1.4 GHz).

6.5.2 Measure of organization

The state of before the application of the ablation patterns was characterized by two variables. The first variable is the percentage of excited tissue, i.e. percentage of nodes with an action potential above a fixed threshold (-60 mV). The second variable is the number of wavelets, defined as the number of connected regions of excited tissue (see chapter 3). Figure 6.8(A) shows the time course of these two variables as observed in the biophysical model. The percentage of excited tissue evolved in a range from 25.3% to 72.2% and the number of wavelets from 1 to 11. The correlation coefficient between the percentage of excited tissue and the number of wavelets was -0.53 . The time course of these variables exhibited a stationary nature. This was confirmed by comparing these curves to the corresponding ones observed at a latter time interval (figure 6.8(B)).

To evaluate the effect of each ablation pattern, the average beat-to-beat interval (ABBI) over time was computed at each node of the mesh just after the application of the ablation patterns. The distribution of these values was displayed as a map on the surface of the atria. A small ABBI value means short action potential durations inducing re-entries and rapid multi-wavelet breaks, whereas a large ABBI value means long action potential durations leading eventually to an atrial cardioversion. ABBI values were documented for each ablation pattern either for the simulation having the longest time to AF termination value or for an unsuccessful termination.

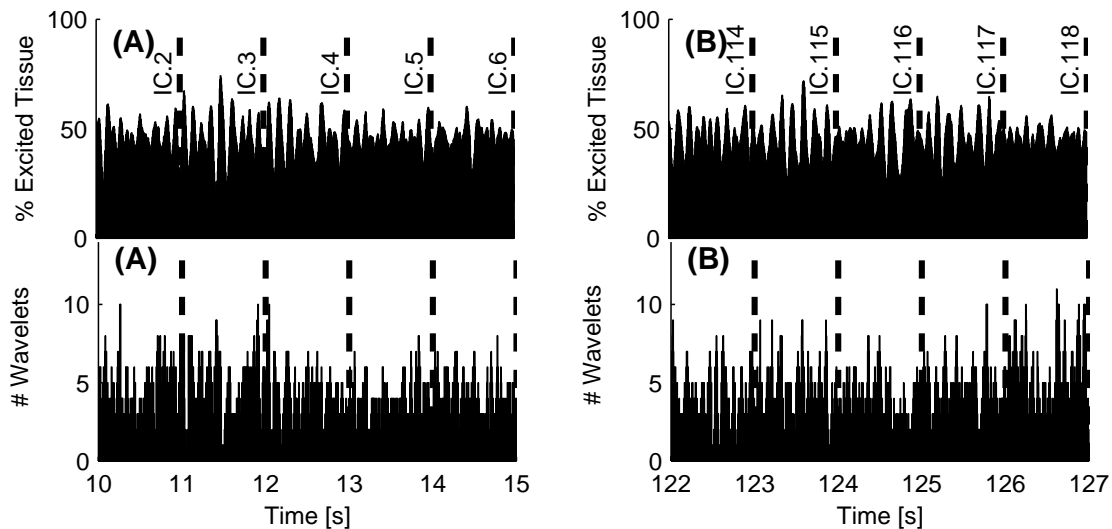


Figure 6.8 – Initial conditions selected for the application of ablation patterns. Percentage of excited tissue and number of wavelets with respect to time. (A) First initial conditions: IC.1 to IC.6. (B) Last initial conditions: IC.113 to IC.118.

6.6 Impact of initial conditions

All of the 118 simulations of the Cox Maze-III procedure were successful in stopping AF, with a mean TAFT equal to $1.3 \text{ s} \pm 0.8 \text{ s}$ (mean \pm standard deviation). Figure 6.9(A) and figure 6.9(B) show respectively the percentage of excited tissue and the number of wavelets before application of the Cox Maze-III procedure with respect of the TAFT. The results suggest that there is no significant correlation between AF termination and the percentage of excited tissue or the number of initial wavelets. This means that a simple isolated wavelet that is not blocked by the ablation lines may generate or maintain a sustained atrial fibrillation. Conversely, an initial state having several wavelets may rapidly lead to a short TAFT value, because these wavelets can block or annihilate another.

6.7 Comparison of the efficiency of ablation patterns

The present section present results of ablation procedures applied on chronic AF simulations (section 3.3.3) in the biophysical model of the atria. First, the results of standard mazes are presented. Second, a comparison of simplifier ablation patterns patterns is exposed. Third, results on imperfect Maze-III procedure are discussed. Fourth, isolation of pulmonary veins patterns are investigated, as well as the effect of gap in these patterns. Fifth, a comparison with a clinical study is performed. Finally, result obtained with the ideal ablation pattern is presented.

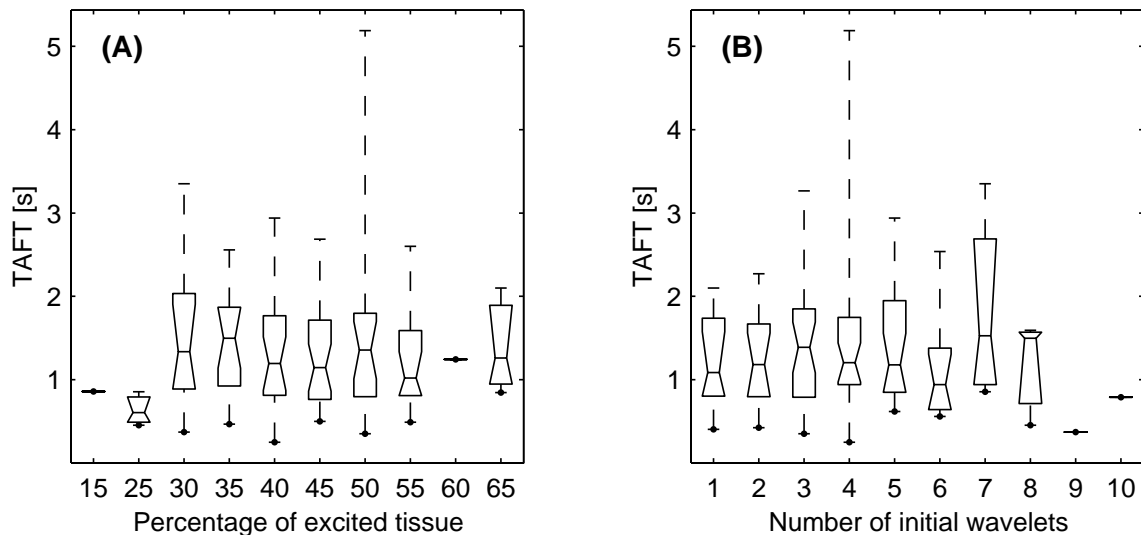


Figure 6.9 – (A) TAFT vs. percentage of excited tissue. (B) TAFT vs. number of initial wavelets. The boxes have lines at the lower quartile, median, and upper quartile values. The whiskers are lines extending from each end of the box to show the range of the data.

6.7.1 Standard maze patterns

The percentages of successful conversion for the four standard maze patterns of figure 6.2 are summarized in table 6.1. The ABBI values were computed for each ablation pattern and their distributions are shown in figure 6.10 with grey color code: ABBI value ranged between 70 ms (in a dark grey color, i.e. short action potential) and 140 ms (in a light grey color, i.e. long action potential) corresponding to frequencies of 14.3 Hz and 7.1 Hz, respectively. Among the ablation patterns achieved, the most efficient pattern remains the standard Cox’s Maze-III procedure, with an AF termination success rate of 100% and the smallest mean TAFT value of $1.3 \text{ s} \pm 0.8 \text{ s}$. The RF-Maze, which is quite similar to the Maze-III procedure has also a success rate of 100% with a mean TAFT only slightly longer ($1.6 \text{ s} \pm 0.8 \text{ s}$). The two other maze patterns (RID-Maze and BAP-Maze) which have isolated regions approximately decreased in half with regard to the Maze-III, have as a consequence an increase of their mean TAFT. As expected, the larger the isolated surface, the shorter the time to AF termination is. The residual surface did not induce wavelets reentries. This effect is confirmed by the distribution of the ABBI value on the surface of the atria. The RID-Maze and BAP-Maze obtained a low ABBI value ($\sim 90 \text{ ms}$) on the left atrium and right atrium, meaning a short action potential between each wave front. With the RID-Maze procedure, it appeared some unsuccessful cardioversions lead to an uncommon flutter around the left appendage (figure 6.11), not reported in clinical data [136].

Among the simulated ablation patterns, the most efficient is the Maze-III procedure with a success rate of 100% and the smallest mean TAFT value of $1.3 \pm 0.8 \text{ s}$. This ablation pattern is able to terminate AF independently of the initial states in the tissue at the moment of application of the lines.

The success rate obtained is in agreement with clinical data, where the complete surgical Maze-III pattern had the highest long-term success rate ranging from 80 to 99% [129, 140–142]. Limitations of this surgical maze necessitate the performance of an open-heart surgery, the time-consuming nature of the procedure and the related complications. RF ablation represents a less invasive alternative. However the surgical Maze-III procedure is technically difficult to reproduce using RF due to frequent discontinuities in the ablation

Patterns	Mean TAFT	Suc. Termination	Flutter
Maze-III	$1.3 \pm 0.8 \text{ s}$	100%	0%
RF-Maze	$1.6 \pm 0.8 \text{ s}$	100%	0%
RIA-Maze	$4.7 \pm 2.7 \text{ s}$	75%	25%
BAP-Maze	$4.6 \pm 3.5 \text{ s}$	100%	0%

Table 6.1 – Mean TAFT for the standard maze procedure patterns.

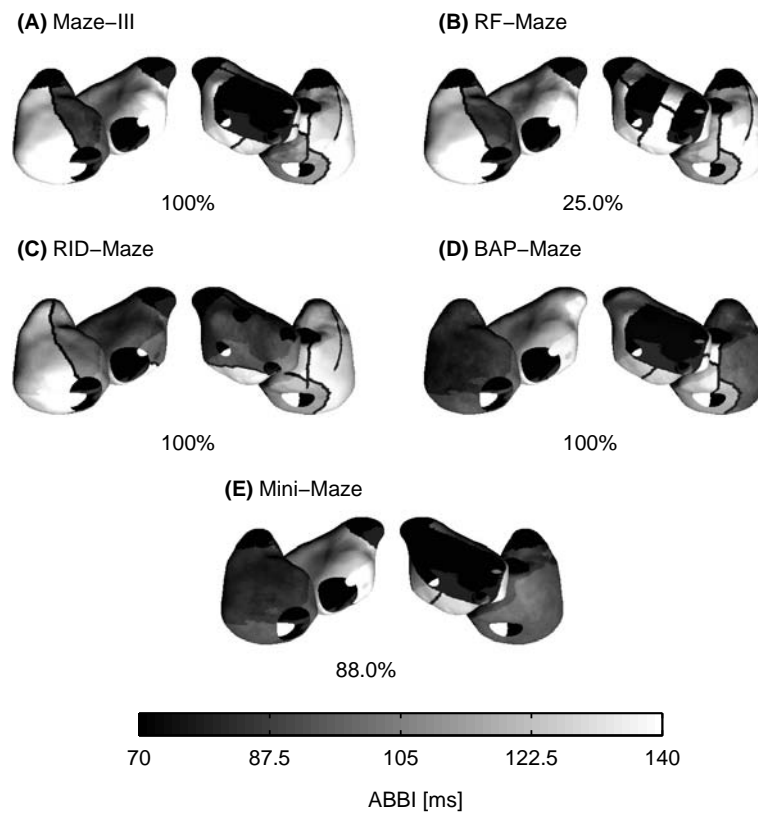


Figure 6.10 — Percentage of success rate and distributions of the average beat-to-beat intervals (ABBI) for each of the standard maze procedures (ablation lines and isolated regions are resented in dark):

lines, especially if ablation is performed from the endocardial side only.

6.7.2 Simpler surgical/RF patterns

The percentages of successful conversion for the 11 ablation patterns of figure 6.3 and the gold standard Maze-III procedure (figure 6.2(A)) are summarized for comparison in table 6.2 and ordered by decreasing values of the percentage of successful termination. Four groups can be distinguished: (1) a group with a success rate of 100%, (2) a group with a success rate from 80% to 95%, (3) a group with a success rate from 60% to 65%, and (4) a group with a success rate from 20% to 25%. The more complex the ablation patterns, the lower the TAFT values. It should be noted that there is a large standard deviation in TAFT values for all ablation patterns. The best result with the shortest TAFT is obtained by the standard Maze-III procedure.

The corresponding distributions of ABBI are shown in figure 6.12. ABBI values ranged between 70 ms (in dark grey) and 140 ms (in light grey) corresponding to frequencies of

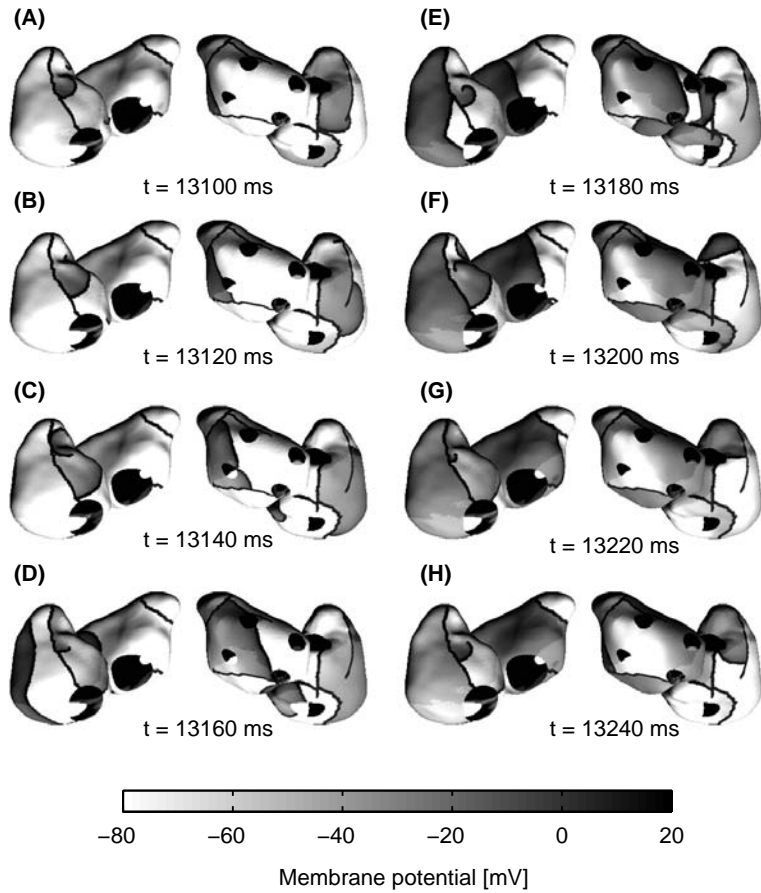


Figure 6.11 – RID-Maze: Uncommon flutter around left appendage. (ablation lines are dark marked and wave front are in gray color level.):

14.3 Hz and 7.1 Hz, respectively. The ablation patterns with a minimum number of lines led to low values of ABBI, indicating no decrease in the rate of AF. The ablation patterns isolating the pulmonary veins (figure 6.12(H–K)) led to a higher left atrial ABBI (> 100 ms) indicating longer intervals between activations. Only the standard Maze-III procedure resulted in a high ABBI in both atria (figure 6.10(A)).

As expected, the ablation pattern with only a 1 cm right isthmus line (IO in figure 6.12(A)) was the least efficient, with a success rate of 20% and many wavelets still present on both atria after ablation. This limited pattern, originally intended to cure atrial flutter [143], has very little effect on the more complex dynamics of AF. This may be observed in the distribution of ABBI with low values ranging from 80 to 90 ms (figure 6.12(A)) indicating the absence of slowing down in atrial activity. The second least effective pattern is the one with an ablation line between both venae cavae (SIVC in figure 6.12(B)). This pattern is not commonly used in clinical interventions but is presented here as part of a systematic study. It led to a success rate of 25% and a distribution of ABBI slightly different from the previous pattern, namely with ABBI values lower than 80 ms in the region

Patterns	Mean TAFT	Suc.Termination
Maze-III	1.3 ± 0.8 s	100.0%
PV+IO+SIVC (K)	6.0 ± 5.0 s	100.0%
LL+SIVC (F)	7.0 ± 5.4 s	100.0%
LL+IO+SIVC (G)	9.8 ± 6.6 s	100.0%
PV+IO (I)	7.8 ± 7.2 s	95.0%
LL+IO (E)	8.8 ± 5.4 s	90.0%
PV+SIVC (J)	10.1 ± 4.5 s	80.0%
PV (H)	15.8 ± 9.8 s	65.0%
LL (D)	11.9 ± 8.5 s	60.0%
IO+SIVC (C)	16.3 ± 8.8 s	60.0%
SIVC (B)	15.1 ± 11.6 s	25.0%
IO (A)	16.2 ± 3.4 s	20.0%

Table 6.2 – Mean TAFT for the simpler patterns.

around the pulmonary veins and the right atrial free wall (figure 6.12(B)). If the simplified IO and SIVC patterns, leading to a very low success rate, were excluded, three groups could be identified in the results obtained with the biophysical model (6.2). The first group has a success rate ranging from 60 to 65% and implies ablation patterns with lines only in the right or only in the left atrium. The first pattern in this group is a combination of IO+SIVC with a total ablation length of 4.5 cm (figure 6.12(C)). Interestingly, this pattern involving right atrial lines only significantly modified the distribution of ABBI in the left atrium with values > 120 ms indicating slower activity (figure 6.12(C)). This type of pattern has been tested in a clinical study by Garg et al. [141] to determine whether lesions could be applied only in the right atrium to suppress the risk associated with catheter ablation in the left atrium. They reported that AF was suppressed in the long-term in 67% of the patients following right atrial compartmentalization, which may be compared to the 60% obtained with the biophysical model. Only two other patterns implying lines in the left atrium led to similar results in terms of success rate and ABBI distribution: the LL pattern (figure 6.12(D)) with a total ablation length of 7.5 cm, and the PV pattern with a full isolation of the pulmonary veins (figure 6.12(H)). These patterns led to a success rate of 60% and 65% respectively. The isolation of the pulmonary veins did not affect the success rate considerably, whereas some differences in the ABBI values in the left atrium could be observed (> 130 ms for the PV pattern and < 120 ms for the LL pattern). The success rate obtained with the biophysical model for these patterns is somewhat in contradiction with clinical experiments of ablation in the region of the pulmonary veins reporting a long-term success rate of 82% [142] This difference may be partly explained by the fact that the AF

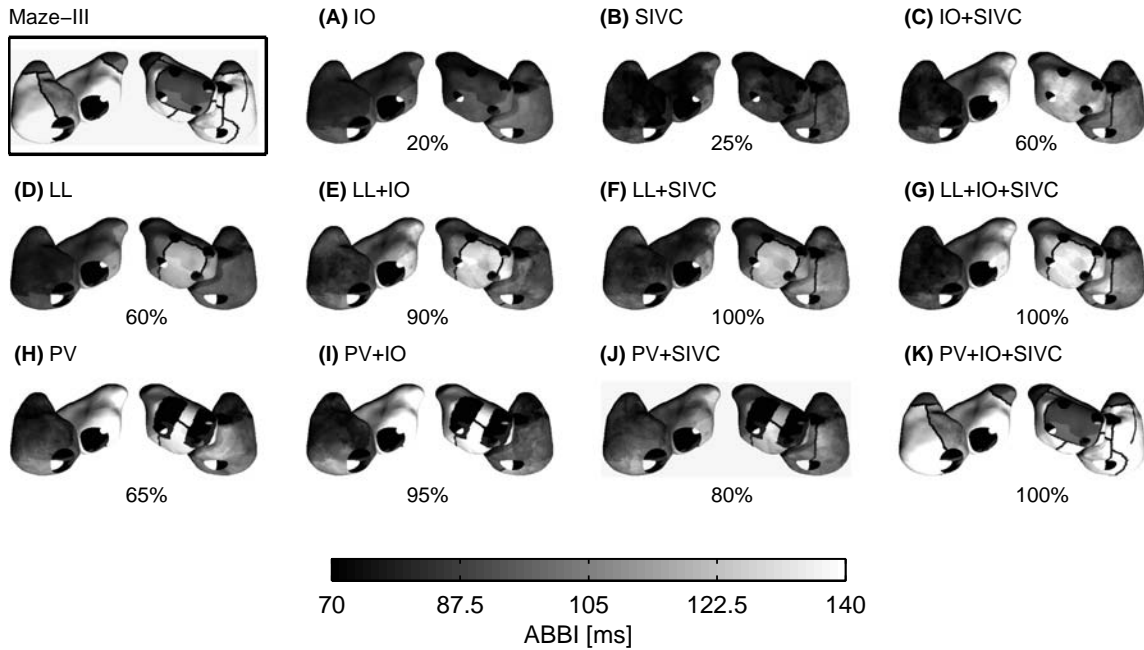


Figure 6.12 – Percentage of success rate and distributions of the average beat-to-beat intervals (ABBI) for each of the 11 simpler ablation patterns studied (ablation lines and isolated regions are resented in white): (A). Isthmus only, IO. (B). Sup./Inf. vena cava line, SIVC. (C). IO and SIVC, IO+SIVC. (D). Left line only, LL. (E). Left line and Isthmus, LL+IO. (F). Left line and Sup./Inf. vena cava line, LL+SIVC (G). Left line, Isthmus and Sup./Inf. vena cava line, LL+IO+SIVC. (H). Pulmonary ablation lines, PV. (I). PV and IO, PV+IO. (J). PV and SIVC, PV+SIVC. (K). PV, IO and SIVC, PV+IO+SIVC. (L). Cox’s Maze-III, Maze-III.

model is based on multiple reentrant wavelets (similar to a permanent AF in the clinical setting implying a diseased atrial tissue), which is very different to the focal AF due to ectopic beats (atrial foci) generally located in the pulmonary veins and acting as triggers for AF [72] (and closer of a paroxysmal form of AF in the clinical setting with a surrounding healthy atrial tissue). The results obtained in the first group of ablation patterns confirmed the fact that lines in the right or in the left atrium only are not sufficient to isolate all multi-wavelet reentries. Notice that ablation lines in the right atrium could impact the ABBI distribution in the left atrium, while on the other hand left lines had little effect on wavelet reentry in the right atrium. A second group was identified with a success rate ranging from 80 to 95%. All patterns in this group are based on the LL or the PV pattern with one ablation line added in the right atrium (the IO or the SIVC line). The addition of the SIVC line to the PV pattern (figure 6.12(J)) increased the success rate from 65% to 80%, while the addition of the IO line to the same PV pattern (figure 6.12(I)) increased the success rate from 65% to 95%. Similarly, by adding the IO line to the LL pattern (figure 6.12(E)), the success rate increased from 60% to 90%. However, for all 3 patterns in this group, the ABBI distribution showed no significant reduction of the activity in the right atrium. The third group of ablation patterns shows a success rate comparable to the Maze-III proce-

ture. The best approaches are the LL pattern with an SIVC line (figure 6.12(F)) and the LL or PV patterns with both an IO and an SIVC line (figure 6.12(G),(K)). They both lead to a 100% success rate. Interestingly, for all these successful patterns, the ABBI values were lower in the right atrium as compared to the Maze-III, suggesting the persistence of residual wavelets and reentries not affecting termination. The easiest pattern to implement and, furthermore, with the shortest total ablation length is the LL+SIVC pattern.

However, as mentioned earlier, our model does not take into account focal AF with triggers in the pulmonary veins. Therefore in clinical experiments, patterns without full isolation of the pulmonary veins could lead to worse results.

6.7.3 Imperfect Maze-III procedure

The results of simulations of discontinuities in the Maze-III are listed in table 6.3. The success rates obtained with the gap in the ablation line between the upper pulmonary veins (Gap II in figure 6.7) are similar to those of the Maze-III (100%). The activation maps showed that wavelets passing through this gap were blocked later by the other ablation lines connecting the four pulmonary veins. Therefore, the position or size of this gap was not critical for the success of AF termination and the means TAFTs were similar. With the gap between the pulmonary veins and mitral valve annulus (Gap I in figure 6.7) the success rates were affected by both width and location. The effect of the gap location was a decrease in success rate as the gap was moved towards the mitral annulus. Furthermore, the wider the gap (except for a gap value of 1.3 mm which had no effect), the lower the

	Position Gap I			Position Gap II		
	Mean TAFT	Suc. Term.	MV Flutter	Mean TAFT	Suc. Term.	AF
Gap widths at the middle position						
1.3 mm	1.4 ± 0.8 s	100.0%	0.0%	1.4 0.6 s	100.0%	0.0%
1.7 mm	1.4 ± 0.9 s	89.0%	11.0%	1.4 0.9 s	100.0%	0.0%
2.4 mm	1.4 ± 0.8 s	82.2%	17.8%	1.4 0.8 s	100.0%	0.0%
3.0 mm	1.4 ± 0.8 s	79.7%	20.3%	1.4 0.7 s	100.0%	0.0%
Gap positions with 3 mm width						
Up/Left	1.4 ± 0.8 s	79.7%	20.3%	1.4 0.7 s	100.0%	0.0%
Middle	1.4 ± 0.9 s	79.7%	20.3%	1.4 0.7 s	100.0%	0.0%
Down/Right	1.3 ± 0.7 s	72.0%	28.0%	1.4 0.7 s	100.0%	0.0%

Table 6.3 – Effect of discontinuities in the Maze-III: mean TAFT and percentage of successful termination.

termination rate. In both cases the decrease of the success rate was linked to the presence of an uncommon flutter around the mitral valve. Figure 6.13 shows this phenomenon as observed by means of the biophysical model.

The results show that a gap, whatever its size or location placed between the upper pulmonary veins, has no effect on the success rate (Gap II in table 6.3). When the mechanism of AF is self-perpetuation based on multiple reentries, only three lines out of four are needed for the pulmonary vein connections. This phenomenon is confirmed by the high success rate observed in simulations with patterns LL+SIVC and LL+IO+SIVC (figure 6.12(F),(G)) which include only three lines (without gap) between the pulmonary veins. By looking at the activation maps, some observable wavelets still passing through this gap were further blocked by ablation lines. On the other hand, a gap positioned along the ablation line connecting the pulmonary veins and the mitral annulus (Gap I in table 6.3) can significantly decrease the success rate due to a flutter around the mitral valve (a phenomenon already clinically observed [55]). This decrease in success rate is more important for gaps close to the mitral annulus since the presence of flutter is facilitated. Success rate also

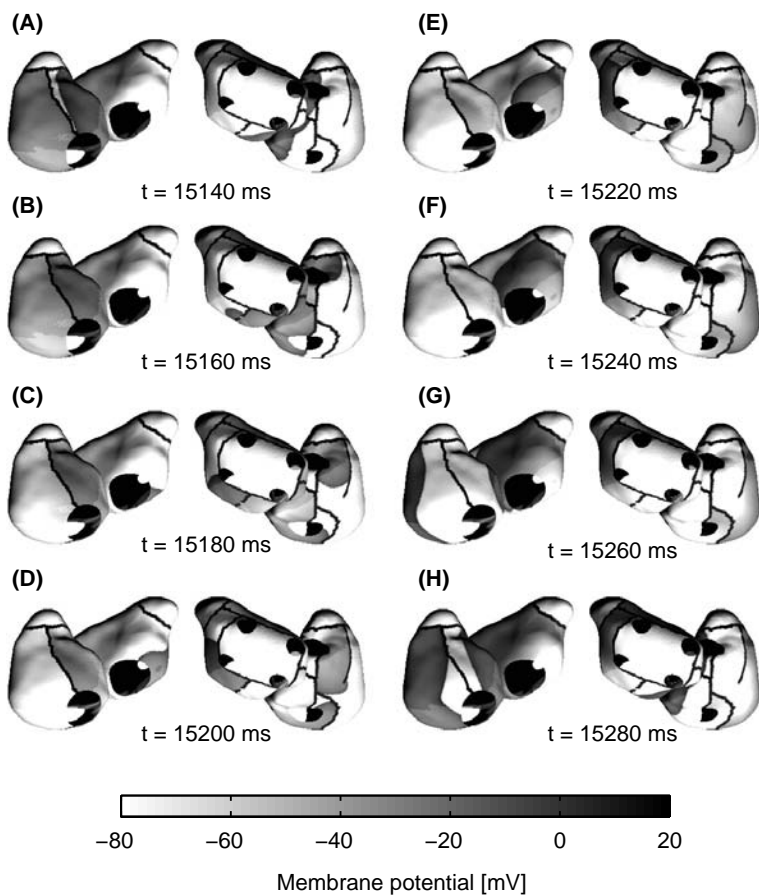


Figure 6.13 – Uncommon flutter around mitral valve. (ablation lines are dark marked and wave front are in gray color level.):

decreased as the gap width was increased from 1.7 to 3 mm. This suggests that for small gaps, conduction blocks may occur, therefore preserving the effect of the ablation line. If no conduction block is associated with the gap, atrial flutter will occur. Mapping studies in animals indicate that gaps smaller than 5 mm in ablation lines may result in conduction blocks [144].

6.7.4 Isolation of pulmonary veins

The results of PVs isolations are listed in table 6.4. The excluded surface around PVs with radius of 10 mm showed higher sinus rhythm (SR) conversion as expected. However, a higher rate of AFL was obtained with 7.5 mm.

The patterns using combined two by two PVs and linear lines obtained significantly higher success rates (90%) if they were combined with the roof and lateral line. For the roof and left isthmus lines combined with PV isolation, the success rate is also given for incomplete ablation lines with a gap (W.G).

6.7.5 Comparison of simulations with clinical data

Results obtained with the Mini-Maze for both the biophysical model and the clinical experiments are summarized in table 6.5. For Group II (with perfect ablation lines in the biophysical model and both endo- and epicardial RF ablation in the clinic) the percentage

PVI	SR (W.G)	AF (W.G)	AFL (W.G)
Exclude surface around the PVs			
5 mm	10%	85%	5%
7.5 mm	25%	50%	25%
10 mm	60%	30%	10%
Combined 2x2 PVs			
5 mm	55%	25%	20%
2.5 mm	30%	45%	25%
0 mm	65%	30%	5%
Combined 2x2 PVs + Linear Lines			
Roof	40% (10%)	55% (60%)	5% (30%)
Lateral	40% (25%)	20% (30%)	40% (45%)
Roof+Lateral	90%	10%	0%

Table 6.4 – *Pulmonary veins isolations. Simulations performed with a gap are denoted with W.G.*

Mini-Maze patterns	SR clinical/computer	AF clinical/computer	AFL clinical/computer	p clinical/computer
Group I	12(60%) / 13(65%)	4(20%) / 2(10%)	4(20%) / 5(25%)	0.66
Group II	24(92%) / 23(88%)	2(8%) / 3(12%)	0(0%) / 0(0%)	0.64

Table 6.5 – Comparison between clinical data and biophysical simulations.

of conversion to sinus rhythm was 88% (with simulations) and 92% (clinical data), which was slightly lower than for the complete Maze-III. For Group I (with a discontinuous ablation line in the biophysical model and only an endocardial RF ablation in the clinic) this percentage was found to be decreased and atypical left atrial flutter was observed both in the biophysical model and in patients. No significant difference was observed between the clinical data and the computer results. Figure 6.10(E) represents the corresponding ABBI distribution for the Group II. When compared to the full Maze-III, the Mini-Maze procedure, despite right atrial appendage removal, leads to ABBI values close to 80 ms in the right atrium, meaning persistent wavelet activity. The ABBI distribution was very similar to those obtained with the other ablation patterns also implying an isolation of the pulmonary veins (figure 6.12(H)-(K)).

The clinical results show that Group I patients have a significantly lower success rate (60%) compared to the Group II patients (92%), highlighting the importance of transmural ablation pattern. These data, as well as the presence of left atrial flutter for Group I patients, are confirmed by our biophysical model, and no significant statistical difference was observed between clinical and computer data using a Fisher’s exact test.

6.7.6 Proposition of an ideal ablation pattern

Table 6.6 summarizes the result obtained with the progressive modified Maze III procedure and for 40 simulations per pattern with different initial conditions. The most efficient were MMP5, MMP6 and Maze III with a 100% success rate. The main difference was expressed in decreasing mean TAFT with a correlation coefficient $R = -0.8$. Note the inflexion point at 100% success rate and a TAFT value of 7.5 s (MMP5), signifying that no additional lines were mandatory beyond this limit (figure 6.14). For two patterns (MMP1 and MMP2) an uncommon flutter around the mitral valve was observed in 2.5% and 10% of the cases, respectively. For the other patterns, flutters were avoided thanks to the left atrial isthmus (LAI) line.

The result from the biophysical model suggested that Maze-III can be simplified in its right atrial pattern to a single line joining superior to inferior vena cava. This remains to be validated in clinical settings.

Patterns	Suc. Termination	AF	Flutter	TAFT
P1	55.0%	42.5%	2.5%	13.5 ± 7.1 s
P2	65.0%	25.0%	10.0%	13.4 ± 9.4 s
P3	80.0%	20.0%	0.0%	11.6 ± 8.1 s
P4	95.0%	5.0%	0.0%	9.5 ± 7.1 s
P5	100.0%	0.0%	0.0%	7.5 ± 7.6 s
P6	100.0%	0.0%	0.0%	5.1 ± 5.0 s
Maze III	100.0%	0.0%	0.0%	1.3 ± 0.8 s

Table 6.6 – *Statistic for the modified Maze III patterns.*

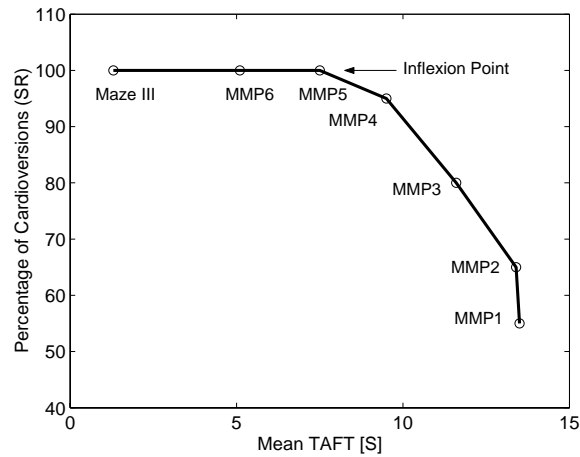


Figure 6.14 – *Percentage of cardioversions vs. TAFT for the modified Maze III patterns.*

6.7.7 Limitations

Even though the results obtained with the atrial model are consistent with clinical observations, some of the limitations should be highlighted. In this study, the number of simulations performed with the standard Maze-III procedure is identical to that of patients in the literature, i.e. 118 patients. However, a direct comparison between computer simulations and clinical data is difficult, since the geometry of the biophysical model was one and the same during the whole experiment, whereas the atrial anatomy differs in each patient. First, in contrast to surgical operations, during computer simulations all elements of the ablation lines were applied instantaneously. Also, when simulating non-transmural ablation lines, one gap of arbitrary width was introduced into a line of the biophysical model, while during clinical endocardial ablation many gaps of unknown size can be present. Moreover the fact that the AF model takes into account reentrant wavelets only and cannot be used in the case of rapid foci, should be highlighted. For instance, if a rapid focus appears in the pulmonary vein region, incomplete ablation lines around pulmonary veins (figure 6.7

Gap II) will not necessarily prevent AF reinitiation. Finally, in order to keep computation time within a tractable range, a simplified atrial model was used. The single layer cell model does not include anisotropic fast-conducting regions, fiber orientation, crista terminalis and pectinate muscles, which may all play a role during AF [17, 145]. A version of the model incorporating some of these aspects has been developed at the expense of an increased complexity and computational load. The inclusion of such details requires validated morphological data.

6.8 Conclusions

This chapter shows how a computer model of human atria can be used to compare existing surgical or RF ablation procedures and to study the effect of imperfect ablation lines. The results of our the simulated ablation lines confirm the high performance of the gold standard Maze-III procedure, and suggest that the development of less invasive patterns needs to include ablation lines in both the right an the left atrium. It has also been observed in the simulations that some lines are more sensitive to imperfections (for example due to non-transmurality of ablation) than others, leading generally to the presence of uncommon atrial flutter after ablation, a phenomenon also observed in the clinic. A comparison of the simulation data with clinical data shows no significant difference in the case of patients suffering from permanent AF.

A new ablation pattern that can be proposed on the basis of the results of these simulation studies is as follow. The Maze-III procedure can be simplified in its right atrial pattern to a single line joining superior to inferior vena cava. This remains to be confirmed clinically.

These results indicate that, through an interaction with clinicians involved in surgical procedures, biophysical models are promising tools for the investigation of patterns.

7

Therapeutic pacing

7.1 Introduction

THE advantages of pacing the heart electrically were well known as far back as the early 1900s [146, 147]. Current permanent pacemakers consist of a source of electrical current that is linked to the cardiac muscle by a wire (lead) and controlled by an integrated circuit. If the sinoatrial node does not generate intrinsic electrical impulses in a regular manner, the pacemaker sends an electrical current down the lead to stimulate the heart. The current depolarizes the cardiac cells at the tip of the lead, and this depolarization propagates across the myocardium in a normal fashion.

Early pacemakers were large, bulky external devices that used vacuum tubes, powered by an external AC current source. External electric stimuli were frequently too traumatic for patients, and the AC-operated pacemaker could fail during a power blackout. Rune Elmqvist developed the first implantable pacemaker at the prompting of Dr. Ake Senning, a surgeon at the Karolinska Institute in Stockholm, in 1958.

At present, various types of sophisticated pacemakers are currently on the market: single-chamber or multi-chamber pacemakers. Pacemakers that synchronize both the atria and ventricles are called dual-chamber pacemakers. Some pacemakers use adaptable pacing algorithms such as burst or ramp pacing to terminate atrial or ventricular arrhythmias [148, 149].

Pacemakers are inserted for a variety of heart conditions including sick sinus syndrome, supraventricular bradycardia, heart block and ventricular bradycardia. The pacemakers are individually programmed to maintain the patient's natural, intrinsic heart rhythm, which usually falls between 50 and 70 beats per minutes. On the other hand, during ventricular

tachycardia or fibrillation, an implantable *defibrillator* is adopted. The defibrillators use one or more of three basic modes of operation [150]: *low-energy* (0.5 to 2 Joules) cardioversion, *defibrillation*¹ (~ 30 Joules) and *antitachycardia pacing* (ATP). Most devices in use today employ high-energy defibrillation for ventricular tachycardia. This short-circuits the rapid ventricular rhythms by sending at a pace faster than the already accelerated ventricular rate. The aim is to depolarize the heart muscle at the right moment, interrupting the abnormal rhythm and thereby halting the tachycardia. The main motivation to develop ATP of atrial fibrillation (AF) is the fact that pacing is below the threshold of pain compared to defibrillation. Other advantages of using ATP are: reversible impact (when compared to ablation procedures) and better tolerance (when compared to medication).

These days, interest in AF therapies has considerably increased. It is well known that atrial flutter (AFL) can be terminated by pacing [151]. However, no pacing therapy has yet proved to be effective in AF termination, probably due to its complex dynamics, the variable number of wavelets, and the shorter and variable *excitable gap*² during AF. Mitchell *et al.* showed that ATP treatments (50 Hz burst pacing of 2 seconds duration) are ineffective in terminating persistent atrial fibrillation in humans [152].

However, the possibility of local atrial *capture*³ has been demonstrated in animal and human experiments, both in electrically induced and spontaneous AF. Alessie *et al.* showed for electrically induced AF in dogs that it is possible to capture a region of atrial tissue with a diameter of about 6 cm by rapid pacing [153]. The rate of the paced atria is faster than the original rate but does not lead to termination, due sometimes to a loss of capture. Daoud *et al.* performed pacing in a human right atrium during electrically induced type I AF (pacing with a cycle length 10-50 ms less than the mean atrial cycle length up to 110 ms) [154]. Local capture and distant effects in the left atrium could be observed but not termination. Pandozi *et al.* assessed the possibility of local capture in patients with spontaneous chronic atrial fibrillation (pacing with cycle length of 250 ms, decreased by 10 ms every 10 ms down to a cycle length of 100 ms) [155]. Local capture was obtained in 87.2% of the pacing sites, with a preference for the lateral wall over the atrial roof or the septum.

Most techniques pace at a single site, leading to a region of capture with a diameter of approximately 4-6 cm (generally in the right atrium). It has been suggested that multi-site pacing could be more efficient in capturing both atria [156]. Pacing could then be stopped when atrial activation becomes organized on the whole surface, leading to termination. The main problem is how to optimize this therapeutic pacing system and synchronize the different pacing sites.

Since no optimal solutions come out of clinical and experimental experience, simulations

¹Defibrillation is the use of an electric shock, administered either through a device on the exterior of the chest wall or directly to the exposed heart muscle, to restart or normalize heart rhythms.

²The excitable gap is a short period within the cycle of the atrioventricular or intraventricular conduction allowing the passage of an impulse, which at other times would be blocked in transit.

³The capture is a region of the tissue where no reentries are present and the only possible wavefronts are generated by the stimulation of the pacemaker.

are proposed as an alternative to explore atrial therapies by electrical stimulations. In this study, a biophysical model of the human atria is used to investigate ATP during atrial arrhythmia. It aims at helping electrophysiologists to optimize the following parameters:

- position and number of electrodes needed for sensing atrial activity;
- position and number of electrodes needed for pacing;
- pacing frequencies and amplitudes;
- determination of variables (reflecting atrial activation in the tissue such as excitable gap, degree of organization) that can be used to control pacing;
- sequence and timing for multi-site pacing.

This chapter presents preliminary results on these topics. First, section 7.2 presents an algorithm for pacing and the different pacing sites that have been investigated during this research. Second, section 7.3 shows why atrial flutter can be pace-terminated more easily than AF. Finally, section 7.4 presents antitachypacing strategies on the different types of AF previously presented in chapter 3. To quantify the efficiency of the ATP procedure, the methods presented in chapter 4 are used to measure the degree of organization.

7.2 Pacing methods

7.2.1 Introduction

Pacing can be used to *control*¹ a tissue region during arrhythmia. The main problem is to find the time instant at which the tissue is in its resting state (*i.e.* the excitable gap) to ensure that the stimulus applied propagates through the tissue. The stimulus should be delivered late enough to avoid the effective refractory period (ERP) of the tissue but early enough to stay away from “encroachment” of an external wavefront, resulting from a distant reentry or spiral generated by a mother rotor². Figure 7.1 presents the time course of the membrane potential of a node on the surface of the atria and the electrogram signal computed at the same site during sustained AF. The highlighted time instants (in dark) represent the instants at which the tissue is in its resting state ($V_m \leq 75$ mV). Depending on the type of AF, the excitable gap ranges from 70 ms to 180 ms.

7.2.2 Pacing algorithms

State-of-the-art

When applying ATP, the optimal pacing frequency can be determined by different methods. Early approaches performed by Alessie *et al.* [153] were experimented on animals. They

¹A region under control by pacing is an area where no reentries are present and only wavefronts are generated by the stimulation of the pacemaker.

²A mother rotor is a stable source of reentry that generates multiple wavelet breaks

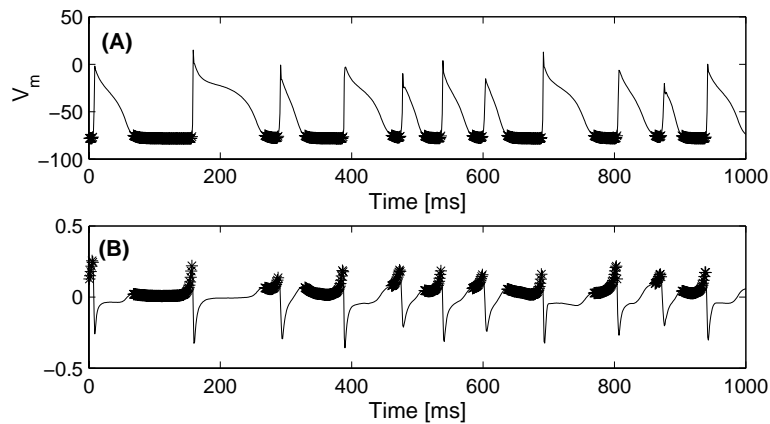


Figure 7.1 – *Excitable gap (in dark)*. Example of simulation using the chronic AF model. (A) Transmembrane potential. (B) Electrogram signal.

used pacing intervals 10 ms shorter than the local median fibrillation interval, subsequently shortened by steps of 1 ms. In 1997, Pandozi and co-workers [155] demonstrated that local capture by atrial pacing was possible in human atria. They used decremental pacing starting from the average AF cycle length. These procedures are usually performed in an open-loop fashion. Their main disadvantage compared to a closed-loop method, is that stimuli are always generated independently of the state of the tissue. In a closed-loop system, stimuli are delivered only if a wavefront is not present under the pacing electrode, avoiding the application of an ineffective stimulus. In pacing devices, the term closed-loop refers to a pacing system, which takes into account the *return cycle length*¹ [157]. In the present study, the term closed-loop is used in the general sense.

In 2000, Ditto and colleagues chose an interesting chaos control approach to determine the pacing frequency [158]. Their results presented on the application and evaluation of chaos control for slowing and regularizing local electrical activation of the right atrium of humans during induced AF. In the technical literature, the term chaos refers to a process that appears to be random and disordered but is in fact of a deterministic nature. The basic idea is the following: the dynamics of a chaotic process in the state space can be characterized by unstable fixed points (UFP). In the vicinity of an UFP, there are regions of space in which the point is attracting (stable manifold), and others where it is repulsive (unstable manifold). The aim of chaos control is to apply a small perturbation to the system evolving on an unstable manifold and to bring it to a stable one [159]. In the case of ATP pacing, the UFP was determined using the beat-to-beat interval (BBI) histogram. This method [158] consisted of constructing a Poincaré map [160], in which the n^{th} interbeat interval (I_n) was plotted against the previous interval (I_{n-1}). Then, during a learning phase, the unstable fixed points were identified on the Poincaré map. Finally, the intervention phase consisted in applying precisely-timed stimuli to place the next Poincaré map point

¹The return cycle length is the time period between the last pulse of an ATP and the first spontaneous depolarization detected post-ATP.

onto the stable manifold of the identified fixed point [161].

In 2000, Peterson and Link [162] have suggested a schema patent for pacing based on monophasic action potential (MAP) recordings, this consists of obtaining a signal corresponding to the action potential of a tissue patch. The stimulus is delivered during the repolarization phase of the tissue, just after the effective refractory period (ERP). The difficulty in this method resides in the MAP recordings, which is still not possible with a pacemaker as well as the detection of ERPs.

Development of pacing algorithms in the biophysical model

In the present study, four different procedures were implemented and evaluated with the biophysical model:

1. open-loop pacing at a constant frequency;
2. open-loop pacing with a ramp protocol;
3. closed-loop pacing with rate adaptation;
4. closed-loop pacing with rate adaptation and a ramp protocol.

The first algorithm paces at a constant frequency over time. This frequency was determined from the BBI histogram. The second algorithm uses a ramp protocol. The initial frequency is incremented or decremented between each stimulation pacing. These two algorithms are similar to the one Alessie *et al.* [153] used and belongs of course to the category of open-loop algorithms.

Based on the Peterson's patent closed-loop algorithm [162], the two last algorithms (algorithm 3 and 4) were developed. Instead of using the MAP recordings and detecting the ERP phase repolarization, which is not always an easy task in an electronic device, the upstroke phase (section 2.2, figure 2.2) of the depolarization was used. The detection of the upstroke is easier because of the fast and large variations of the transmembrane potential. The upstroke phase can be detected in two different manners by the MAP recordings or by the electrogram signals. The upstroke is represented by a fast variation from a positive peak to a negative peak value in the electrogram signal (figure 7.1(B)). In the biophysical model, the MAP signals were used to detect the upstroke to save computation time and to avoid having to compute the electrogram signals during simulations.

The schemes of algorithm 3 and 4 are presented simultaneously in figure 7.2. The presence of the ramp protocol differentiates algorithm 3 and 4. Two parameters are involved in algorithm 4: 1) the waiting time τ and 2) the increment (*underdrive pacing*) or decrement (*overdrive pacing*) of the waiting time value τ . The initial value of τ is taken to be the median value of the BBIs histogram.

The main difference between the two first algorithms and the two last ones is the closed-loop protocol. Since in an open-loop pacing method, the pacing is delivered at a constant

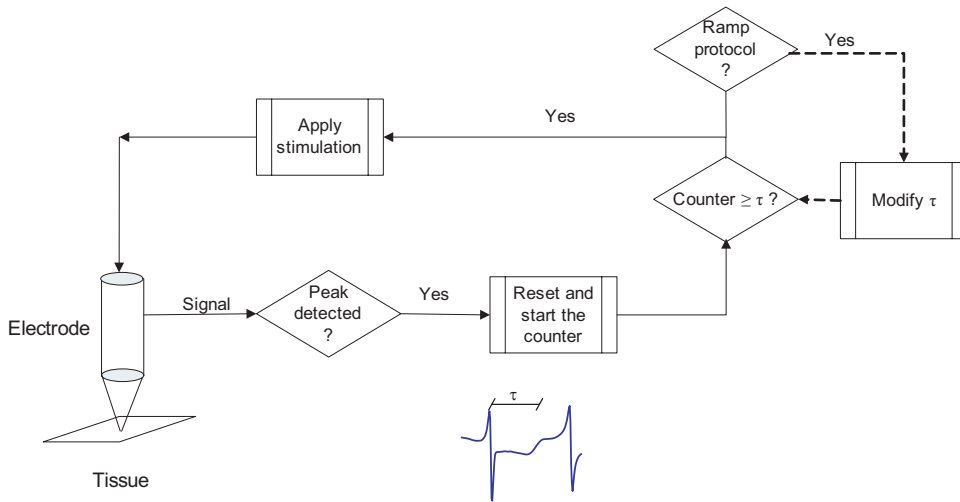


Figure 7.2 – Flow chart of the closed-loop pacing algorithm (3 and 4) and an electrogram signal with the waiting time τ is also presented. If a ramp protocol is used (algorithm 4, in dashed line), this parameter can be incremented (underdrive pacing) or decremented (overdrive pacing).

frequency, a stimulus could be generated even during the resting period of the tissue. But this stimulus cannot induce a wavefront propagation. In a closed-loop pacing method, if a wavefront is detected during the waiting time τ , no stimulus is delivered (figure 7.2). Another advantage of a closed-loop system is that less stimuli are delivered, so saving pacemaker batteries.

As results obtained were quite similar with open- or closed- loop algorithms, only results with the algorithms 3 and 4 are presented in this study. Using open-loop algorithms, the time to reach the control of a region is longer due to the ineffectiveness of some stimuli, which were delivered during the effective refractory period.

7.2.3 Pacing rates and pacing sites

This section deals with the initial value of the waiting time τ previously described, as well as the different sites of pacing investigated during this study.

A priori, any pacing frequency value is possible for the waiting time τ . Since there is an excitable gap between two successive beats, the choice of the pacing frequency is determined by the BBIs histogram computed at the pacing site. Since the pacing frequency is the number of complete cycles over a period of time, it is obtained by taking the reciprocal value of BBI value.

Figure 7.3 presents the BBI histograms of three different types of simulated AF: chronic AF, meandering AF and cholinergic AF. The BBIs distribution varies considerably depending on the type of AF. In chronic AF, the BBI shows a large dispersion compared to the meandering and cholinergic AF. Meandering AF and cholinergic AF demonstrate a single mode around 250 ms and 80 ms, respectively. In this study, the median value of the BBI

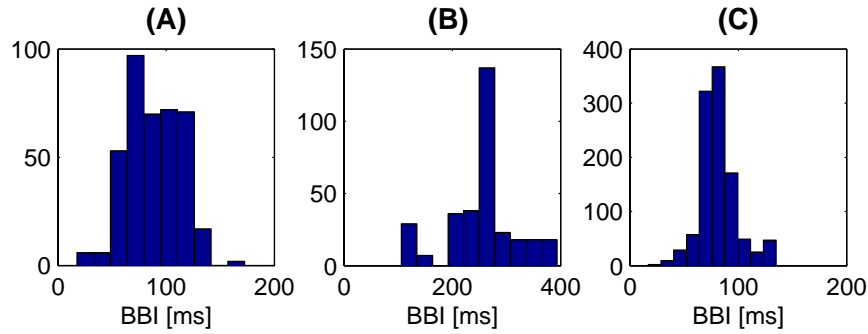


Figure 7.3 – Examples of BBIs histogram computed in the middle of the right atrium free wall. (A) Chronic AF: min. value = 17.6 ms, max. value = 172.5 ms, mean value = 87.9 ms and median value = 80.8 ms. (B) Meandering AF: min value = 106.0 ms, max. value = 394.4 ms, mean value = 255.4 ms and median value = 263.6 ms. (C) Cholinergic AF: min value = 33.4 ms, max. value = 135.0 ms, mean value = 81.5 ms and median value = 80.1 ms.

histogram was chosen for the initial value of the waiting time τ . This insures that a stimulus can always be generated and propagated. If the minimum value is chosen and overdrive pacing is applied, wavefronts cannot be generated. When decreasing τ , stimuli are applied during the refractory period of the tissue. If the maximum value of the BBI histogram is chosen as the initial τ value, meaning that the initial pacing frequency is low, only overdrive pacing can be used to ensure stimuli to be delivered during the excitable gap. Also, the probability of having a wavefront under the pacing site is high.

Note that in current pacing devices, pacing algorithms are applied depending on the beat-to-beat interval of the last 5 to 10 beats. Furthermore, during pacing, a ramp protocol or a burst can be applied.

Figure 7.4 presents the different pacing sites (S_1 - S_6) investigated in this research. The pacing algorithms (3 and 4) are used for single site pacing as well as for multi-site pacing. E denotes the position of the computed electrogram signal used to observe organization during AF pacing. It is located at 2.25 cm from S_1 .

Pacing is initiated by injecting intracellular current ($I_{stim} = 80 \mu\text{A}/\text{cm}^2$) in a small region of approximately 3 mm^2 during 2 ms.

7.2.4 Evaluation of pacing efficiency

To follow the evolution of the spatio-temporal complexity during ATP of different types of AF (chronic, meandering and cholinergic), the methods described in chapter 4 are used: high density mapping and multidimensional electrogram signal analysis. The signal duration used to compute the spatial correlation with the high density mapping system is 1 s. In order to observe the global organization of both atria, the spatial multidimensional signal analysis with a split level 6 (32 electrodes per atrium, placed at equal distances, see section 4.2.3) is used with a moving time window of 1 s and an overlap of 0.5 s.

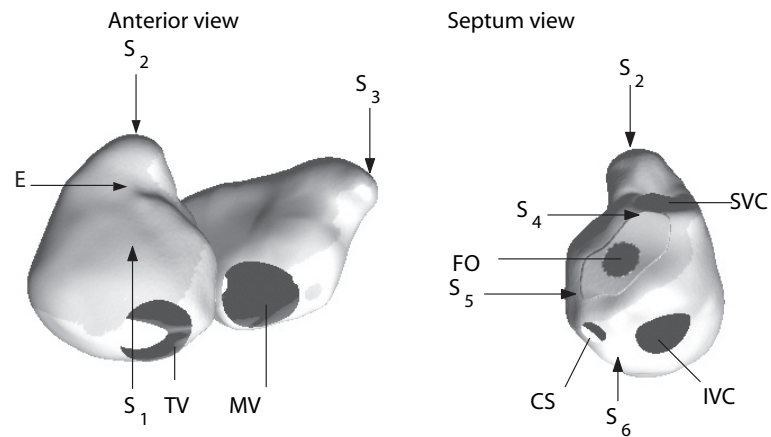


Figure 7.4 – *Pacing sites.* The different pacing sites experimented are indicated: S_1, S_2, S_3, S_4, S_5 and S_6 . E is the position used to compute an electrogram signal. The major vessels and valves are included: tricuspid valve (TV), mitral valve (MV), superior vena cava (SVC), inferior vena cava (IVC), coronary sinus (CS) and fossa ovalis (FO).

The next two sections present results of ATP, using algorithm 3 and 4, applied to different types of atrial arrhythmias simulated (see chapter 3) with the biophysical model of the human atria. First, ATP is used on atrial flutters simulated on the 3D homogeneous monolayer and the 3D inhomogeneous multilayer model. These experiments aim at confirming clinical results. Second, ATP is investigated for different types of AFs: chronic AF, meandering AF and cholinergic AF. These results are compared with that of ongoing clinical research.

7.3 Pacing atrial flutter

Since the biophysical model can reproduce AFLs in the 3D homogeneous monolayer (section 3.2.1) and in the 3D inhomogeneous 3D multilayered model (section 3.2.2), ATP is applied to these two different cases. Usually, in clinical practice, the pacing electrode is placed in the right atrium appendage (RAA). In the biophysical model, AFL pacing is evaluated at two different sites: the isthmus region and the RAA.

7.3.1 Pacing AFL in the 3D homogeneous monolayer model

Section 3.2.1 presented how an atrial flutter can be simulated using the 3D monolayer model. This kind of flutter presents overly rapid contractions of the atria at a rate of 400 bpm (beat per minute). By pacing in the isthmus region (figure 7.4, site S_6) with an initial waiting time τ set to the median value of the BBI, it was possible to pace-terminate the flutter using an increasing or decreasing ramp protocol with a 1 or 2 ms increment or decrement, respectively. The position of the pacing site was chosen in the narrowest region along the pathway of the macro-reentrant circuit. This favored the creation of a block in the opposite direction.

By pacing in the right atrium appendage, as is usually performed in clinical practice, no AFL termination could be achieved. The wavefront generated by the pacing site could not interrupt the AFL circuit. Since the flutter generates a single wavefront and wavetail, the extra wavefront introduced by the pacing site did not affect the circuit. In fact, the stimulus generated two wavefronts: one of them collided with the wavefront of the flutter and the second one generated a new wavefront.

This phenomenon is illustrated in figure 7.5 with an action potential propagating in a 1D ring model. Because of the position chosen, a block in the opposite direction was not observed.

The wavefront was not confined to a region such as the isthmus, but propagated in all directions of the tissue and so regenerated a reentry. The tissue of the monolayer 3D model is homogenous and isotropic, which maintains a stable macro-reentrant circuit. In a configuration in which anisotropy is present, AFL termination could be obtained. This situation is described in the next section.

7.3.2 Pacing AFL in the 3D inhomogeneous multilayer model

In section 3.2.2, it has been shown that atrial flutter in the multilayer 3D model could be initiated by properly timed electrical stimuli. The rate of the simulated AFL was 333 bpm (180 ms of cycle length) on average. This section presents how this AFL can be terminated using rapid pacing or overdrive pacing (at a rate higher than the reentrant process). Two pacing sites were investigated. The first one was located in the isthmus region (figure 7.4, site S_6), since this position corresponds to the narrowest region along the pathway of the macro-reentry, so that it is easy to create a block in the direction opposite to that of the

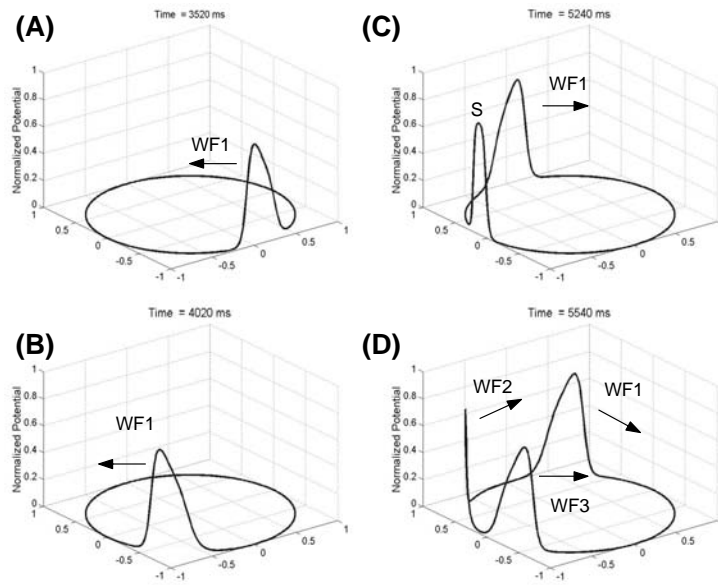


Figure 7.5 – *Unsuccessful termination of AFL pacing. (A)-(B) Single wavefront (WF1) propagating in the clockwise direction. (C) Stimulus (S) applied. (D) Generation of two new wavefronts (WF1 and WF2). WF3 will collapse with WF1 and WF2 will maintain the reentry.*

reentrant circuit. The second position was located in the right atrial appendage (RAA) (figure 7.4, site S_2), which corresponds more with the antitachypacing pacemaker currently used clinically, due to the accessibility of RAA to implement an electrode. As in the previous section, the pacing protocol used a ramp.

Figure 7.6 presents the transmembrane potential distribution map for an example of pacing in the RAA with a decremented ramp of 1 ms (overdrive pacing). The mechanisms involved in this case to pace-terminate the AFL depends on two factors. The first one is the perturbation of the stable rhythm (figure 7.6(A-C)) as shown in figure 7.6(D). The wavefront anchored around the tricuspid valve (TV) was momentary unanchored, which modified the cycle length. The second factor is the wavefront collapsing at the wave tail leading to the annihilation of the circuit (figure 7.6(G-H)).

In addition to these two factors, another factor has been found to be responsible for AFL termination. A reentry situated in the isthmus region (figure 7.7) around the coronary sinus (CS) was present and a new wavefront propagated in a direction opposite to the direction of the macro-reentry of the AFL. The collision of the two wavefronts cancelled both of them and the macro-reentry was destroyed.

When applying pacing in the isthmus region (figure 7.4, site S_6), another phenomenon was generally involved in pace-termination. The wavefront generated by the pacing electrode propagated in two opposite directions, namely the septum and the RAA. The first front collided with the main wavefront of the macro-reentry and collapsed, whereas the second one was blocked by the refractory period of the macro-reentry tail.

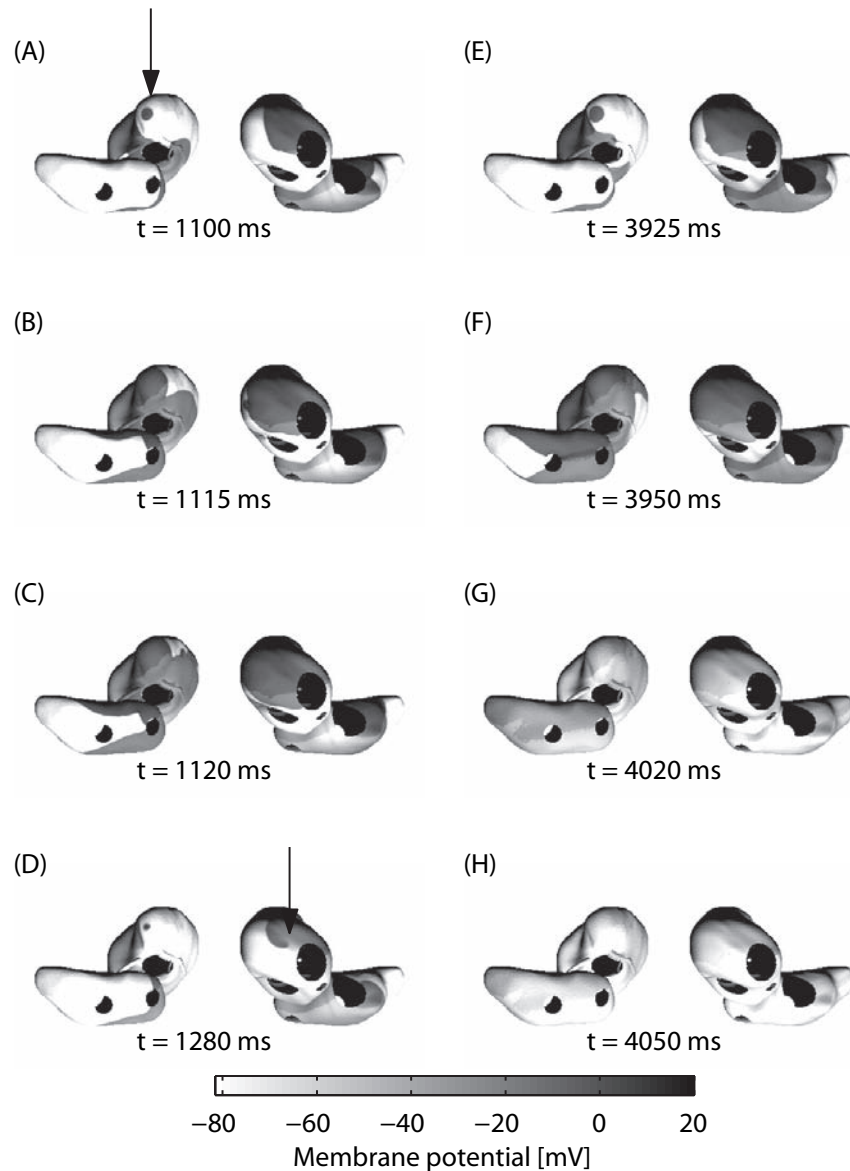


Figure 7.6 – Pacing atrial flutter in the right atrium. Mechanism leading to AFL termination. (A)-(H): TMPDM. (A) Pacing site (indicated by an arrow) in the RAA. (B)-(C) Macro-reentrant around the tricuspid valve (TV). (D) Macro-reentrant circuit modified due to the wavefront (indicated by an arrow) unanchored around the tricuspid valve. (E)-(F) Modification of the macro-reentrant circuit. (G)-(H) Annihilation of the flutter.

These results are in accordance with results published by Sinha *et al.* [163] They demonstrated in a 2D model that under certain conditions, successful termination of arrhythmia requires the presence of inhomogeneous regions. In the present study the isthmus region has a slow conduction velocity compared to the rest of the tissue.

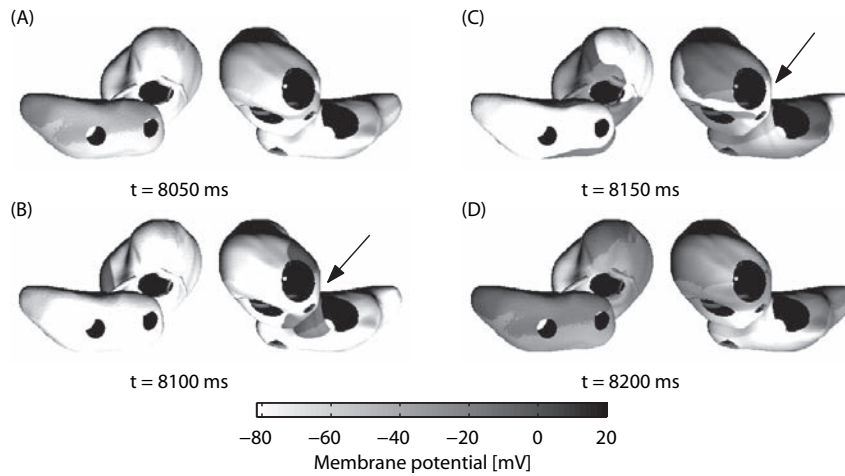


Figure 7.7 – Pacing atrial flutter in the right atrium: reentry in the isthmus region leading to AFL termination (A)-(D): TMPDM. (A) The region between CS and IVC is still in refractory period. (B)-(C) Wavelet anchored around CS. (D) Collision of the macro-reentrant wavefront and the wavefront anchored around CS leading to AFL termination.

7.4 Pacing atrial fibrillation

Electrophysiologists have found that the right anterior atrial free wall is an effective site for pacing, with a largest area of capture during atrial pacing [155]. In the biophysical model, the sensor and stimulation electrodes were placed at the same position, located in the middle of the high density mapping system (figure 4.1 and figure 7.4, site S_1). The antitachypacing method was tested for three different types of AF (see chapter 3): chronic, meandering and cholinergic, and for some other sites as described in figure 7.4. Since during AF, the macrostructure plays a minor role, all the simulations were performed using the monolayer 3D model to save computation time.

7.4.1 Pacing chronic AF

Figure 7.8 presents the evolution of the spatial correlation on the high density mapping during chronic AF pacing in the right atrium free wall (figure 7.4, site S_1). Signal lengths used to compute the spatial correlation were 5 s during sinoatrial rhythm and 1 s during AF. Curves (1) and (2) correspond to the sinoatrial rhythm and chronic AF, respectively. The other intermediate curves show the evolution of the local organization during ATP, after 2 s, 5 s and 10 s. As shown in this figure, after 10 s of pacing, the right anterior atrium free wall was completely under control. The correlation coefficient was close to 1.

To observe the global organization of both atria, the spatial multidimensional signals analysis with a split level 6 (32 electrodes per atrium placed at equal distances, see section 4.2.3) was used on a moving time window of one second with an overlap of 0.5 s. Figure 7.9 shows the time evolution of the two measures of complexity $CEig_{95\%}$ and $CEnt$

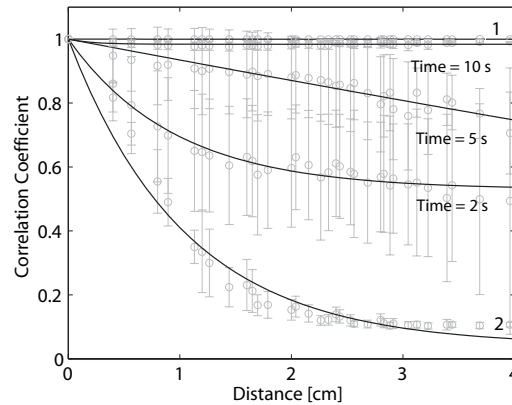


Figure 7.8 – Spatial correlation during pacing of chronic AF. (1) Sinoatrial rhythm. (2) Chronic AF. Evolution of spatial correlation after pacing of 2 s, 5 s and 10 s.

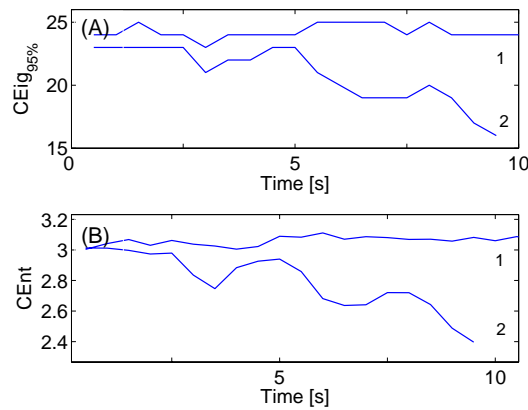


Figure 7.9 – Measure of complexity during pacing of chronic AF. (A) $CEig_{95\%}$. (B) $CEnt$. (1) Chronic AF. (2) Pacing.

(section 4.2.4). During sinoatrial rhythm, $CEig_{95\%}$ and $CEnt$ values were respectively 5 and 1.5 (figure 4.6). As expected, the complexity decreased over time but never reached a value lower than 15 for the $CEig_{95\%}$ and 2.4 for $CEnt$. This means that a residual AF was still present on the left atrium. Even under control, oscillations were observable in curve (2) (figure 7.9(A),(B)), corresponding to an imperfect control and some reentries were present in the controlled area.

Figure 7.10 presents the transmembrane potential distribution map during pacing. The pacing site on the right atrium free wall is indicated by an arrow. At the beginning ($t = 410$ ms) the control was only effective in a small region around the pacing site. After 2 s of pacing the region under control reached a diameter of 4.5 cm. After 10 s, the entire right atrium was under control, and only residual wavelets reentries were present on the left atrium (figure 7.10(F)).

An electrode (figure 7.4(E)) placed at 2.25 cm from the pacing site recorded an electro-

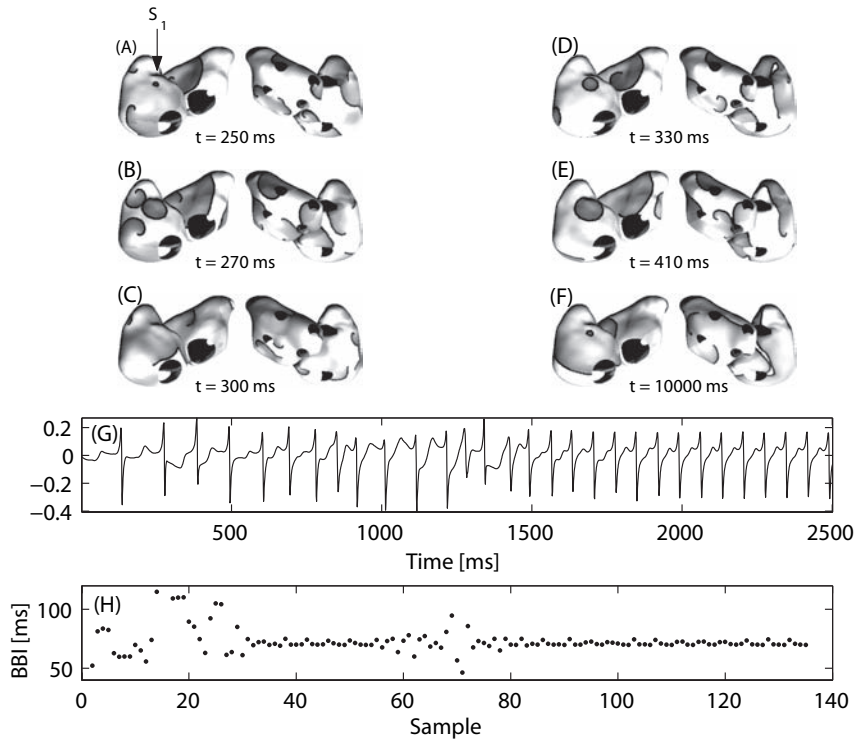


Figure 7.10 – Pacing in the right atrium free wall during chronic AF. (A)-(F) TMPDM. The pacing site is indicated by an arrow. (G) Electrogram signal computed at 2.25 cm from the pacing site (S_1) in the direction of right atrium appendage. (H) Beat-to-beat intervals computed at the same site of the measured electrogram signal.

gram signal (figure 7.10(G)). This one shows irregularities before 1.5 s. After the control became effective, this signal became periodic. The frequency of the electrogram signal followed the pacing rate of the stimulation, that is 13.3 Hz. Figure 7.10(H) presents the BBI computed at the same site as the electrogram signal. During the first 30 samples, the BBIs ranged from 50 to 150 ms. Under control, the BBIs stayed stable around 75 ms, which corresponded to the pacing frequency of 13.3 Hz. Note that a loss of control was detected between the 60th and the 70th sample.

After full control of the right atrium was obtained, a decrement rate of 1 ms was used between each stimulus. By decreasing the pacing rate, the diastolic interval (DI) increased. Since the APD depends on the DI, by decreasing DI, the APD increased according to the restitution curve (section 2.2, figure 3.9). The goal was to modify the tissue properties and guide the atrial rate to sinoatrial rhythm. Figure 7.11 presents the result obtained after decrementing the pacing rate. The position of measurement selected was as used previously. After 2 s, the electrogram signal became irregular (figure 7.11(A)), showing a loss of control and the onset of reentries. Figure 7.11(B) shows the evolution of the BBIs. By decreasing the pacing, the BBIs increased from 70 ms to 100 ms for the first 20 samples. The region was controlled by the pacing rate. After 2 s, the BBIs became irregular and ranged between

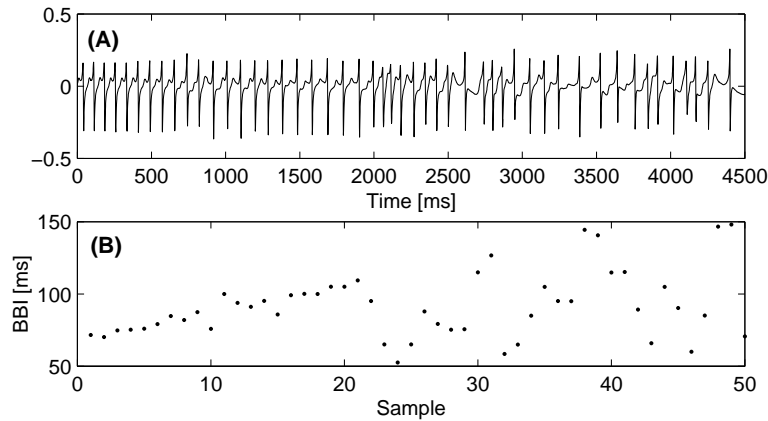


Figure 7.11 – Decrementing the pacing rate after control during chronic AF. (A). Electrogram signal (B). Beat-to-beat intervals.

50 and 150 ms, meaning a loss of control and the onset of reentries.

The other site of pacing was used during ATP (figure 7.4, site S_{2-5}). When pacing in the right or left appendage only (S_{2-3}), similar results were obtained. Only one atrium could be controlled by pacing.

The advantage of pacing in the septum is that both atria could be controlled at the same time [164–166]. The sites (S_4 and S_5) were proposed as pacing sites. The transmembrane potential distribution map during AF pacing at site S_4 is illustrated in figure 7.12. After 10 s of pacing, both atria were under control, and no residual wavelets were present. The only wavefronts were generated by the delivered stimulation. However, the anchored wavefront (indicated in figure 7.12(B) by arrows) was still a factor generating AF, because, when pacing was stopped or the rate of pacing reduced after 10 s, AF was reinitiated.

In contrast to pacing at site S_4 , there was no control when pacing at site S_5 . This is due to several orifices present in this region. Wavefronts generated by the pacing could not propagate over the atria. It was also observed that a wave anchored around the coronary sinus (CS) was present, which prevented the stimulation from propagating.

The results obtained using incremental or decremented pacing during chronic AF were not satisfactory. The action potential duration (APD) of this type of AF was very short with an average cycle length of 89 ms. So by incrementing the pacing rate (overdrive pacing), stimuli were performed during the effective refractory period (ERP) and no wave could be propagated. By decrementing the rate, loss of capture was observed due to the penetration of reentrant wavelets in the region of capture.

As a single site can almost control either the entire right or left atrium, two pacing sites were used to attempt to control both atria. Several combinations of pacing sites were used (figure 7.4). The difficulty when using multi-site pacing was to take into account the local activity under a specific pacing site as well as the wavefront generated by the other site. When considering only the wavefront generated by the other pacing site, the local activity

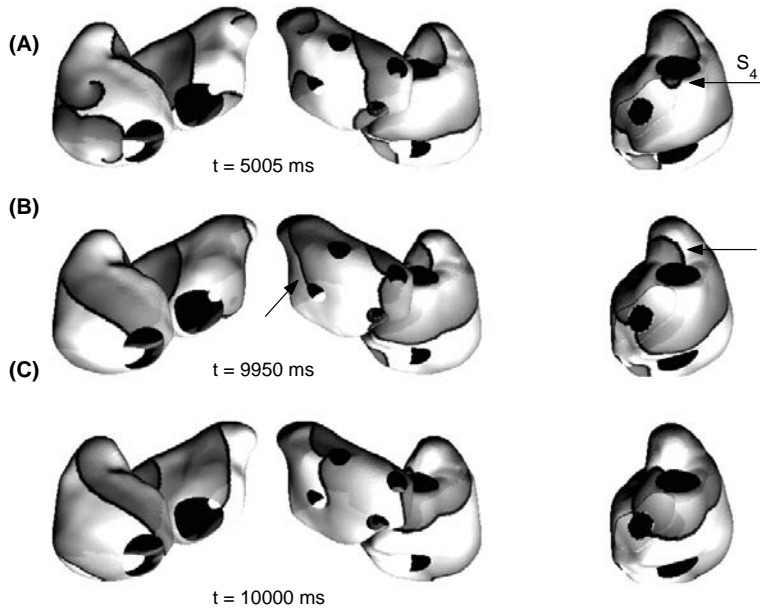


Figure 7.12 – Pacing in superior septum during chronic AF. (A)-(D) TMPDM. (A) The pacing site is indicated by S_4 . (B) The two arrows indicate wavelets anchored around the left inferior pulmonary vein (LIPV) and the superior vena cava (SVC), respectively. When ATP was reduced or stopped, AF was regenerated.

was neglected, and the stimulation delivered could not spread due to the fact that the tissue was in the ERP. However, when considering only the state of the tissue at the pacing site, the wavefronts generated by the other pacing sites were ignored, as result useless extra stimuli would be generated.

The position of the first pacing site was in the RAA and the second one in the left atrium appendage (LAA) (figure 7.4, sites S_2 and S_3). With this method, a full control of the atria was obtained. However, when the pacing was stopped, the fibrillation resumed due to residual wavelets. These residual wavelets were generated at the collision border between fronts generated by the two pacing sites or by reentries, caused by wavelets anchored around pulmonary veins as shown in figure 7.12(B).

7.4.2 Pacing meandering AF

During meandering AF, the dynamic of the wavelets is more organized than during chronic AF. The average number of wavelets is approximately 3 compared to 6 during chronic AF. Furthermore, the wavelength during meandering AF is longer than that of the chronic AF. Based on these observations, pace termination of AF meandering can be expected. This type of AF is close to AF type I and/or II, according to Wells' classification [167].

Figure 7.13 presents evolution of spatial correlation on the high density mapping during meandering AF pacing in the middle of the right atrium (figure 7.4, site S_1). The continuous

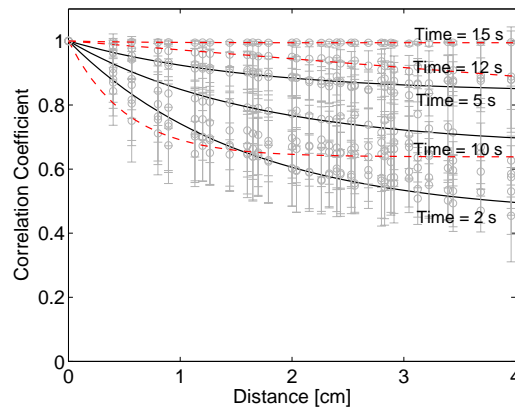


Figure 7.13 – Spatial correlation during pacing of meandering AF. Evolution of spatial correlation after constant pacing of 2 s, 5 s and 10 s (continuous line). The dashed lines represent pacing using a ramp protocol after 10 s, 12 s and 15 s. Means and standard deviations are respectively denoted by circles and bars.

curves represent pacing at a constant rate of 150 ms and the dashed curves, the pacing using a decrement ramp protocol of 1 ms. During constant pacing at 5 s, no control was obtained with a correlation value higher than 0.8. But at 10 s, this value decreased to 0.7, meaning that a loss of control occurred. Conversely, during the ramp protocol pacing, the correlation increased over time (10-15 s), until the maximum correlation of 1 after 15 s.

Figure 7.14 shows the spatial organization during pacing. Curves (1) and (2) correspond to regular pacing and ramp protocol pacing, respectively. After 15 s of pacing using a constant pacing interval, the complexity expressed by $CEig_{95\%}$ and $CEnt$ did not vary considerably, staying over 20 and around 3, respectively. No control was obtained during

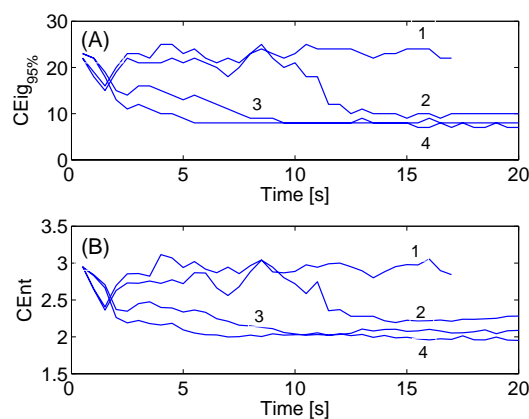


Figure 7.14 – Measure of complexity during pacing of meandering AF. (A) $CEig_{95\%}$. (B) $CEnt$. (1) Pacing in the right atrium free wall without ramp protocol. (2) Pacing in the right atrium free wall with decrement ramp protocol of 1 ms. (3) Pacing in the superior septum with a decrement of 1 ms. (4) Pacing in the superior septum with a decrement of 2 ms.

the whole process. However, after 18 s AF self-termination has taken place, which would have appeared if no pacing was applied. The conclusion of this observation is that regular ATP pacing is not a mechanism leading to pace-termination.

On the other hand, pacing with a decremented ramp of 1 ms (figure 7.14(2)) induced a decrease of complexity over time. Once again, AF termination was not completely due to the ATP protocol. AF was terminated by the annihilation of mutual wavelets as previously mentioned. However, using the decreasing ramp protocol, atrial reorganization was apparent. By modifying the local dynamics, the action potential duration (APD) of the system was changed. When the rate of pacing decreased, the diastolic interval (DI) adjusted itself, as well as the APD, following the restitution curve (section 3.3.4, figure 3.11). So, the APD became longer and termination was facilitated.

One of the specific characteristics of the meandering AF is the very low number of wavelets (2-4) with a few wavelets reentries, due to the long APD. Also, a large spatial dispersion of action potential duration is present on the surface of the atria. When applying the pacing, the wavefronts generated by the stimuli could not propagate in an isotropic and circular manner and wave breaks could appear. By decrementing the pacing rate, it was possible to slowly modify the spatial APD distribution, which allowed for a better control of the atria and prevented reentries during pacing.

Figure 7.15 shows an example of this phenomenon during pacing in the superior part of the septum (figure 7.4, site S_4). At 1145 ms the atria were still not fully under control. A reentry wavelet situated in the septum was observable. After 1150 ms of constant pacing, both atria were controlled. Two wavefronts spread through the left and right atrium, respectively. If pacing was stopped, AF termination occurred. By continuing the stimulation, a reentry emerged on the right posterior atrium (indicated by an arrow in figure 7.15(D)).

To avoid this mechanism of reentry and to permanently control the atria, a ramp protocol was tested with increments of 1 and 2 ms (underdrive pacing). By increasing the waiting time τ by 1 or 2 ms between each successive stimulation, it was possible to pace terminate AF. Figure 7.14 (curves (3) and (4)) displays the evolution of complexity during pacing in the septum region. The complexity decreased very rapidly compared to what was observed when pacing in the right atrium free wall. With an increment of 1 ms, control was obtained after 10 ms and 5 ms with a decrement of 2 ms.

As one pacing electrode was sufficient to pace-terminate meandering AF, multi-site pacing with this type of AF is not necessary, and it was not investigated in the present study.

7.4.3 Pacing cholinergic AF

Figure 7.16 and figure 7.17 present the evolution of spatial correlation curve on the high density mapping and the spatial organization during chronic AF, respectively. After 10 s of pacing in the right atrium free wall (figure 7.4, site S_1), the correlation coefficient of the local organization did not reach 1 as in chronic AF pacing. Due to the heterogeneities, a

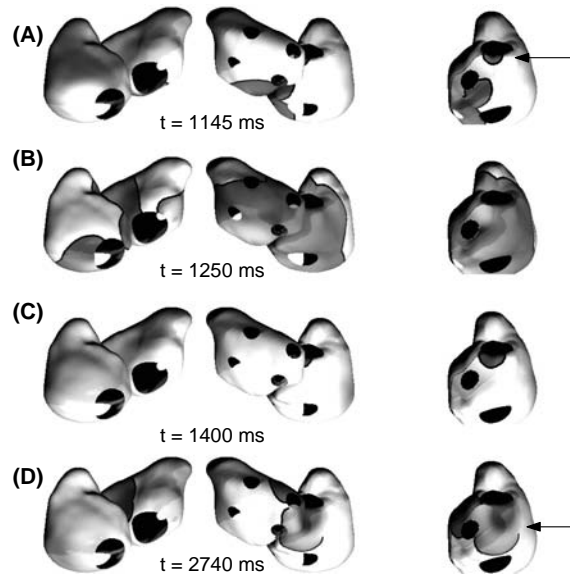


Figure 7.15 – Pacing in septum (site S_4) during meandering AF. (A)-(D) MPSPM. (A) The pacing site is indicated by an arrow. (D) The arrow indicates the reentry due to the spatial distribution of the action potential duration on the right atrium.

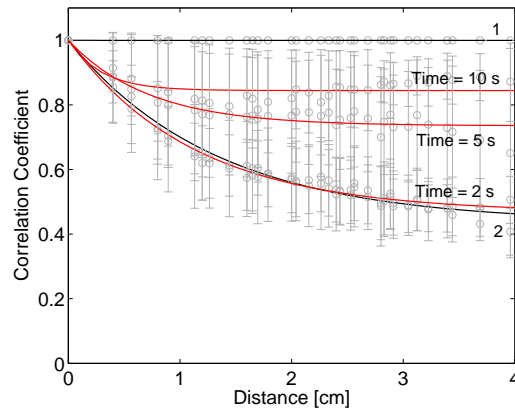


Figure 7.16 – Spatial correlation during pacing of cholinergic AF. (1) Sinatrial rhythm. (2) Cholinergic AF. Evolution of spatial correlation after pacing of 2 s, 5 s and 10 s. Means and standard deviations are respectively denoted by circles and bars.

full control of the right anterior free wall was not possible, and persistent reentries were still present. First, heterogeneities did not allow the wavefront generated by the stimulation to propagate in a homogeneous manner. Some patches with different ERP induced wave breaks. Second, a mother wavelet anchored on the left atrium appendage generated wavefronts colliding with wavefronts generated by the stimulation. It was never possible to unanchor this mother rotor. By observing the time evolution of the global organization (figure 7.17), the complexity $CEig_{95\%}$ and $CEnt$ did not decrease as much as during chronic AF pacing.

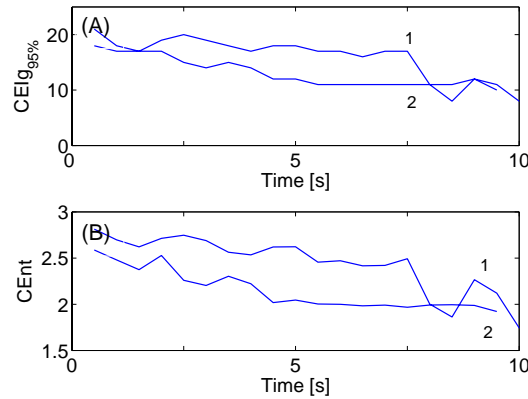


Figure 7.17 – Measure of complexity during pacing of cholinergic AF. (A) $CEig_{95\%}$. (B) $CEnt$. (1) Cholinergic AF. (2) Pacing.

As the mother rotor was close to the left appendage, the pacing site S_3 and the middle of the mother rotor tip were used as pacing sites. The results obtained were not satisfactory. The mother rotor persisted. When pacing in the site S_3 , the generated wavefront could not propagate and spread due to the wavefront generated by the mother rotor. Furthermore, the wavefront produced by the stimulation could not reach the spiral tip of the mother rotor. As the ERP in the tip region was very short (45 ms in the tissue and 95 ms in the heterogeneities region), an excitable gap was almost non-existent, and the ERP restitution curve was completely flattened (figure 3.11) resulting in a very stable state of the action potential duration. Therefore the stimulation could not be introduced or could not propagate to unanchor the mother rotor, even when the stimulation was applied in the middle of the tip.

7.5 Conclusions

The present chapter has shown therapeutic pacing experimented on a biophysical model. A closed-loop algorithm based on beat-to-beat intervals was proposed to investigate anti-tachypacing. An increasing/decreasing ramp protocol can be used with this method. It was used to pace terminate atrial flutter as well as less complex atrial fibrillation. As reported in the literature, the effectiveness of atrial ATP therapies has been shown to diminish as the arrhythmia cycle length shortens below 200 ms [168].

The results obtained confirm that atrial flutter can be pace-terminated by pacing in the right atrium appendage or in the isthmus region.

Depending on the type of atrial fibrillation, the model demonstrated that chronic AF could not be pace terminated. But a region of 4-6 cm of diameter can be controlled when pacing in the right atrium and both atria can be controlled when pacing in the septum region. However, AF resumed when control was stopped due to reentries anchored around pulmonary veins. Multisite pacing has been tested and control was observed but AF termi-

nation could not be achieved due to wavelet collisions near the controlled region borders.

During meandering AF, pace termination was accomplished with a ramp protocol and with an electrode placed on the right atrium or in the septum region.

In another case, simulation of the pacing of cholinergic AF showed no control was obtained during the whole process, even with multisite pacing.

The results obtained with the biophysical model are in accordance with the results obtained by electrophysiologists during clinical procedure: atrial flutter could be pace-terminated and local capture was obtained with complex atrial fibrillation.

Conclusion



THE work presented in this thesis is a part of a larger project to establish a general research framework for atrial fibrillation (AF). It is the continuation of the two previous theses accomplished by Olivier Blanc [4] and Vincent Jacquemet [5]. These works focused mainly on the development of a biophysical model of the human atria: development of an atrial geometry, implementation of membrane kinetics models and study of electrogram signal morphology.

Now the biophysical model has reached an advanced stage, it can be used as an efficient tool to study AF as well as atrial therapies. Hypotheses can be investigated or validated and propositions of new strategies on therapies can be made. The current work brings to light the fact that, for the first time, a biophysical model of the human atria can be used to investigate AF treatments.

Investigation of atrial therapies by means of a biophysical model has several advantages when compared to animal or human experiment. First, from an economical point of view, simulation requires a major investment in the development phase (scientists and computers) and only limited maintenance costs. With clinical experiments, the cost includes at the very least surgeons and electrophysiologists time, animals, and operation rooms. Second, the main drawback of animal experiments is the difficulty of accessing the whole atria and the difference between animal and human hearts. Finally, compared to clinical and animal studies, simulation presents the advantage of repeatability of the experiments under controlled conditions.

In spite of the presents limitations due to computer power, results obtained with the biophysical model were comparable to those obtained in clinical experiments, which validated first the biophysical model. Then, new therapeutic strategies were proposed to clinicians.

Those strategies should be assessed in a clinical environment.

The purpose of the current work has been firstly the development of methods to determine the organization during AF and to differentiate different types of AF. Secondly, investigation of atrial therapies using a biophysical model of human atria has been considered. This thesis demonstrates that the biophysical model can now be used as a standard tool to investigate new therapies. Furthermore, biophysical modeling has now reached a point of maturity which, in light of the future developments, justifies sharing results with a broad cardiologist audience.

In this chapter the most important issues and contributions presented in this thesis are reviewed. Then possible extensions of the presented work are discussed.

8.1 Summary of achievements

In this thesis, the major achievements can be summarized as follows.

Atrial arrhythmias

The biophysical model was used to simulate various types of atrial arrhythmia. In the continuation of the previous work by Jacquemet [5], which presented different types of AF, the simulation of atrial flutter (AFL) was integrated. The AFLs were simulated in a monolayer 3D biophysical model as well as in the multilayer 3D model. Different macro-reentry circuits were observed depending of the inclusion of slow and fast velocity conduction regions and boundaries. Stable AFL type I, which is the most common type of AFL, was obtained for a few seconds.

Measures of organization

Measures of organization were developed to quantify and classify different types of AF. The AF organization was evaluated at the electrogram signal level, as well as at the cellular level.

In chapter 4, a high density mapping system and a geometrical splitting of the atrial geometry had permitted the investigation of local and global activities during AF. Signal processing methods based on principal component analysis were applied to the electrogram signals. Results showed that using 64 electrodes uniformly distributed on the surface of the atria, it was possible to capture AF complexity. Four types of atrial arrhythmia were investigated with the biophysical model: atrial flutter, chronic AF, meandering AF and cholinergic AF.

In chapter 5, a new algorithm for phase singularity detection and tracking was proposed to study organization at the cellular level. This method classifies different types of AF and their evolution over time. Through all simulations it was found that major phase singularities were mainly located close to the large anatomical obstacles and long-living

phase singularities were clustered in space over the right and left atrium free wall.

Therapies

During this work, two different atrial therapies were investigated: surgical/catheter ablation and low energy electrical stimulation.

In chapter 6, the biophysical model was used first to study the efficiency of ablation procedure. The results confirmed the superiority of aggressive surgical procedures to terminate chronic AF. It was also observed in the simulations that some lines are more sensitive to imperfections than others, leading generally to the presence of uncommon atrial flutter after ablation. The results obtained were confirmed by those from clinical studies. Furthermore, an ideal ablation pattern was proposed using the biophysical model. The Maze-III procedure could be simplified in the right atrial atrium to a single line joining superior to inferior vena cava.

In chapter 7, the second therapeutic approach investigated was the therapeutic pacing. An algorithm for pacing and different pacing sites were investigated during this work. Anti-tachycardia pacing on different types of AF was experimented; the simulations showed that more organized arrhythmias such as atrial flutter or meandering AF can be pace terminated. Whereas, only local capture was possible on more complex AF. The results obtained with the biophysical model are in agreement with clinical studies.

8.2 Perspectives

The work presented in this thesis can be extended in various ways.

Biophysical model of the human atria

The biophysical model of human atria could be improved by adding more realistic heterogeneity, anisotropy and fibrosis based on physiological data from the literature. But these data are still not available and further investigations need to be performed *in vitro* by electrophysiologists before being implemented in the model.

Atrial arrhythmias

Several arrhythmias were presented in this research work: flutter, chronic AF, meandering AF and cholinergic AF. The initiation of the actual flutter can still be improved by multiple stimuli, with an appropriately chosen delay. In addition, anisotropic velocity conduction in the isthmus region should be added to facilitate AFL initiation by burst pacing or simultaneous stimulations delivered from several sites. The pathway of the typical counter-clockwise flutter is not stable. Further understanding of this mechanism and in particular the role of the crista terminalis needs to be investigated to obtain a sustained flutter.

Therapies

In the present work, defibrillation was not investigated due to the fact that defibrillation uses energy above the threshold of pain. Also, to simulate defibrillation, a bidomain model needs to be implemented to consider the extra- and the intracellular current flows.

The ablation procedures were applied on a healthy model of atria. It is known that during AF, atria are usually dilated. The next step will be to dilate the geometry, either on the right atrium or left atrium, to fit real physiological conditions.

Antitachycardia pacing algorithms could be improved by implementing more sophisticated algorithms. One solution consists of using prediction methods to predict the next beat-to-beat interval and applying a stimulus during the excitable gap. Other approaches, not based on beat-to-beat intervals, could be based directly on the analysis of the electrogram signals. Signals processing techniques such as matching pursuit, wavelets analysis, hidden Markov model and dynamic time warping may be an issue to analyze the morphology of the signals.

It has been shown that chronic and cholinergic AF could not be pace-terminated by antitachypacing. By combining ablation and pacing techniques, solutions could be found to cardiovert AF.

Anti-arrhythmic drugs could be tested on the atria. By changing the properties of the membrane kinetics on the biophysical model, simulation of drug therapies could be investigated. Prior to that, an appropriate knowledge of the cellular conditions inducing AF needs to be acquired, as well as the implementation of more appropriate membrane kinetics models.

Extension to the heart

Since the biophysical model of the human atria is well established, one of its possible extensions would be to add the ventricles. The addition of these and a 3D thorax model will allow one to compute surface electrocardiograms, comparable to what clinicians can observe. By modifying the substrate generating AF, modification on the surface electrocardiograms are induced. The comparison between simulated and clinical electrocardiograms, could lead to a better understanding of AF pathologies. Thus, the biophysical model of human atria can indeed assist clinicians in their diagnostics.

Bibliography

- [1] M. K. Chung. Current clinical issues in atrial fibrillation. *Cleve Clin J Med*, 70 Suppl 3:S6–11, 2003. 0891-1150 Journal Article Review Review, Tutorial.
- [2] I. Savelieva and A. J. Camm. Atrial pacing for the prevention and termination of atrial fibrillation. *Am J Geriatr Cardiol*, 11(6):380–398, 2002.
- [3] R. D. Smith. *Simulation: The Engine Behind the Virtual World*. Simulation 2000. ematter edition, 1999.
- [4] O. Blanc. *A computer model of human atrial arrhythmia*. PhD thesis, Swiss Federal Institute of Technology, 2001.
- [5] V. Jacquemet. *A biophysical model of atrial fibrillation and electrograms: Formulation, validation and applications*. PhD thesis, Swiss Federal Institute of Technology, 2004.
- [6] S. Zozor, O. Blanc, V. Jacquemet, N. Virag, J.-M. Vesin, E. Pruvot, L. Kappenberger, and C. Henriquez. A numerical scheme for modeling wavefront propagation on a monolayer of arbitrary geometry. *IEEE Trans Biomed Eng.*, 50(4):412–420, 2003.
- [7] A. C. Guyton and J. E. Hall. *Textbook of Medical Physiology 9th Ed*. W. b. saunders co edition, 1996.
- [8] W. Huda and R. Slone. *Review of radiologic physics*. Lippincott Williams & Wilkins, Philadelphia, 1995.
- [9] G. K. Moe, W. C. Rheinboldt, and J. A. Abildskov. A computer model of atrial fibrillation. *Am Heart J.*, 67:200–220, 1964.
- [10] E. Macchi. Digital-computer simulation of the atrial electrical excitation cycle in man. *Adv Cardiol.*, 10:102–110, 1974.
- [11] C. J. Kafer. Internodal pathways in the human atria: a model study. *Comput Biomed Res.*, 24:549–563, 1991.

-
- [12] R. Killmann, P. Wach, and F. Dienstl. Three-dimensional computer model of the entire human heart for simulation of reentry and tachycardia: gap phenomenon and wolff-parkinson-white syndrome. *Basic Res Cardiol.*, 86:485–501, 1991.
- [13] M. Lorange and R. M. Gulrajani. A computer heart model incorporating anisotropic propagation, i: model construction and simulation of normal activation. *J Electrocardiol.*, 26(4):245–260, 1993.
- [14] D. Wei, O. Okazaki, K. Harumi, E. Harasawa, and H. Hosaka. Comparative simulation of excitation and body surface electrocardiogram with isotropic and anisotropic computer heart models. *IEEE Trans Biomed Eng.*, 42:343–357, 1995.
- [15] R. A. Gray and J. Jalife. Ventricular fibrillation and atrial fibrillation are two different beasts. *Chaos*, 8(1):65–78, 1998.
- [16] O. Blanc, J.-M. Vesin, N. Virag, O. Egger, J. Koerfer, and L. Kappenberger. Computer simulation of atrial arrhythmias. *EPFL-SCR*, 11:32–35, 1999.
- [17] W. S. Ellis, A. SippensGroenewegen, D. M. Auslander, and M. D. Lesh. The role of the crista terminalis in atrial flutter and fibrillation: a computer modeling study. *Ann Biomed Eng.*, 28(7):742–54, 2000.
- [18] C. W. Zemlin, H. Herzel, S. Y. Ho, and A. V. Panfilov. A realistic and efficient model of excitation propagation in the human atria. In N. Virag, O. Blanc, and L. Kappenberger, editors, *Computer Simulation and Experimental Assessment of Cardiac Electrophysiology*, pages 29–34. Futura, New-York, 2000.
- [19] D. M. Harrild and C. S. Henriquez. A computer model of normal conduction in the human atria. *Circ Res*, 87(7):25e–36e, 2000.
- [20] E. J. Vigmond, R. Ruckdeschel, and N. Trayanova. Reentry in a morphologically realistic atrial model. *J. Cardiovasc. Electrophysiol.*, 12(9):1046–1054, 2001.
- [21] N. Virag, V. Jacquemet, C. Henriquez, S. Zozor, O. Blanc, J.-M. Vesin, E. Pruvot, and L. Kappenberger. Study of atrial arrhythmias in a computer model based on mr images of human atria. *Chaos*, 12(3):754–763, 2002.
- [22] C. Höper, G. Seemann, F. B. Sachse, H. Zhang, and O. Dossel. 3d computer model of human atrial anatomy and electrophysiology. In *Biomedizinische Technik.*, 48(1):2–3, 2003.
- [23] C. S. Henriquez and A. A. Papazoglou. Using computer models to understand the roles of tissue structure and membrane dynamics in arrhythmogenesis. *Proc. of the IEEE*, 84(3):334–354, 1996.
- [24] C. Luo and Y. Rudy. A model of the ventricular cardiac action potential. depolarization, repolarization, and their interaction. *Circ Res*, 68(6):1501–1526, 1991.

-
- [25] M. Courtemanche, R. J. Ramirez, and S. Nattel. Ionic mechanisms underlying human atrial action potential properties: insights from a mathematical model. *Am J Physiol Heart Circ Physiol*, 275(1):H301–321, 1998.
- [26] F. Xie, Z. Qu, A. Garfinkel, and J. N. Weiss. Electrical refractory period restitution and spiral wave reentry in simulated cardiac tissue. *Am J Physiol Heart Circ Physiol*, 283(1):H448–H460, 2002.
- [27] L. Glass. Dynamics of cardiac arrhythmias. *Phys Today*, 49:4045., 1996.
- [28] Z. Qu, J. Weiss, and A. Garfinkel. Cardiac electrical restitution properties and stability of reentrant spiral waves: a simulation study. *Am J Physiol Heart Circ Physiol*, 276(H269-H238), 1999.
- [29] A. L. Hodgkin and A. F. Huxley. A quantitative description of membrane current and its application to conduction and excitation in nerve. *J. Physiol.*, 117:500–544, 1952.
- [30] G. W. Beeler and H. Reuter. Reconstruction of the action potential of ventricular myocardial fibres. *J Physiol*, 268(1):177–210, 1977. 0022-3751 Journal Article.
- [31] C.-H. Luo and Y. Rudy. A dynamic model of the cardiac ventricular action potential. i. simulations of ionic currents and concentration changes. *Circ. Res.*, 74(6):1071–1096, 1994.
- [32] C. S. Henriquez. Simulating the electrical behavior of cardiac tissue using the bidomain model. *Crit Rev Biomed Eng.*, 21(1):1–77., 1993.
- [33] A. V. Holden and A. V. Panfilov. Modeling propagation in excitable media. In A. V. Panfilov and A. V. Holden, editors, *Computational Biology of the Heart*, pages 66–99. John Wiley and Son, West Sussex, 1997.
- [34] J. Rogers, M. Courtemanche, and A. McCulloch. Finite element methods for modeling impulse propagation in the heart. In A. V. Panfilov and A. V. Holden, editors, *Computational Biology of the Heart*, pages 217–233. John Wiley and Son, West Sussex, 1997.
- [35] J. P. Keener and K. Bogar. A numerical method for the solution of the bidomain equations in cardiac tissue. *Chaos*, 8(1):234–241, 1998. 1054-1500 Journal article.
- [36] H. I. Saleheen and K. T. Ng. A new three-dimensional finite-difference bidomain formulation for inhomogeneous anisotropic cardiac tissues. *IEEE Trans Biomed Eng*, 45(1):15–25, 1998.
- [37] A. T. Winfree. Rotors, fibrillation and dimensionality. In A. V. Panfilov and A. V. Holden, editors, *Computational Biology of the Heart*, pages 101–135. John Wiley and Son, West Sussex, 1997.

-
- [38] S. Y. Ho, R. H. Anderson, and D. Sanchez-Quintana. Atrial structure and fibres: morphologic bases of atrial conduction. *Cardiovasc. Res.*, 54(2):325–336, 2002.
- [39] S. Y. Ho, R. H. Anderson, and D. Sanchez-Quintana. Gross structure of the atriums: more than an anatomic curiosity? *Pacing Clin. Electrophysiol.*, 25(3):342–350, 2002.
- [40] Z. Qu and A. Garfinkel. An advanced algorithm for solving partial differential equation in cardiac conduction. *IEEE Trans Biomed Eng*, 46(9):1166–8, 1999. 0018-9294 Journal Article.
- [41] G. D. Smith. *Numerical Solution of Partial Differential Equations. Finite Difference Methods*. Oxford Univ. Press, 1986.
- [42] J. C. Strikwerda. *Finite difference schemes and partial differential equations*. Wadsworth Publ. Co, 1989.
- [43] A. Nygren, C. Fiset, L. Firek, J. W. Clark, D. S. Lindblad, R. B. Clark, and W. R. Giles. Mathematical model of an adult human atrial cell : The role of k⁺ currents in repolarization. *Circ Res*, 82(1):63–81, 1998.
- [44] J. A. McWilliam. Fibrillar contraction of the heart. *J. Physiol.*, 8:296, 1886.
- [45] W. A. Jolly and T. W. Ritchie. Auricular flutter and fibrillation. *Heart*, 3:177–221, 1911.
- [46] J. E. Olgin, J. M. Kalman, A. P. Fitzpatrick, and M. D. Lesh. Role of right atrial endocardial structures as barriers to conduction during human type i atrial flutter : Activation and entrainment mapping guided by intracardiac echocardiography. *Circulation*, 92(7):1839–1848, 1995.
- [47] A. L. Waldoo. *Atrial Flutter: From Mechanism to Treatment*, volume 14 of *Clinical approaches to tachyarrhythmias*. Futura Publishing Company, Inc., Armonk, New York, 2001.
- [48] P. A. Friedman. Novel mapping techniques for cardiac electrophysiology. *Heart*, 87(6):575–582, 2002.
- [49] K. W. Lee, Y. Yang, and M. M. Scheinman. Atrial flutter: a review of its history, mechanisms, clinical features, and current therapy. *Curr Probl Cardiol*, 30(3):121–67, 2005. 0146-2806 Journal Article.
- [50] M. M. Scheinman and Y. Yang. Atrial flutter: historical notes—part 1. *Pacing Clin Electrophysiol*, 27(3):379–81, 2004. 0147-8389 Historical Article Journal Article.
- [51] M. M. Scheinman, Y. Yang, and J. Cheng. Atrial flutter: Part ii nomenclature. *Pacing Clin Electrophysiol*, 27(4):504–6, 2004. 0147-8389 Historical Article Journal Article.

-
- [52] Y. Yang, N. Varma, and E. C. Keung. Surface ecg characteristics of intra-isthmus reentry. *PACE*, 26:1032, 2003.
- [53] Y. YANG, N. VARMA, E. C. KEUNG, and M. M. SCHEINMAN. Reentry within the cavotricuspid isthmus: An isthmus dependent circuit. *Pacing and Clinical Electrophysiology*, 28(8):808–818, 2005.
- [54] C. T. Tai, T. Y. Liu, P. C. Lee, Y. J. Lin, M. S. Chang, and S. A. Chen. Non-contact mapping to guide radiofrequency ablation of atypical right atrial flutter. *J Am Coll Cardiol*, 44(5):1080–6, 2004. 0735-1097 Journal Article.
- [55] P. Jais, D. C. Shah, M. Haissaguerre, M. Hocini, J. T. Peng, A. Takahashi, S. Garrigue, P. Le Metayer, and J. Clementy. Mapping and ablation of left atrial flutters. *Circulation*, 101(25):2928–2934, 2000.
- [56] A. Bochoeyer, Y. Yang, J. Cheng, R. J. Lee, E. C. Keung, N. F. Marrouche, A. Natale, and M. M. Scheinman. Surface electrocardiographic characteristics of right and left atrial flutter. *Circulation*, 108(1):60–66, 2003.
- [57] N. F. Marrouche, A. Natale, O. M. Wazni, J. Cheng, Y. Yang, H. Pollack, A. Verma, P. Ursell, and M. M. Scheinman. Left septal atrial flutter: electrophysiology, anatomy, and results of ablation. *Circulation*, 109(20):2440–7, 2004. 1524-4539 Journal Article.
- [58] H. Winterberg. Ueber herzflimmern und seine beeinflussung durch kampher. *Zeitschr. Exp. Pathol. Ther.*, 3:182–208, 1906.
- [59] M. A. Allesie, W. J. Lammers, B. F.I., and J. Hollen. Experimental evaluation of moe’s multiple wavelet hypothesis of atrial fibrillation. In D. P. Zipes and J. Jalife, editors, *Cardiac Electrophysiology and Arrhythmias.*, pages 265–76. Grune & Stratton, New York, 1985.
- [60] J. Jalife, O. Berenfelda, and M. Mansourb. Mother rotors and fibrillatory conduction: a mechanism of atrial fibrillation. *Cardiovasc. Res.*, 54(2):204–216, 2002.
- [61] J. Kneller, R. Zou, E. J. Vigmond, Z. Wang, L. J. Leon, and S. Nattel. Cholinergic atrial fibrillation in a computer model of a two-dimensional sheet of canine atrial cells with realistic ionic properties. *Circ. Res.*, 90(17):E73–87, 2002.
- [62] P. Attuel, R. Childers, B. Cauchemez, J. Poveda, J. Mugica, and P. Coumel. Failure in the rate adaptation of the atrial refractory period: its relationship to vulnerability. *Int J Cardiol*, 2(2):179–97, 1982. 0167-5273 Journal Article.
- [63] M. Boutjdir, J. Y. Le Heuzey, T. Lavergne, S. Chauvaud, L. Guize, A. Carpentier, and P. Peronneau. Inhomogeneity of cellular refractoriness in human atrium: factor of arrhythmia? *Pacing Clin Electrophysiol*, 9(6 Pt 2):1095–100, 1986. 0147-8389 Journal Article.

-
- [64] B.-S. Kim, Y.-H. Kim, G.-S. Hwang, H.-N. Pak, S. C. Lee, W. J. Shim, D. J. Oh, and Y. M. Ro. Action potential duration restitution kinetics in human atrial fibrillation. *Journal of the American College of Cardiology*, 39(8):1329–1336, 2002. TY - JOUR.
- [65] A. Arenal, J. Almendral, J. M. Alday, J. Villacastin, J. M. Ormaetxe, J. L. M. Sande, N. Perez-Castellano, S. Gonzalez, M. Ortiz, and J. L. Delcan. Rate-dependent conduction block of the crista terminalis in patients with typical atrial flutter : Influence on evaluation of cavotricuspid isthmus conduction block. *Circulation*, 99(21):2771–2778, 1999.
- [66] B. Schumacher, W. Jung, H. Schmidt, C. Fischenbeck, T. Lewalter, A. Hagedorff, H. Omran, C. Wolpert, and B. Luderitz. Transverse conduction capabilities of the crista terminalis in patients with atrial flutter and atrial fibrillation. *Journal of the American College of Cardiology*, 34(2):363–373, 1999. TY - JOUR.
- [67] C. T. Tai, S. A. Chen, Y. J. Chen, W. C. Yu, M. H. Hsieh, C. F. Tsai, C. C. Chen, Y. A. Ding, and M. S. Chang. Conduction properties of the crista terminalis in patients with typical atrial flutter: basis for a line of block in the reentrant circuit. *J Cardiovasc Electrophysiol.*, 9(8):811–119, 1998.
- [68] C. T. Tai, S. A. Chen, C. E. Chiang, S. H. Lee, K. C. Ueng, Z. C. Wen, J. L. Huang, Y. J. Chen, W. C. Yu, A. N. Feng, C. W. Chiou, and M. S. Chang. Characterization of low right atrial isthmus as the slow conduction zone and pharmacological target in typical atrial flutter. *Circulation*, 96(8):2601–11, 1997. 0009-7322 Journal Article.
- [69] F. G. Cosio. Atrial flutter update. *Card Electrophysiol Rev*, 6(4):356–64, 2002. 1385-2264 Journal Article Review Review, Tutorial.
- [70] M. S. Spach, 3rd Miller, W. T., D. B. Geselowitz, R. C. Barr, J. M. Kootsey, and E. A. Johnson. The discontinuous nature of propagation in normal canine cardiac muscle. evidence for recurrent discontinuities of intracellular resistance that affect the membrane currents. *Circ Res*, 48(1):39–54, 1981. 0009-7330 Journal Article.
- [71] J. E. Saffitz, H. L. Kanter, K. G. Green, T. K. Tolley, and E. C. Beyer. Tissue-specific determinants of anisotropic conduction velocity in canine atrial and ventricular myocardium. *Circ Res*, 74(6):1065–70, 1994. 0009-7330 Journal Article.
- [72] M. Haissaguerre, P. Jais, D. Shah, A. Takahashi, M. Hocini, G. Quiniou, S. Garrigue, A. L. Mouroux, P. L. Mtayer, and J. Clmenty. Spontaneous initiation of atrial fibrillation by ectopic beats originating in the pulmonary veins. *N. Engl. J. Med.*, 339(10):649–666, 1998.
- [73] R. B. Krol, S. Saksena, A. Prakash, I. Giorgberidze, and P. Mathew. Prospective clinical evaluation of a programmed atrial stimulation protocol for induction of sustained atrial fibrillation and flutter. *J Interv Card Electrophysiol*, 3(1):19–25, 1999. 1383-875x Journal Article.

-
- [74] A. S. Manolis, J. Cameron, T. Deering, E. H. Han, and 3rd Estes, N. A. Sensitivity and specificity of programmed atrial stimulation for induction of supraventricular tachycardias. *Clin Cardiol*, 11(5):307–10, 1988. 0160-9289 Journal Article.
- [75] Z. Qu, A. Garfinkel, P. S. Chen, and J. N. Weiss. Mechanisms of discordant alternans and induction of reentry in simulated cardiac tissue. *Circulation*, 102(14):1664–70, 2000. 1524-4539 Journal Article.
- [76] A. Vinet, D. R. Chialvo, D. C. Michaels, and J. Jalife. Nonlinear dynamics of rate-dependent activation in models of single cardiac cells. *Circ Res*, 67(6):1510–24, 1990. 0009-7330 Journal Article.
- [77] F. Fenton and A. Karma. Vortex dynamics in three-dimensional continuous myocardium with fiber rotation: Filament instability and fibrillation. *Chaos*, 8(1):20–47, 1998.
- [78] E. Vigmond and L. J. Leon. Restitution curves and the stability of reentry in three-dimensional simulations of cardiac tissue. *Comput Visual Sci.*, 5:1–11, 2002.
- [79] J. Chen, R. Mandapati, O. Berenfeld, A. C. Skanes, R. A. Gray, and J. Jalife. Dynamics of wavelets and their role in atrial fibrillation in the isolated sheep heart. *Circ Res.*, 48(2):220–232, 2000.
- [80] J. Wang, L. Liu, J. Feng, and S. Nattel. Regional and functional factors determining induction and maintenance of atrial fibrillation in dogs. *Am J Physiol Heart Circ Physiol*, 271(1):H148–158, 1996.
- [81] R. Arora, S. Verheule, L. Scott, A. Navarrete, V. Katari, E. Wilson, D. Vaz, and J. E. Olgin. Arrhythmogenic substrate of the pulmonary veins assessed by high-resolution optical mapping. *Circulation*, 107(13):1816–21, 2003. 1524-4539 Journal Article.
- [82] S. Fareh, C. Villemaire, and S. Nattel. Importance of refractoriness heterogeneity in the enhanced vulnerability to atrial fibrillation induction caused by tachycardia-induced atrial electrical remodeling. *Circulation*, 98(20):2202–2209, 1998.
- [83] M. N. Obreztkhikova, E. A. Sosunov, E. P. Anyukhovskiy, N. S. Moise, R. B. Robinson, and M. R. Rosen. Heterogeneous ventricular repolarization provides a substrate for arrhythmias in a german shepherd model of spontaneous arrhythmic death. *Circulation*, 108(11):1389–94, 2003. 1524-4539 Journal Article.
- [84] V. Jacquemet, N. Virag, Z. Ihara, L. Dang, O. Blanc, S. Zozor, J.-M. Vesin, L. Kapfenberger, and C. Henriquez. Study of unipolar electrogram morphology in a computer model of atrial fibrillation. *J. Cardiovasc. Electrophysiol.*, 14:S172–S179, 2003.
- [85] V. Barbaro, P. Bartolini, G. Calcagnini, and F. Censi. Extraction of physiological and clinical information from intra-atrial electrograms during atrial fibrillation: review of methods. *Ann. Ist. Super Sanita.*, 37(3):319–324, 2001.

-
- [86] G. W. Botteron and J. M. Smith. A technique for measurement of the extent of spatial organization of atrial activation during atrial fibrillation in the intact human heart. *IEEE Trans Biomed Eng.*, 42(6):579–586, 1995.
- [87] F. Censi, V. Barbaro, P. Bartolini, G. Calcagnini, A. Michelucci, G. F. Gensini, and S. Cerutti. Recurrent patterns of atrial depolarization during atrial fibrillation assessed by recurrence plot quantification. *Ann Biomed Eng*, 28(1):61–70, 2000. 0090-6964 Journal Article.
- [88] M. Kirchner, L. Faes, E. Olivetti, R. Riccardi, M. Scaglione, F. Gaita, and R. Antolini. Local electrical characterisation of human atrial fibrillation. *Computer in Cardiology*, 27:499–502, 2000.
- [89] K. T. S. Konings, J. L. R. M. Smeets, O. C. Penn, H. J. J. Wellens, and M. A. Allesie. Configuration of unipolar atrial electrograms during electrically induced atrial fibrillation in humans. *Circulation*, 95(5):1231–1241, 1997.
- [90] G. K. Moe. On the multiple wavelet hypothesis of atrial fibrillation. *Arch Int Pharmacodyn Ther*, 140:83188., 1962.
- [91] H. J. Sih, D. P. Zipes, E. J. Berbari, and J. E. Olgin. A high-temporal resolution algorithm for quantifying organization during atrial fibrillation. *IEEE Trans. Biomed. Eng.*, 46(4):440–450, 1999.
- [92] P. Jais, M. Haissaguerre, D. C. Shah, S. Chouairi, and J. Clementy. Regional disparities of endocardial atrial activation in paroxysmal atrial fibrillation. *Pacing Clin Electrophysiol*, 19(11 Pt 2):1998–2003, 1996. 0147-8389 Journal Article.
- [93] V. Barbaro, P. Bartolini, G. Calcagnini, S. Morelli, A. Michelucci, and G. Gensini. Automated classification of human atrial fibrillation from intraatrial electrograms. *Pacing Clin Electrophysiol*, 23(2):192–202, 2000. 0147-8389 Journal Article.
- [94] A. Sahakian, K. Ropella, and S. Swiryn. Atrial electrograms and the characterization of atrial fibrillation. *J Electrocardiol*, 24 Suppl:131–3, 1992. 0022-0736 Journal Article.
- [95] E. G. Lovett and K. M. Ropella. Time-frequency coherence analysis of atrial fibrillation termination during procainamide administration. *Ann Biomed Eng*, 25(6):975–84, 1997. 0090-6964 Clinical Trial Journal Article.
- [96] J. Jalife, O. Berenfeld, A. Skanes, and R. Mandapati. Mechanisms of atrial fibrillation: mother rotors or multiple daughter wavelets, or both? *J Cardiovasc Electrophysiol*, 9(8 Suppl):S2–12, 1998. 1045-3873 Journal Article Review Review, Tutorial.
- [97] B. P. Hoekstra, C. G. Diks, M. A. Allesie, and J. DeGoede. Nonlinear analysis of epicardial atrial electrograms of electrically induced atrial fibrillation in man. *J Cardiovasc Electrophysiol.*, 6(6):419–440, 1995.

-
- [98] H. F. Pitschner, A. Berkovic, S. Grumbrecht, and J. Neuzner. Multielectrode basket catheter mapping for human atrial fibrillation. *J Cardiovasc Electrophysiol*, 9(8 Suppl):S48–56, 1998. 1045-3873 Clinical Trial Journal Article.
- [99] A. Berkowitsch, J. Carlsson, A. Erdogan, J. Neuzner, and H. F. Pitschner. Electrophysiological heterogeneity of atrial fibrillation and local effect of propafenone in the human right atrium: analysis based on symbolic dynamics. *J Interv Card Electrophysiol*, 4(2):383–94, 2000. 1383-875x Journal Article.
- [100] R. Arora, M. K. Das, D. P. Zipes, and J. Wu. Optical mapping of cardiac arrhythmias. *Indian Pacing Electrophysiol. J.*, 3(4):187–196, 2003.
- [101] G. H. Dunteman. *Principal Components Analysis*, volume 69 of *Quantitative Applications in the Social Sciences*. SAGE Publications, Inc., Newbury Park, California 91320, 1989.
- [102] C. E. Shannon. A mathematical theory of communication. *Bell Syst. Tech. J.*, 27:379–423, 623–656, 1948.
- [103] A. Palacios, G. H. Gunaratne, M. Gorman, and K. A. Robbins. Karhunen-love analysis of spatiotemporal flame patterns. *Phys. Rev. E*, 57(5):5958–5971, 1998.
- [104] G. W. Botteron and J. M. Smith. Quantitative assessment of the spatial organization of atrial fibrillation in the intact human heart. *Circulation*, 93(3):513–518, 1996.
- [105] S. Nattel. New ideas about atrial fibrillation 50 years on. *Nature*, 415(6868):219–226, 2002.
- [106] J. Chen, R. Mandapati, O. Berenfeld, A. C. Skanes, and J. Jalife. High-frequency periodic sources underlie ventricular fibrillation in the isolated rabbit heart. *Circ Res.*, 86(1):86–93, 2000.
- [107] R. A. Gray, M. P. Arkady, and J. Jalife. Spatial and temporal organization during cardiac fibrillation. *Nature*, 392:75–78, 1998.
- [108] A. M. Pertsov, J. M. Davidenko, R. Salomonsz, W. T. Baxter, and J. Jalife. Spiral waves of excitation underlie reentrant activity in isolated cardiac muscle. *Circ Res.*, 72(3):631–650, 1993.
- [109] A. T. Winfree. Electrical instability in cardiac muscle: phase singularities and rotors. *J Theor Biol.*, 138(3):353–405, 1989.
- [110] D. J. M., P. A. M., S. R., B. W. P., and J. J. Spatiotemporal irregularities of spiral wave activity in isolated ventricular muscle. *J Electrocardiol.*, 24:Suppl:113–122, 1992.
- [111] O. Landendorff. Untersuchungen am belebenden sugethierherzen. *Arch Gesante Physiol.*, 61:291–332, 1895.

-
- [112] R. H. Clayton and A. V. Holden. Filament behavior in a computational model of ventricular fibrillation in the canine heart. *IEEE Trans Biomed Eng.*, 51(1):28–34, 2004.
- [113] J. M. Rogers. Combined phase singularity and wavefront analysis for optical maps of ventricular fibrillation. *IEEE Trans Biomed Eng.*, 51(1):56–65, 2004.
- [114] R. Zou, J. Kneller, L. Leon, and S. Nattel. A novel method to detect phase singularity during atrial fibrillation. *Biophys. J. (Annual Meeting Abstracts)*, 82(1):93c–, 2002.
- [115] R. Zou, J. Kneller, L. J. Leon, and S. Nattel. Development of a computer algorithm for the detection of phase singularities and initial application to analyze simulations of atrial fibrillation. *Chaos*, 12:764–778, 2002.
- [116] A. T. Winfree. Varieties of spiral wave behavior: An experimentalist’s approach to the theory of excitable media. *Chaos*, 1(3):303–334, 1991.
- [117] A. N. Iyer and R. A. Gray. An experimentalist’s approach to accurate localization of phase singularities during reentry. *Ann Biomed Eng.*, 29(1):47–59, 2001.
- [118] N. H. Packard, J. P. Crutchfield, J. D. Farmer, and R. S. Shaw. Geometry from a time series. *Phys. Rev. Lett.*, 45:712–716, 1980.
- [119] F. Takens. Detecting strange attractors in turbulence.” dynamical systems and turbulence. In D.A. Rand and L.S. Young, editors, *Lecture Notes in Mathematics 898*, pages 366–81. Springer-Verlag, 1981.
- [120] D. P. Zipes and H. J. J. Wellens. What have we learned about cardiac arrhythmias ? *Circulation*, 102(20 (Suppl. 4)):IV52–IV57, 2000.
- [121] G. M. Guiraudon, C. S. Campbell, D. L. Jones, M. J.L., and M. J.L. Combined sino-atrial node atrio-ventricular node isolation: A surgical alternative to his’ bundle ablation in patients with atrial fibrillation. *Circulation*, 72(1):161–169, 1985.
- [122] S. M.M., F. Morady, H. D.S., and G. R. Catheter-induced ablation of the atrioventricular junction to control refractory supraventricular arrhythmias. *JAMA*, 248(7):851–855, 1982.
- [123] J. M. Williams, U. R.M., L. G.K., and J. L. Cox. Left atrial isolation: New technique for the treatment of supraventricular arrhythmias. *J. Cardiovasc. Electrophysiol.*, 80(3):373–80, 1980.
- [124] J. L. Cox. The surgical treatment of atrial fibrillation. iv. surgical technique. *J. Thorac. Cardiovasc. Surg.*, 101(4):584–92, 1991.
- [125] J. L. Cox. Modification of the maze procedure for atrial flutter and atrial fibrillation. i. rationale and surgical results. *J. Thorac. Cardiovasc. Surg.*, 110(2):473–84, 1995.

-
- [126] J. L. Cox, R. D. Jacquiss, S. R.B., and B. J.P. Modification of the maze procedure for atrial flutter and atrial fibrillation. ii. surgical technique of maze iii procedure. *J. Thorac. Cardiovasc. Surg.*, 110(2):485–95, 1995.
- [127] D. Keane. New catheter ablation techniques for the treatment of cardiac arrhythmias. *Card. Electrophysiol. Rev.*, 6(4):341–349, 2002.
- [128] H. Oral and F. Morady. Ablation of atrial fibrillation. *J. Cardiovasc. Electrophysiol.*, 15(1):112, 2004.
- [129] H. T. Sie, W. P. Beukema, A. Elvan, and A. R. Ramdat Mister. New stragies in the surgical treatment of atrial fibrillation. *Cardiovasc. Res.*, 58(3):501–509, 2003.
- [130] L. Thomas, A. Boyd, S. P. Thomas, N. B. Schiller, and D. L. Ross. Atrial structural remodelling and restoration of atrial contraction after linear ablation for atrial fibrillation. *Eur Heart J*, 24(21):1942–1951, 2003.
- [131] M. D. Cheitlin, W. F. Armstrong, G. P. Aurigemma, G. A. Beller, F. Z. Bierman, J. L. Davis, P. S. Douglas, D. P. Faxon, L. D. Gillam, T. R. Kimball, W. G. Kussmaul, A. S. Pearlman, J. T. Philbrick, H. Rakowski, D. M. Thys, E. M. Antman, Jr Smith, S. C., J. S. Alpert, G. Gregoratos, J. L. Anderson, L. F. Hiratzka, S. Ann Hunt, V. Fuster, A. K. Jacobs, R. J. Gibbons, and R. O. Russell. Acc/aha/ase 2003 guideline update for the clinical application of echocardiography: Summary article: A report of the american college of cardiology/american heart association task force on practice guidelines (acc/aha/ase committee to update the 1997 guidelines for the clinical application of echocardiography). *Circulation*, 108(9):1146–1162, 2003.
- [132] P. Ruchat, J. Schaefer, A. Delabays, M. Hurni, J. Milne, and L. K. v. Segesser. Left atrial radiofrequency compartmentalization for chronic atrial fibrillation during heart surgery. *Thorac. Cardiovasc. Surg.*, 50(3):155–159, 2002.
- [133] L. Dang, N. Virag, Z. Ihara, V. Jacquemet, O. Blanc, J.-M. Vesin, and L. Kapfenberger. Evaluation of ablation patterns by means of a computer model of human atria. In *Engineering in Medicine and Biology society. Proceedings of the 25th Annual International Conference of the IEEE*, volume 1, pages 126–129, Cancun, 2003.
- [134] W. S. Ellis, A. SippensGroenewegen, and M. Lesh. The effect of linear lesions on atrial defibrillation threshold and spontaneous termination. a computer modeling study. *PACE*, 20 (Part II):1145, 1997.
- [135] H. T. Sie, W. P. Beukema, A. R. Misier, A. Elvan, J. J. Ennema, M. M. Haalebos, and H. J. Wellens. Radiofrequency modified maze in patients with atrial fibrillation undergoing concomitant cardiac surgery. *J. Thorac. Cardiovasc. Surg.*, 122(2):249–259, 2001.

-
- [136] T. Nitta, Y. Ishii, H. Ogasawara, S. Sakamoto, Y. Miyagi, K. Yamada, S. Kanno, and T. S. Initial experience with the radial incision approach for atrial fibrillation. *Ann. Thorac. Surg.*, 68(3):805–810, 1999.
- [137] F. Isobe, H. Kumano, T. Ishikawa, Y. Sasaki, S. Kinugasa, K. Nagamachi, and Y. Kato. A new procedure for chronic atrial fibrillation: bilateral appendage-preserving maze procedure. *Ann. Thorac. Surg.*, 72(5):1473–1478, 2001.
- [138] C. Pappone, S. Rosanio, G. Oreto, M. Tocchi, F. Gugliotta, G. Vicedomini, A. Salvati, C. Dicandia, P. Mazzone, V. Santinelli, S. Gulletta, and S. Chierchia. Circumferential radiofrequency ablation of pulmonary vein ostia : A new anatomic approach for curing atrial fibrillation. *Circulation*, 102(21):2619–2628, 2000.
- [139] F. Morady. Catheter ablation of supraventricular arrhythmias: state of the art. *J Cardiovasc Electrophysiol*, 15(1):124–39, 2004. 1045-3873 Journal Article Review Review, Tutorial.
- [140] J. L. Cox, R. B. Schuessler, J. H. J. D’Agostino, C. M. Stone, B.-C. Chang, and M. E. Cain. The surgical treatment of atrial fibrillation iii. development of a definitive surgical procedure. *J. Thorac. Cardiovasc. Surg.*, 101(4):569–583, 1991.
- [141] A. Garg, W. Finneran, M. Mollerus, U. Birgersdotter-Green, O. Fujimura, L. Tone, and G. K. Feld. Right atrial compartmentalization using radiofrequency catheter ablation for management of patients with refractory atrial fibrillation. *J. Cardiovasc. Electrophysiol.*, 10(6):763–771, 1999.
- [142] H. Kottkamp, G. Hindricks, D. Hammel, R. Autschbach, J. Mergenthaler, M. Borggrefe, G. Breithardt, F.-W. Mohr, and H. H. Scheld. Intraoperative radiofrequency ablation of chronic atrial fibrillation: A left curative approach by elimination of anatomic ”anchor” reentrant circuit. *J. Cardiovasc. Electrophysiol.*, 10(6):772–780, 1999.
- [143] F. G. Cosio, F. Arribas, M. Lopez-Gil, and H. D. Gonzalez. Radiofrequency ablation of atrial flutter. *J Cardiovasc Electrophysiol.*, 7(1):60–70, 1996.
- [144] M. A. Mitchell, I. D. McRury, T. H. Everett, H. Li, J. M. Mangrum, and D. E. Haines. Morphological and physiological characteristics of discontinuous linear atrial ablations during atrial pacing and atrial fibrillation. *J. Cardiovasc. Electrophysiol.*, 10(3):378–86, 1999.
- [145] H. Nakagawa, R. Lazzara, T. Khastgir, K. J. Beckman, J. H. McClelland, S. Imai, J. V. Pitha, A. E. Becker, M. Arruda, M. D. Gonzalez, L. E. Widman, M. Rome, J. Neuhauser, X. Wang, J. D. Calame, M. D. Goudeau, and W. M. Jackman. Role of the tricuspid annulus and the eustachian valve/ridge on atrial flutter: Relevance to catheter ablation of the septal isthmus and a new technique for rapid identification of ablation success. *Circulation*, 94(3):407–424, 1996.

-
- [146] S. Furman. The early history of cardiac pacing. *null*, 26(10):2023–2032, 2003.
- [147] L. A. Geddes. Historical highlights in cardiac pacing. *IEEE Engineering in Medicine and Biology Magazine*, 9(2):12–18, 1990.
- [148] J. D. Fisher, Z. Zhang, S. G. Kim, K. J. Ferrick, J. A. Roth, and D. R. Johnston. Comparison of burst pacing, autodecremental (ramp) pacing, and universal pacing for termination of ventricular tachycardia. *Arch Mal Coeur Vaiss*, 89 Spec No 1:135–9, 1996. 0003-9683 Clinical Trial Journal Article Randomized Controlled Trial.
- [149] A. R. Mitchell and N. Sulke. Does rapid atrial pacing terminate atrial fibrillation? a comparison of laboratory and device termination studies. *Card. Electrophysiol. Rev.*, 7(4):352–454, 2003.
- [150] B. L. Zaret, M. Moser, and L. S. Cohen. *Yale University School of Medicine heart book*. New Haven, Conn. : Yale University School of Medicine., 1992.
- [151] H. J. J. Wellens. Contemporary management of atrial flutter. *Circulation*, 106(6):649–652, 2002.
- [152] A. R. J. Mitchell, P. A. R. Spurrell, L. Cheatle, and N. Sulke. Effect of atrial antitachycardia pacing treatments in patients with an atrial defibrillator: randomised study comparing subthreshold and nominal pacing outputs. *Heart*, 87(5):433–437, 2002.
- [153] M. A. Allesie, C. Kirchhof, G. J. Sheffer, F. Chorro, and J. Brugada. Regional control of atrial fibrillation by rapid pacing in conscious dogs. *Circulation*, 84(4):1689–697, 1991.
- [154] E. G. Daoud, B. Pariseau, M. Niebauer, F. Bogun, R. Goyal, M. Harvey, K. C. Man, S. A. Strickberger, and F. Morady. Response of type i atrial fibrillation to atrial pacing in humans. *Circulation*, 94(5):1036–1040, 1996.
- [155] C. Pandozi, L. Bianconi, M. Villani, A. Castro, G. Altamura, S. Toscano, A. P. Jesi, G. Gentilucci, F. Ammirati, F. L. Bianco, and M. Santini. Local capture by atrial pacing in spontaneous chronic atrial fibrillation. *Circulation*, 95(10):2416–2422, 1997.
- [156] A. R. Misier, W. P. Beukema, and R. Willems. Multisite atrial pacing for atrial fibrillation prevention: where to go from here? *Card Electrophysiol Rev*, 7(4):329–32, 2003. 1385-2264 Journal Article Review Review, Tutorial.
- [157] D. J. Callans, B. G. Hook, R. L. Mitra, and M. E. Josephson. Characterization of return cycle responses predictive of successful pacing-mediated termination of ventricular tachycardia. *Journal of the American College of Cardiology*, 25(1):47–53, 1995. TY - JOUR.
- [158] W. L. Ditto, M. L. Spano, V. In, J. Nefe, and B. Meadows. Control of human atrial fibrillation. *International Journal of Bifurcation and Chaos*, 10(3):593–601, 2000.

-
- [159] E. Ott, C. Grebogi, and J. A. Yorke. Controlling chaos. *Phys. Rev. Lett.*, 64(11):1196–1199, 1990.
- [160] J. P. Crutchfield, J. D. Farmer, N. H. Packard, and D. Shah. Chaos. *Sci Am.*, 255:46–67, 1986.
- [161] A. Garfinkel, M. L. Spano, W. L. Ditto, and J. N. Weiss. Controlling cardiac chaos. *Science*, 257:1230, 1992.
- [162] D. K. L. Peterson and M. J. Link. Method and apparatus for treatment of fibrillation, US Patent, us 6078837, 2000.
- [163] S. Sinha, K. M. Stein, and D. J. Christini. Critical role of inhomogeneities in pacing termination of cardiac reentry. *Chaos: An Interdisciplinary Journal of Nonlinear Science*, 12(3):893–902, 2002.
- [164] S. J. Bailin, S. Adler, and M. Giudici. Prevention of chronic atrial fibrillation by pacing in the region of bachmann’s bundle : Results of a multicenter randomized trial. *J. Cardiovasc. Electrophysiol.*, 12(8):912–917, 2001.
- [165] M. Kale and D. H. Bennett. Atrial septal pacing in the prevention of paroxysmal atrial fibrillation refractory to antiarrhythmic drugs. *Int. J. Cardiol.*, 82(2):167–175, 2002.
- [166] L. Padeletti, A. Michelucci, P. Pieragnoli, A. Colella, and N. Musilli. Atrial septal pacing: a new approach to prevent atrial fibrillation. *Pacing Clin. Electrophysiol.*, 27(6 Pt 2):850–854, 2004.
- [167] J. L. Wells, R. B. Karp, N. T. Kouchoukos, W. A. MacLean, T. N. James, and A. L. Waldo. Characterization of atrial fibrillation in man: studies following open heart surgery. *Pacing Clin Electrophysiol.*, 1(4):426–38, 1978.
- [168] A. R. J. Mitchell. Mitchell ar. the role of pacemaker and defibrillator therapy for the treatment of atrial fibrillation. *Minerva Cardioangiol*, 52:141–153, 2004.

Index

- Ablation, 79
 - pattern, 81
 - protocol, 87
- Action potential, 13
 - duration, 14
- Anisotropy, 74
 - ratio, 74
- Arrhythmia, 3, 25
- Atrial
 - fibrillation, 4, 27
 - flutter, 26, 28
 - therapy, 4
- Bachmann's bundle, 22
- Bidomain, 17
- Bipolar electrogram, 49
- Bradyarrhythmia, 3
- Bradycardia, 3
- Cardiac cell, 12
- Chaos control, 104
- Cholinergic AF, 39
- Chronic AF, 37
- Conductivity, 18
 - longitudinal, 74
 - transverse, 74
- Courtemanche-Ramirez-Nattel, 17
- Crista terminalis, 22
- Cycle length, 14
- Diastolic interval, 14
- Early repolarization, 14
- Effective refractory period, 14
- Electrical stimulation, 4, 103
- Electrocardiogram, 20, 26
- Electrogram, 20
- Entropy, 50
- Excitable gap, 103
- Gap, 85
- Gap junction, 13
- Gate kinetics, 16
- Gating variable, 16
- Heterogeneity, 39, 74
- High density mapping, 47
- Imperfect ablation line, 85
- Inhomogeneity, 74
- Initiation atrial fibrillation, 36
- Isolation of pulmonary veins, 84, 97
- Lagendoff-perfused, 58
- Late repolarization, 14
- Limitation, 99
- Luo-Rudy, 16
- Maze procedure, 79
- Maze-III, 79, 95
- Meandering AF, 39
- Measure of organization, 46, 88
- Membrane
 - kinetics, 11
 - potential, 13
- Monodomain, 19
- Mother rotor, 28
- Multidimensional signal analysis, 49
- Pacemaker, 101
- Pacing, 103
 - site, 106
- Pectinate muscles, 22

- Perpetuation of atrial fibrillation, 36
- Phase singularity, 57, 58, 61
 - distribution, 73
 - lifespan, 71
 - localization, 61
 - tracking, 64
- Phase variable, 58
- Plateau, 14
- Poincaré map, 104
- Principal component analysis, 50

- Radio frequency, 79
- Radiofrequency ablation, 4
- Reentry, 15
- Remodeling, 28
- Resting potential, 14
- Restitution curve, 14

- Sinoatrial rhythm, 26
- Space constant, 50
- Spatial correlation, 49
- Stimulation current, 15

- Tachyarrhythmia, 3
- tachycardia, 3
- Triangular mesh, 22

- Unipolar electrogram, 49
- Unstable fixed points, 104
- Upstroke, 14

- Ventricular fibrillation, 4

- Wave length, 50

Curriculum Vitae

Lam DANG

Citizenship: Swiss

Birthdate: October 16, 1974

Gender/Status: male, single

Rue du Simplon, 3

1020 Renens, SWIZERLAND

Phone: +41-21 634 03 74

Mobile: +41-76 589 24 14

E-mail: Lam.Dang@epfl.ch

Objectives

My main interest lies in the study of atrial arrhythmias and therapies using a biophysical model of the human atria.

Education

- 01/2002 - PRESENT Swiss Federal Institute of Technology, Lausanne, Switzerland (EPFL)
Research assistant and PhD student at Signal Processing Institute.
- 03/2001 - 10/2001 Swiss Federal Institute of Technology, Lausanne, Switzerland (EPFL)
University of Lausanne, Switzerland (UNIL)
University of Geneva, Switzerland (UNIGE)
Postgraduate in Biomedical Engineering.
- 10/1994 - 03/2001 Swiss Federal Institute of Technology, Lausanne, Switzerland (EPFL)
Master Science in Micro-Engineering. Specialization in engineering processes and production management.
- 08/1990 - 06/1994 Collège Voltaire, Geneva
Baccalaureate, specialization in engineering.
-

Languages

FRENCH	Native language
ENGLISH	Fluent
GERMAN	Intermediate
CHINESE	Native language, oral
VIETNAMESE	Basic notions

Experiences and projects

- 01/2002 - PRESENT Research Assistant and PhD candidate at the Signal Processing Institute, EPFL. Research activities: numerical simulations of atrial therapies. Teaching activities: definition and supervision of semester and diploma student projects.
- 07/2001 - 11/2001 Postgraduate diploma project at EPFL: Analysis of Evoked Potential in Electroencephalogram, collaborating with Centre Hospitalier Universitaire Vaudois (CHUV).
- 10/2000 - 02/2001 Diploma project at EPFL: Control of a long-range X-Y scanning stage and Development and implementation of an Atomic Force Microscope (AFM). Nanometres resolution. Using Matlab for DSP, image processing and control, MSim for electronic circuit design.
- 02/2000 - 06/2000 Semester project at EPFL: Integration of a long-range X-Y scanning stage with heterodyne interferometer. Nanometres resolution. Using Matlab for DSP, C programming for High Speed Fringe Counter card programming, MSim for electronic circuit design.
- 10/1999 - 02/2000 Semester project at EPFL: Image processing for genes analysis, collaborating with University of Lausanne (UNIL). Using Visual C++ and Matrox Mil library for image processing.
- 10/1998 - 06/1999 Treasurer of Sysmic (EPFL student organisation).
- 07/1998 - 08/1998 Internship at HAEMONETICS S.A, in R&D Department: Statistical analysis of platelets in human blood. Parameterisation of statistical models for platelet concentration in the MCS+. (See: <http://www.haemonetics.com/products/pframe2.htm>).
-

Publications

Journal papers

1. M. Rotter, L. Dang, V. Jacquemet, N. Virag, L. Kappenberger and M. Haissaguerre. *Impact of varying ablation patterns in a simulation model of persistent atrial fibrillation*, to be submitted.
2. P. Ruchat, L. Dang, J. Schlaepfer, N. Virag, L. K. von Segesser and L. Kappenberger. *A biophysical model of atrial fibrillation to understand the outcome of surgical ablation procedures*, to be submitted.
3. P. Ruchat, L. Dang, N. Virag, J. Schlaepfer, L. Kappenberger and L. K. von Segesser. *A biophysical model of atrial fibrillation to define the appropriate ablation pattern in modified maze*, Eur J Cardiothorac Surg., submitted.
4. L. Dang, N. Virag, Z. Ihara, V. Jacquemet, J. Vesin, J. Schlaepfer, P. Ruchat and L. Kappenberger. *Evaluation of ablation patterns using a biophysical model of atrial fibrillation*, Ann Biomed Eng., 33(4):465-474, 2005.
5. V. Jacquemet, N. Virag, Z. Ihara, L. Dang, O. Blanc, S. Zozor, J.-M. Vesin, L. Kappenberger and C.S. Henriquez. *Study of unipolar electrogram morphology in a computer model of atrial fibrillation*, J Cardiovasc Electrophysiol., 14(10):172-179, 2003.

Conference papers and abstracts

6. N. Virga, L. Dang, and L. Kappenberger. *The effect of antitachycardia pacing on phase singularities observed in a biophysical model of atrial fibrillation*, HRS, Boston, USA, May 2006, submitted.
7. L. Dang, J. Schlaepfer, N. Virag, L. Kappenberger and P. Ruchat. *A biophysical model of atrial fibrillation to define the appropriate ablation pattern in modified Maze*, EACTS, Barcelona, Spain, September 2005.
8. L. Dang, M. Rotter, N. Virag, V. Jacquemet, L. Kappenberger and M. Haissaguerre. *Impact of excluded surface around the pulmonary veins on incidence of atrial flutter in a biophysical model of atrial fibrillation*, European Heart Journal, (Abstr. Suppl.), ESC, Stockholm, Sweden, September 2005.
9. L. Dang, N. Virag, J. Schlaepfer, P. Ruchat and L. Kappenberger. *Evaluation of ablation patterns using a biophysical model of atrial fibrillation*, Europace Supplements, 7(S1):69, EUROPACE, Prague, Czech Republic, June 2005.
10. N. Virag, L. Dang and L. Kappenberger. *Study of antitachycardia pacing of atrial arrhythmias in a biophysical model*, Europace Supplements, 7(S1):124, EUROPACE, Prague, Czech Republic, June 2005.

11. L. Dang, N. Virag, J. Schlaepfer, P. Ruchat and L. Kappenberger. *Comparison of standard ablation patterns using a biophysical model of atrial fibrillation*, SSC, Mdecine Cardiovasculaire, 8(S8):S53, SSC, Lausanne, Switzerland, June 2005.
12. V. Jacquemet, M. Rotter, L. Dang, N. Virag, L. Kappenberger and M. Haissaguerre, *Evaluation of combined pulmonary vein isolation and linear ablation in a biophysical model of atrial fibrillation*, Heart Rhythm, 2:274-275, HRS, New Orleans, USA, May 2005.
13. L. Dang, P. Ruchat, J. Schlaepfer, N. Virag and L. Kappenberger, *Study of the surgical Maze III procedure in a computer model of atrial fibrillation*, European Heart Journal, 25 (Abstr. Suppl.):543, ESC, Munich, Germany, September 2004.
14. L. Dang, P. Ruchat, J. Schlaepfer, N. Virag and L. Kappenberger. *Simplified maze procedure for the treatment of chronic atrial fibrillation - Comparison of clinical data with results from a computer model of human atria*, Heart Rhythm, 1(S1): S77, HRS, San Francisco, USA, May 2004.
15. L. Dang, N. Virag, Z. Ihara, V. Jacquemet, O. Blanc, J.-M. Vesin, and L. Kappenberger. *Evaluation of ablation patterns by means of a computer model of human atria*, in Proc. of the 25th Annual International Conference-IEEE/EMBS 2003, pp. 126-129, Mexico, September 2003.
16. L. Kappenberger, N. Virag, L. Dang, V. Jacquemet, A. Forclaz, J. Schlaepfer and P. Ruchat. *How to study atrial fibrillation: a computer model*, in Proc. Internat. Meeting on Atrial Fibrillation, pp.15-21, Bologna, Italy, September 2003.
17. N. Virag, O. Blanc, L. Dang, V. Jacquemet, Z. Ihara, J.-M. Vesin, C.S. Henriquez and L. Kappenberger. *Characterizing anti-tachy pacing efficiency in a numerical model of human atrial arrhythmias*, European Heart Journal , 24 (Abstr. Suppl.):601, ESC, Vienna, Austria, September 2003.
18. V. Jacquemet, N. Virag, Z. Ihara, L. Dang, O. Blanc, J.-M. Vesin, C.S. Henriquez and L. Kappenberger. *A computer model of sustained atrial fibrillation to study atrial electrograms*, IJBEM, 5(1):181-182, ICE, Helsinki, Finland, June 2003.
19. V. Jacquemet, Z. Ihara, L. Dang, O. Blanc, N. Virag, J.-M. Vesin, L. Kappenberger and C.S. Henriquez, *Analysis of electrogram morphology to detect gross structural remodeling during chronic AF: model study*, PACE, 24(4 Part II):1025, NASPE, Washington DC, USA, April 2003.
20. L. Dang, Z. Ihara, V. Jaquemet, N. Virag, O. Blanc, J.-M. Vesin, and L. Kappenberger, *Optimization of antitachycardia pacing using a computer model of atrial arrhythmias*, PACE, 24(4 Part II):1025, Washington DC, USA, April 2003.